

Multipixel Si PN Junction Photodetector Sensor Arrays for the Depth Resolved  
Measurement of Tissue using Diffuse Reflectance Spectroscopy  
by

Callie Marie Woods

Department of Electrical and Computer Engineering  
Duke University

Date: \_\_\_\_\_

Approved:

---

Nan M Jokerst, Advisor

---

Richard B Fair

---

Aaron Franklin

---

Loren Nolte

---

Adrienne Stiff-Roberts

Dissertation submitted in partial fulfillment of  
the requirements for the degree of Doctor  
of Philosophy in the Department of  
Electrical and Computer Engineering in the Graduate School  
of Duke University

2020

ABSTRACT

Multipixel Si PN Junction Photodetector Sensor Arrays for the Depth Resolved  
Measurement of Tissue using Diffuse Reflectance Spectroscopy  
by

Callie Marie Woods

Department of Electrical and Computer Engineering  
Duke University

Date: \_\_\_\_\_

Approved:

---

Nan M Jokerst, Advisor

---

Richard B Fair

---

Aaron Franklin

---

Loren Nolte

---

Adrienne Stiff-Roberts

An abstract of a dissertation submitted in partial  
fulfillment of the requirements for the degree  
of Doctor of Philosophy in the Department of  
Electrical and Computer Engineering in the Graduate School of  
Duke University

2020

Copyright by  
Callie Marie Woods  
2020

## Abstract

The optical characteristics of tissue can give insight into the health status of that tissue. Tissue health is indicated by tissue properties such as chromophore concentrations (including hemoglobin, iron, glucose and cytochrome oxidase) as well as by the type of cells (cancerous vs normal) present in the tissue. Diffuse reflectance spectroscopy (DRS) is a non-invasive optical interrogation technique for the quantification of tissue properties and the classification of tissue. DRS systems are generally composed of two parts, the sensing system and the data processing used for tissue/sample analysis. Systems and analysis techniques can both range widely depending on the application. Moreover, the classification accuracy of both can suffer in low signal-to-noise ratio (SNR) settings.

This thesis combines a high density multipixel Si photodetector (PD) probe, Monte Carlo (MC) simulations, and partial least squares regression (PLSR) analysis to enable the extraction of optical properties and the classification of samples in low SNR settings. The development and characterization of a DRS multipixel Si PD sensor array is presented. A multipixel Si PD sensor array is used herein to measure homogenous liquid tissue-mimicking phantoms. This data was then used to develop a PLSR algorithm to directly predict, for the first time, the optical coefficients of a tissue-mimicking phantom in a leave-one-out approach. The Si PD array was also used to

conduct DRS measurements of 2-layer and 3-layer solid phantoms that were modeled using MC simulations to analyze the depth sensitivity of the multipixel Si PD array. This depth sensitivity analysis contributes to the DRS field by examining the difference in DRS signals between homogeneous and heterogeneous samples using a multipixel Si PD probe, demonstrating, for the first time, that low contrast buried layers surrounding by homogeneous media can be detected.

# Contents

Abstract .....	iv
List of Tables .....	ix
List of Figures .....	x
Acknowledgements .....	xiii
1. Introduction .....	1
2. Background .....	5
2.1 Diffuse Reflectance Spectroscopy .....	5
2.2 Semiconductor Photodetectors and PN Junctions .....	12
2.3 General Tissue Characterization .....	14
2.4 Monte Carlo Simulations for the Extraction of Optical Properties .....	18
2.6 Partial Least Squares Regression .....	22
2.7 Depth Analysis in Diffuse Reflectance Spectroscopy .....	25
2.8 Conclusions .....	29
3. Sensor Fabrication .....	31
3.1 Sensor Design .....	31
3.2 Junction Depth Optimizations .....	39
3.3 Sensor Fabrication Process Flow .....	41
3.4 Sensor Array Characterization .....	49
3.5 Conclusions .....	53
4. Homogenous Phantom Optical Property Extraction .....	54

4.1 Partial Least Squares Regression.....	55
4.2 Experimental Setup.....	57
4.3 Prediction Accuracy as a Function of SNR.....	60
4.4 Prediction Accuracy as a Function of Number of Detectors.....	63
4.5 Conclusions.....	66
5. 2-layer Solid Phantom Experiments and Simulations.....	68
5.1 Motivation.....	68
5.2 Experimental Results.....	70
5.3 Simulations vs Experimental Results.....	74
5.4 Simulations.....	77
5.5 Reflectance as a Function of Depth.....	80
5.6 System Resolution as a Function of Optical Properties.....	85
5.7 Conclusions.....	88
6. Experiment and Simulation for Three Layer Phantoms.....	90
6.1 Motivation.....	90
6.2 Experimental Results.....	92
6.3 Simulation of Phantoms Containing a Buried Layer.....	97
6.4 ROC Curves in Decision Making.....	101
6.5 ROC Analysis of the DRS Sensing System.....	103
6.6 Classification of 3-Layer Structures.....	108
6.7 Conclusions.....	110
7. Conclusions.....	112

7.1 Conclusions .....	112
7.2 Future Work: Depth Analysis with Arrays Composed of More Pixels .....	114
7.3 Future Work: The Sensing of Cytochrome C Oxidase .....	115
References .....	121
Biography .....	127

## List of Tables

Table 1: Optical Tissue Parameters for Sensor Design .....	34
Table 2: Boron Junction Test Diodes .....	41
Table 3: Phosphorus Test Diodes.....	44
Table 4: Al Test Diode Anneal Time and Temperatures .....	46
Table 5: Optical Properties of Homogenous Liquid Phantoms.....	59
Table 6: Percent of Data Used in SNR Analysis for Given Minimum SNRs .....	62
Table 7: Detectors used for Prediction Accuracy as a Function of Number of Detectors Analysis .....	63
Table 8: Detector Numbers from Each Group used in Prediction Error as a Function of Detector Group Analysis .....	65
Table 9: Optical Properties of Sets of Solid Phantoms .....	71

## List of Figures

Figure 1: Photon interactions with tissue at yellow scattering centers and red absorption centers.....	6
Figure 2: Possible Photon Paths Through Tissue .....	7
Figure 3: Si PD Arrays Fabricated by Jokerst Group (a) 4x4 Si PD Array (b) 24 Pixel Si PD Array .....	8
Figure 4: 100 Rays from MC Simulations of Skin Tissue.....	19
Figure 5: Pixel Configuration of 32 Pixel Si PD Array Designed Herein .....	32
Figure 6: 100 Rays Simulated in Zemax for the Design of the Multipixel Array Herein..	35
Figure 7: Simulated Power vs Radial Distance for Four Optical Property Pairs .....	36
Figure 8: Simulated Photocurrent for 32 Pixel Si PD Array .....	39
Figure 9: Responsivity for Different Junction Depths as a Function of Wavelength Simulated in Silvaco .....	40
Figure 10: Dark Current of Phosphorus Test Diodes.....	45
Figure 11: Dark Current Per Unit Area of Al Test Diodes .....	46
Figure 12: Packaged 32 Pixel Si PD Sensor Array .....	48
Figure 13: Si PD Sensor Array Process Flow .....	48
Figure 14: Responsivity of Pixels in 32 Pixel Si PD Sensor Array .....	50
Figure 15: Dark Current and Dark Current per Unit Area of 32 Pixel Si PD Sensor Array .....	51
Figure 16: SNR of Pixels in Si PD Sensor Array for Wavelengths between 400 nm - 800 nm.....	52
Figure 17: Experimental Setup for Homogenous Liquid Phantom Measurements .....	57

Figure 18: Prediction Results for Leave-One-Out Prediction Using PLSR .....	61
Figure 19: Prediction Error as Function of SNR for LUTs and PLSR Analyses .....	62
Figure 20: Prediction Error as a Function of Detector Number Using PLSR.....	64
Figure 21: Prediction Error for Detector Groups using PLSR.....	65
Figure 22: Experimental Setup for Solid Phantom Experiments (a) Multipixel Si PD Sensor Array (b) Testing Setup with Solid Phantoms .....	70
Figure 23: Experimental Results for 2-Layer Solid Phantoms Measurements Using Set 1 Phantoms.....	72
Figure 24: Experimental Results for 2-Layer Solid Phantom Measurements Using Set 2 Phantoms.....	73
Figure 25: Theory vs Experiment for 2-Layer Solid Phantom Measurements Using Set 1 Solid Phantoms.....	76
Figure 26: Theory vs Experiment for 2-Layer Solid Phantom Measurements Using Set 2 Solid Phantoms.....	76
Figure 27: Theoretical Spaces Simulated in Chapter 5.....	78
Figure 28: Simulated Photocurrents for 2-Layer Phantoms Using Theoretical Space 1 ...	78
Figure 29: Contrast for a Simulated Set of Solid Phantoms .....	79
Figure 30: Simulated Phantom Setup for Creation of Depth vs DRS Signal Curves.....	81
Figure 31: Simulated Reflectance vs Depth for 6 Detectors in the Multipixel Si PD Sensor Array .....	82
Figure 32: Normalized Reflectance as a Function of Depth for one Set of Optical Properties .....	84
Figure 33: Reflectance vs Depth for Different Optical Properties at Select Detectors.....	86
Figure 34: Effect of Changing Absorption Levels on Simulated DRS Signal for 4 Phantom Thicknesses .....	87

Figure 35: Experimental Setup for 3-layer Solid Phantoms Measured Using a 400 um Aperture Si PD Sensor Array .....	92
Figure 36: 3 Layer Solid Phantom Measurements using 400 um Si PD Sensor Array .....	95
Figure 37: Theory vs Experiment for 3-Layer Solid Phantoms Measured using a 400 um Si PD Sensor Array .....	98
Figure 38: Simulated 3-Layer Phantoms using a 750 um Aperture Si PD Sensor Array	100
Figure 39: ROC Curves for Simulated 3-layer Phantoms as a Function of Detector Group .....	104
Figure 40: ROC Curves for Experimentally Measured Data as a Function of Detector Group.....	105
Figure 41: ROC Curves as a Function of Top Layer Thickness for Simulated Phantoms .....	106
Figure 42: ROC Curves as a Function of Buried Layer Thickness for Simulated Phantoms .....	107
Figure 43: ROC Curves for a Highly Absorbing Buried Layer as a Function of Detector Group.....	108
Figure 44: Repeatability of Blood Pressure Cuff Measurements using Multipixel Si PD Sensor Array .....	118
Figure 45: Blood Pressure Cuff Measurements for No Inflation, Inflation to 60 mmHg and Inflation to 200 mmHg.....	119

## Acknowledgements

I would like to start by thanking my advisor, Dr. Nan Jokerst. Her guidance and support throughout my dissertation work has been inspiring. She has helped me grow greatly as a researcher.

I also would like to thank our collaborators, Dr. Gage Greening, Dr. Timothy Muldoon, and Dr. Richard Moon. The work of Dr. Greening and Dr. Muldoon creating the solid phantoms used herein was instrumental to this dissertation. The design and testing portion of this work was inspired by conversations with Dr. Richard Moon. The future work section would be done in further collaboration with him.

Thank you to Dr. Adrienne Stiff-Roberts, Dr. Loren Nolte, Dr. Richard Fair, and Dr. Aaron Franklin for being on my committee and for all that they taught me during their classes. Each class has influenced this work.

Thank you to all the members of Jokerst Group that have been there during my time. As each of them has left, I have greatly missed them and the talks that we would have in the office. They made pursuing a Ph.D fun and full of new and exciting discoveries.

Many thanks go out to the staff members of the Shared Materials Instrumentation Facility for the training they provided and the help troubleshooting

throughout the fabrication process. I learned much more than I imagined possible about the cleanroom from them.

Finally, I would like to thank all the family and friends that have supported me throughout my time at Duke and throughout my journey as a student. From high school through graduate school, they have kept me laughing and pushed me to go further.

# 1. Introduction

Tissue classification is of great interest to the medical community. Classification can include chromophore quantification (including hemoglobin, iron, glucose and cytochrome oxidase) and other characteristics that determine tissue health. Currently, a great deal of tissue classification relies first on excising tissue and then measuring properties. This not only involves surgery for the patients, but it can also lead to long wait times for diagnosis. This is particularly true for rural settings where samples sometimes need to be shipped large distances for analysis if on-site labs are not available.

Diffuse reflectance spectroscopy (DRS) is an optical interrogation technique for the quantification of tissue properties and the classification of tissue. Tissue properties include the optical absorption and scattering coefficients ( $\mu_a$  and  $\mu'_s$ , respectively). These optical parameters are used to characterize and classify tissue samples *in-vivo* and *in-vitro* [1]. Knowledge of these parameters can inform physicians about tissue characteristics (cancerous vs non-cancerous) and can yield information about the composition of the tissue (quantity of chromophores present). Since DRS is a non-invasive technique, surgery is not required for patients, and diagnosis can happen at the same appointment. The range of applications is large, making DRS an area of great interest to the research and medical communities. Potential applications of a DRS probe include skin cancer detection [2], breast cancer margin assessment [1], glucose

concentrations [3], and colon cancer classification [4]. Currently in clinical settings, to perform any of the aforementioned procedures, some form of invasive procedure is involved even if it is pricking a finger for a small blood sample. The use of DRS has the potential to offer an alternative to the use of invasive measures.

DRS systems are generally composed of two primary functional parts, the sensing system and the data processing used for tissue analysis. Systems and analysis techniques can both range widely, depending on the application. Reported DRS systems typically use fibers for detection [5], [6], however, these fiber systems suffer from poor signal to noise ratio (SNR) compared to recently reported systems that utilize photodetectors (PDs) directly detecting the DRS signals. [7]. These PD-based systems have higher SNR and are thus applicable to a wider range of DRS sensing applications. For example, often DRS signals are very small, particularly when trying to sense deep into the body or through highly absorptive material, and a higher SNR system enables the use of DRS. This thesis will focus on the use of a Si PD-based DRS probe.

In applications where direct knowledge of tissue properties is required (e.g. glucose monitoring), reported analysis techniques include Monte Carlo (MC) simulations, look-up tables (LUT), and partial least squares regression (PLSR). Other applications (e.g. breast cancer detection) require only a decision (yes/no) regarding classification, for which direct extraction of optical properties may not be necessary [1]. All of these systems are limited in low signal-to-noise ratio (SNR) settings. This thesis

combines a high density Si PD multipixel probe and PLSR analysis to enable extraction of optical properties and classification of samples/tissues in low SNR settings. Herein is included background information regarding DRS, followed by an analysis of current systems and algorithms. A SRDRS probe for depth-resolved measurements will be presented, including a process flow for Si probe fabrication, measurements using multipixel Si PD probes, MC and PLSR data analysis, and an in-depth analysis of the depth sensitivity of SRDRS.

Herein, the Si PD array was also used to conduct DRS measurements of 2-layer and 3-layer solid phantoms that were modeled using MC simulations to analyze the depth sensitivity of the multipixel Si PD array. Many previous DRS systems assume that the tissue being interrogated is homogenous. *In vivo*, this assumption fails. Layers within tissue, in addition to more macroscopic features such as veins, require sensors that can distinguish between the different tissue properties. Even very thin tissue samples are often composed of smaller tissue layers that have different optical and physical properties that vary with tissue type and the specific biological features present. As photons travel through a tissue sample they are scattered or absorbed based on the features that they encounter. Thus, different physical layers in a tissue under optical interrogation can greatly affect the DRS signal. For example, a highly absorbing cancerous layer of tissue can be buried under and surrounded by normal tissue. A photon interacting with the cancerous tissue is more likely to be absorbed than if the

entire tissue sample was homogenous, normal tissue. The depth at which the cancerous tissue is located and the thickness of the cancerous layer will both change the number of photons that will propagate back to the surface and be collected. This thesis research contributes to the DRS field by assessing the effects of heterogenous samples on DRS signals using a multipixel Si PD probe, demonstrating that highly absorbing layers (e.g. as exhibited by cancer) buried in normal tissue can be detected.

## 2. Background

This thesis focuses on the use of a multipixel array for depth-sensitive tissue measurements using diffuse reflectance spectroscopy. This chapter discusses information relevant to the measurement and characterization of tissue including diffuse reflectance spectroscopy, silicon photodetectors, current methods for tissue characterization, and current systems for the depth resolved analysis of tissue.

### 2.1 Diffuse Reflectance Spectroscopy

Diffuse reflectance spectroscopy (DRS) is an optical, non-invasive interrogation technique that enables the determination of the properties of a sample under test, including absorption and scattering coefficients. When used to measure biological tissues, this optical information is associated with a variety of tissue characteristics, including chromophore concentration [8], blood perfusion [9], and the presence of cancerous cells [10]. For *in vivo* tissue measurements, DRS is preferred over transmission spectroscopy because DRS measurements often collect more light and result in higher signals, since *in vivo* tissues are often optically thick samples that limit the number of photons collected. For transmission spectroscopy a detector is placed on the opposing side of the tissue from the illumination and the detector monitors transmitted light. In contrast, in DRS measurements a probe is placed on the same side of a surface as the light source. The tissue is illuminated, and photodetectors on the tissue surface collect the photons that travel through the tissue and are scattered back to the surface.

Light incident on tissue is absorbed or scattered as determined by the tissue composition and the wavelength of incident light. Light interacting with absorption centers known as chromophores will be absorbed and will thus cease to travel through the sample. Microscopic discontinuities in the sample as well as changes in refractive index will result in photon scattering [11]. The overall photon path is determined by its interactions with these two types of sites within the tissue [12]. The possible interactions between photons and absorption and scattering centers are depicted in Figure 1.

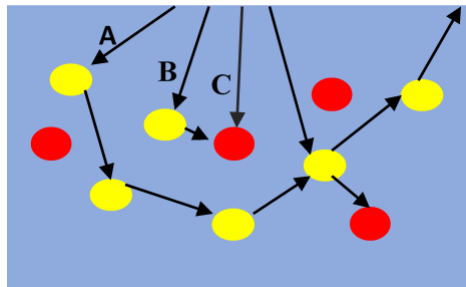


**Figure 1: Photon interactions with tissue at yellow scattering centers and red absorption centers.**

Photons can travel many different paths through the tissue, as shown in Figure 2, and multiple photodetectors (PDs) can enable spatially resolved detection of the DRS signal, called spatially resolved DRS (SRDRS). Photons entering a tissue sample follow a roughly banana shaped curve. Typically, photons exiting the surface of the tissue farther away from the source have penetrated deeper into the tissue. SRDRS can enable knowledge of photon penetration depth. PDs located at different radial distances from the source collect photons that have interacted with different sections of tissue at different depths. The power collected at each PD can then be associated with properties

present at different tissue depths. Since many photons pass through multiple layers of tissue while propagating through the tissue, to enable layered analysis, the signals from different layers must be separated from each other. SRDRS is particularly useful in non-homogenous media. While many models assume homogeneity within tissue samples for experimental testing, *in vivo* systems are complex, and within the skin, for example, there are multiple layers that have different optical and physical tissue properties. There have been limited reports of the use of SRDRS to evaluate individual tissue layers. This thesis will look at the isolation of signals from specific layers of a multilayer sample that mimics tissue using a multipixel Si PD probe. This system is designed for depth resolved measurements and, for the first time, uses experimental SRDRS to enable local isolation of a buried layer.

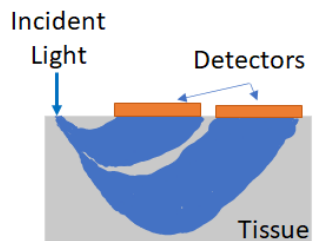


**Figure 2: Possible Photon Paths Through Tissue**

The benefits of SRDRS for evaluating tissue properties motivated the Jokerst Research group to develop a number of different PD arrays for DRS and SRDRS measurements. Both thick [13] and thin film [12] PD arrays have successfully demonstrated the ability to measure optical tissue properties. Early iterations of SRDRS PD probes developed by the Jokerst Research group focused on uniformly spaced

detectors in a 4x4 array (Figure 3) [12]. The PDs in this array had a hole in the center of each PD that allowed light to pass through the PD to illuminate the sample.

Photocurrent measurements were measured simultaneously from all 16 PDs.

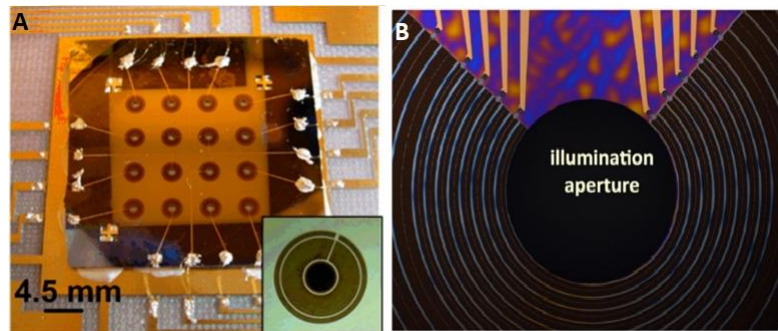


**Figure 3: Si PD Arrays Fabricated by Jokerst Group (a) 4x4 Si PD Array (b) 24 Pixel Si PD Array**

To enable higher signal to noise ratio (SNR) depth measurements, a concentric multipixel photodiode array was fabricated for generalized tissue measurements (Figure 3) [13]. This 24-pixel array had a higher density of pixels compared to most SRDRS systems. The larger pixel density combined with 26 wavelength measurements using a broadband spectrometer from 400-650 nm increased the amount of data collected compared to other systems that use a few fibers as collectors. Using a probe that could collect larger amounts of light due to a higher numerical aperture increases the signal strength and can increase the range of tissue properties capable of being measured [14]. Tissues with high absorption result in less light at detectors further from the source. Higher collection efficiencies at the detector can thus increase photocurrent, which is particularly useful at further source-detector separations. The use of Si PDs (with a

higher numerical aperture than fibers) instead of fibers gives the multipixel array and other systems developed by the Jokerst Research group this higher collection efficiency. With a larger signal and thus a larger SNR, more accurate tissue property extraction may be possible because more of the signal can be captured (higher signal) compared to the noise. [15].

In DRS, a variety of parameters termed “optical tissue properties,” such as absorption coefficients and scattering coefficients are used to characterize and classify tissue samples. Optical tissue properties can vary widely both within a given tissue type and between tissue types [11]. Knowledge of the scattering and absorption coefficients, mean free path, anisotropy factor, and scattering function enables comparison between samples and the prediction of photon path for different tissue compositions and wavelengths.

To characterize tissue, the two most often used optical tissue properties are the scattering coefficient,  $\mu_s$ , and the absorption coefficient,  $\mu_a$ . The former is defined as the rate at which radiant energy is lost due to scattering measured per incremental unit photon path length [11], and the latter is the rate at which a sample absorbs photons. The scattering coefficient is the product of the scatter number density,  $\rho_s$ , and the cross sectional area of scattering,  $\sigma_s$  [16], as shown in Equation 2.1:

$$\mu_s = \rho_s \sigma_s \quad \text{Equation 2.1}$$

A spherical particle will redirect photons interacting with it in new directions, thereby preventing forward, on-axis transmission [16]. Photons cannot be scattered at a 180 degree angle. Thus, there is a shadowed section where photons cannot be scattered based on the size of the particle, known as the cross-sectional area of scattering. The relationship between the probability of transmission,  $T$ , without redirection for a given photon path length ( $L$ ) and  $\mu_s$  is given by Equation 2.2 [16]:

$$T = e^{-\mu_s L} \quad \text{Equation 2.2}$$

Absorption in tissue is mainly attributed to the presence of absorbing molecules called chromophores. An individual chromophore has a unique absorption spectra that combines with other chromophores to give the overall absorption of the tissue [11]. The spectra can overlap significantly with each other, and some chromophores contribute more strongly to the absorption than others. As with its scattering counterpart,  $\mu_a$  has units of  $\text{cm}^{-1}$  [16]. The absorption coefficient is the product of the absorption number density,  $\rho_a$ , and cross-sectional area of absorption  $\sigma_a$ , as shown in Equation 2.3:

$$\mu_a = \rho_a \sigma_a \quad \text{Equation 2.3}$$

The probability of transmission without absorption is shown in equation 2.4 [16]:

$$T = e^{-\mu_a L} \quad \text{Equation 2.4}$$

The angles over which a photon can scatter are characterized by the anisotropy factor,  $g$  [11]. This optical tissue property is only valid far from tissue boundaries and

sources where complex scattering is significantly less likely to occur [11]. Near tissue boundaries and optical sources, a more robust treatment of the angular scattering distribution of photons is required. The angular ( $\theta$ ) dependence of  $g$  is shown in Equation 2.5:

$$g = \langle \cos(\theta) \rangle \quad \text{Equation 2.5}$$

Since  $g$  is tissue dependent, the scattering coefficient is often described in the context of the anisotropy factor, as the reduced scattering coefficient,  $\mu'_s$ , as shown in equation 2.6 [11]:

$$\mu'_s = \mu_s(1 - g) \quad \text{Equation 2.6}$$

Two additional tissue parameters describe the relationship between the total attenuation coefficient,  $\mu_t$ , and the tissue. Albedo,  $a$ , sometimes referred to as the single scattering albedo, is the ratio between  $\mu_s$  and  $\mu_t$ , as shown in Equation 2.7 [11]:

$$a = \frac{\mu_s}{\mu_t} = \frac{\mu_s}{\mu_a + \mu_s} \quad \text{Equation 2.7}$$

The inverse of  $\mu_t$  is the mean free path, MFP, which is the average distance traveled by a photon before an absorption or scattering event, as shown in Equation 2.8 [11]:

$$MFP = \frac{1}{\mu_t} = \frac{1}{\mu_s + \mu_a} \quad \text{Equation 2.8}$$

Both albedo and MFP describe the likelihood of a photon being reemitted from the tissue.

DRS can be used to characterize tissue by quantifying optical tissue properties. SRDRS will be used herein to evaluate both bulk tissue properties and individual layers of tissue. While previous studies have looked at bulk tissue properties [17]–[19], analyses of multilayered structures within the DRS field are limited. This thesis explores the ability of a multipixel Si PD probe to investigate the location of separate layers of tissue within multilayer samples for the first time. Optical tissue properties vary between types of tissue. One significant contribution of this thesis is an exploration of the sensitivity of the depth analysis to small changes in the optical properties.

## ***2.2 Semiconductor Photodetectors and PN Junctions***

Most DRS systems use fibers as a light collection mechanism, however, the PDs used in this thesis have some significant advantages over optical fibers for DRS light collection. Optical fibers have a low numerical aperture compared to photodetectors (PDs), and a cladding that occupies potential detection space, but that does not detect light. Additionally, PDs can be designed for a wide range of sizes and with little non-detecting space between the PDs [7]. Thus, the detected signal for DRS systems that employ PDs instead of fibers can yield a significantly higher signal, and a correspondingly higher SNR than fiber-based DRS detection systems.

A semiconductor PD is an optoelectronic device that produces electrical current from incident absorbed optical photons [20]. Of particular interest to this thesis are silicon (Si) PDs [21] since Si has high responsivity in the visible range and moderate

responsivity in the near infrared up to  $\lambda = 1 \text{ um}$ . Si is a low-cost fabrication material, and thus, Si is a good material of choice for detectors in DRS systems. The Jokerst Research group has previously used both thick and thin-film Si PDs for tissue classification in DRS systems [12], [13].

In PDs, the generation of electron-hole pairs forms the basis for the conversion between electrical and optical energy [22]. When illuminated with light of energy greater than the bandgap energy, PDs will absorb photons. The absorbed energy results in an electron being excited from the valence band to the conduction band, generating an electron-hole pair [22]. The resulting pair can then be separated and transported to the contacts for carrier extraction and contribute to the photocurrent of the device. Joining a p-type semiconductor with an n-type semiconductor results in a PN junction photodiode [22], which aids in the separation and transport of electron-hole pairs to produce measurable photocurrent after photogeneration has occurred.

Previously fabricated photodetectors in the Jokerst Research group have included Si PN junction photodiode arrays [10], [23], [24]. These Si photodiodes have demonstrated excellent performance in three key parameters: responsivity, dark current and signal-to-noise ratio (SNR). A functional device should have high responsivity and SNR in addition to a low dark current.

The number of amps of electrical current produced per incident watt of optical light by a PD due is the responsivity [22]. High levels of surface recombination and

defects that result in recombination centers can decrease the responsivity of PDs [22].

The responsivity,  $R$ , is given in Equation 2.9, where both the photocurrent,  $I_{ph}$ , and the incident power,  $P_o$ , are wavelength dependent:

$$R = \frac{I_{ph}}{P_o} = \frac{\eta q}{h\nu} \quad \text{Equation 2.9}$$

where  $\eta$  is the quantum efficiency,  $q$  is charge, and  $h\nu$  is the photon energy. Previously published responsivities by the Jokerst Research group for thick film devices are as high as 0.3 A/W at 600 nm [10].

The system presented herein uses a series of consecutive photocurrent measurements to calculate the SNR of the device. 10 measurements enable a calculation of the mean and standard deviation of the photocurrent which are combined to calculate SNR as in Equation 2.10:

$$SNR = 20 * \log\left(\frac{signal}{noise}\right) = 20 * \log\left(\frac{I_{ph}}{\sigma}\right) \quad \text{Equation 2.10}$$

This thesis describes the design, fabrication, and test of low dark current, high responsivity PDs using standard Si epitaxial wafers. The high SNR of the PDs enables accurate extraction of optical tissue properties in low signal systems.

### **2.3 General Tissue Characterization**

The characterization of tissue involves the quantification of optical tissue properties and the association of these properties with different tissue classifications.

The determination of optical tissue properties can also be used to extract chromophore

concentration and gain further knowledge of the makeup of the tissue. A general approach to chromophore extraction and tissue characterization seeks to solve the modified Beer-Lambert Law, which relies on knowledge of the optical tissue properties.

A key component to determining tissue properties *in vivo* is the quantification of the optical path length through the tissue. In systems where scattering does not play a role, the Beer-Lambert Law can be evaluated to quantify chromophore concentration,  $A$ , as in Equation 2.11 [19]:

$$A = \log_{10} \left( \frac{I}{I_0} \right) = \mu_a l \quad \text{Equation 2.11}$$

where  $l$  is the optical path length,  $I$  is the measured intensity, and  $I_0$  is the input light intensity. The absorption ( $\mu_a$ ) is the linear sum of the individual absorbers (chromophores) present in the system [25]. These include water, hemoglobin, myoglobin, and CCO in addition to other chromophores with smaller absorptions. Thus, the absorption,  $\mu_a$ , is given by Equation 2.12:

$$\mu_a = \sum_{i=1}^n C_i \mu_{ai} \quad \text{Equation 2.12}$$

where  $C_i$  is the concentration of a given chromophore and  $\mu_{ai}$  is the corresponding absorption coefficient. In systems with no scattering component, the optical path length is the distance that the light travels through the sample as measured from the source to the detector. When scattering is introduced, as is the case in tissue samples, the Beer-

Lambert law is no longer valid. Scattering introduces two additional components into the equation, resulting in the modified Beer-Lambert law, where the chromophore concentration,  $A$ , is given by Equation 2.13 [19]:

$$A = \mu_a B(\mu_a)l + G \quad \text{Equation 2.13}$$

where  $G$  is a term associated with scattering losses within the system and  $B(\mu_a)$  is the differential path length (DP), which reflects that the physical path of light through a sample containing scatterers is many times that of the geometrical path length (the distance between the source and the detector).  $B(\mu_a)$  is further defined as the ratio between the mean optical path length that a photon travels and the geometrical distance between the source and the detector is given by Equation 2.14 [5]:

$$B(\mu_a) = \frac{\text{Optical path length}}{\text{Geometrical path length}} \quad \text{Equation 2.14}$$

The reduced scattering coefficient and the system geometry strongly influence the DP of the system. In practice, the mean path length of a photon is often much larger than the geometrical path length, leading to DP values between 3 and 6 [5]. The modified Beer-Lambert law indicates that the concentration of a chromophore cannot be directly obtained from an attenuation measurement unless the DP is known. Since optical scattering and absorption are wavelength dependent, the DP is also a wavelength dependent term and must therefore be calculated for each wavelength used in measuring an attenuation spectrum.

Due to the complexity introduced by scattering within tissue, most commercially available systems seek only to characterize changes in chromophore concentration. Among those that do report absolute chromophore concentrations (such as commercially available oximeters), only a few wavelengths are used. Due to the wavelength dependence of scattering within tissue, these instruments are challenged by errors produced due to the large variety of chromophores in tissue including hemoglobin, myoglobin [26]. The absorption of these chromophores is affected by the wavelength of light incident on the tissue and can also change with O<sub>2</sub> saturation, tissue pH, and oxygen tension [26]. Chromophores with smaller absorptions than the three largest mentioned above can also play a role in tissue absorption and thus affect optical measurements. A thorough understanding of the DP is therefore often necessary to measure chromophore concentrations and determine optical tissue properties.

This work seeks to minimize the low SNR effects of highly absorptive systems by combining Si PDs (with high SNRs) with a highly pixelated system designed for depth sensitivity. By densely packing the Si PD array, optical properties at different depths can be measured. Photons traveling to different depths in the samples arrive at different source/detector spacings. At larger source/detector spacings, fewer photons arrive at the surface to be collected by the PD. Using a custom design of the Si PDs to take into account this decrease in photon flux, a Si PD array has the design flexibility to achieve a large targeted SNR. Additionally, this thesis will show that groupings of PDs can be

used to target layers of tissue. Fiber based systems have low numerical apertures compared to Si PDs, so a single pixel array or a small grouping of fibers will suffer from either a lack of spatial resolution or an inability to collect the majority of the photons re-emitted from the surface of the tissue. This thesis analyzes a Si PD array designed to improve upon both the collection efficiency and the spatial resolution limitations of current fiber and single pixel DRS systems.

## ***2.4 Monte Carlo Simulations for the Extraction of Optical Properties***

DRS systems contain two parts: the physical system used to measure the signal, and the analytical methods for the extraction of variables of interest (e.g. tissue optical properties). This section will look at one of the most used methods for optical property quantification: Monte Carlo simulations. Using physical *in vivo* measurements to characterize tissue is difficult since tissue is typically inhomogeneous and layered. Using homogeneous phantoms with known optical properties, measurements and subsequent analysis have produced accurate optical property extraction. The analysis methodology used has been statistical simulation of photon propagation through tissue, for which measurements can be matched to optical properties. One such theoretical approach that has been widely used in DRS is the Monte Carlo (MC) simulation method. MC simulations have been used to accurately calculate optical tissue properties by fitting forward models to measured results. These models are generally very robust and produce accurate results if a sufficiently large number of photons are tracked in the

simulation. Often millions of photons are simulated (Figure 4). Monte Carlo simulations using fewer than a million photons have large prediction errors and standard deviations between measurements due to the large range of paths a photon can travel within the tissue. Each scattering event adds a path segment that can be stored and analyzed as a part of the simulations. Since photons travel different paths, the MC simulation will result in a distribution of photons being re-emitted at different locations on the surface of the tissue. If enough photons are simulated, then the distribution is statistically relevant and can be used to accurately simulate experimental measurements.

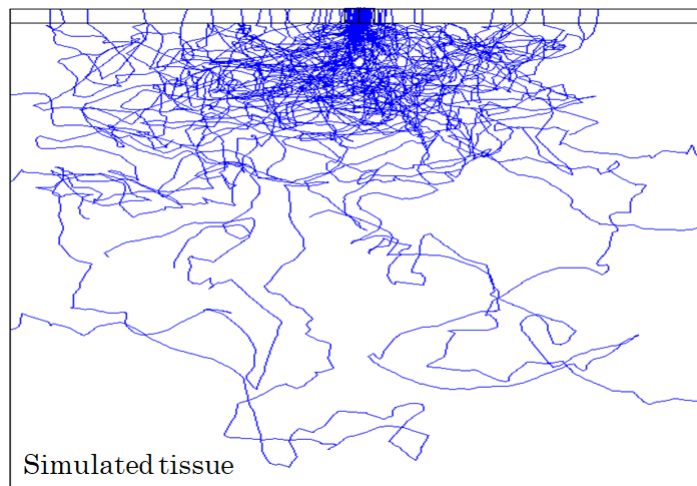


**Figure 4: 100 Rays from MC Simulations of Skin Tissue**

One of the benefits of MC simulations is the wide range of properties that can be modeled, enabling different tissue structures with varying levels of complexity to be simulated. MC simulations can also be combined with different phase functions to model the photon interactions with tissue. Phase functions are a property used to model the scattering and absorption within a system that can change drastically with the

geometry of the problem, as they can each be applicable in different absorption and scattering regimes. The Henyey-Greenstein phase function is often used to model tissue [18], [9]. Other options include the modified Henyey-Greenstein phase function [27] and Mie scattering which, while highly accurate, is computationally intensive. An isotropic component can be added to the Henyey-Greenstein phase function to more accurately describe light scattering *in vivo*, acknowledging the highly forward scattering nature of photon interactions in tissue [9]. In addition to the phase function, MC models permit the selection of scattering and absorption coefficients ( $\mu_s$  and  $\mu_a$ , respectively), and the anisotropy factor ( $g$ ), which characterizes the angular distribution of scattering. The ability to choose from a variety of parameters gives the users of MC simulations the flexibility to accurately simulate the structure they are modeling.

In addition to  $\mu_a$ ,  $\mu_s$ , and  $g$ , blood flow must also be considered in MC simulations. While many studies have previously ignored this factor, studies from Jakobssen et. al. demonstrated that the sampling depth of a simulation exhibits a strong dependency on the blood perfusion distribution [9]. Blood perfusion is a parameter which models the number of red blood cells and the mean velocity of those cells [9]. Blood perfusion is most relevant when sampling depths are such that major veins and arteries will be included in SRDRS measurements. Not all perfusion distributions are homogenous [9]. This adds to the complexity of the MC simulations which model blood perfusion when estimating photon path length. Simulations which focus on photons that

do not penetrate deeply into tissue can potentially ignore this parameter, however. Red blood cells have a  $\mu_s$  similar to that of skin tissue [9]. The scattering coefficient can therefore often be assumed to be the same as the skin tissue. This is not possible when the mean velocity of the red blood cells is large enough to add to scattering within the tissue. Therefore, if the depth resolution of the simulated device is small and the tissue does not contain red blood cells moving at a comparatively high velocity, incorporating the blood perfusion is not necessary. Blood perfusion is related to the pressure applied by a probe during measurement. When pressure is applied, blood from vessels under the device is displaced [28]. Changes in results due to probe pressure variation have been previously reported by multiple groups [28]. Therefore, if probe pressure is not going to be constant, MC simulations must account for blood perfusion in their estimations of optical tissue properties.

Simulated data has shown that photons travel through tissue in a path resembling the shape of a banana [27], as shown in Figure 2.2. Monte Carlo simulations have supported these results. The majority of photons travel through the core of the banana shaped region, and probability distributions can be created to estimate the mean path [27]. The tissue absorption and scattering both have an effect on the overall shape of the banana [27]. For example, as absorption increases, the penetration depth of the photons decreases.

As previously stated, MC simulations result in a large amount of data that must be processed. Additionally, the large number of photons that must be simulated is time consuming. This computational intensity decreases the value of MC simulations for path length extraction despite the high accuracy of the method. Simulations would be required for every combination of optical tissue properties to accurately compare experimental results to simulations. Due to the complex nature of tissues, the computational intensity of MC simulations is not feasible in most *in vivo* scenarios.

## **2.6 Partial Least Squares Regression**

Rather than simulate large data sets using MC methods, experimental results can be combined with regression techniques or machine learning to estimate tissue properties. Partial least squares regression (PLSR) is a regression technique used throughout the field of chemistry as a means of extracting quantitative data from optical spectra and other measurements [29]. In particular, PLSR has been applied for the *in vivo* quantification of blood glucose concentration [30], [31], to classify cancerous tissues [32], and to quantify brain lipids [33]. The use of PLSR to decompose chemical spectra in addition to the recent application of the technique to tissue samples suggests that PLSR can be an accurate method for quantifying optical tissue properties and tissue classification. Previous applications of PLSR to DRS do not directly use PLSR to extract the optical properties of the sample being measured. Instead, PLSR was used to identify latent variables that are then used in a machine learning algorithm to classify tissue [34].

This thesis is the first application of PLSR to DRS data to directly extract optical properties.

PLSR is a two step simulation process designed to associate desired output variables with features in the spectra provided to the model [29]. This is accomplished by solving a series of matrix equations. One of the benefits of multivariate linear regression techniques is that they can be applied to more than one dependent variable [29]. Thus, this method is applicable to chromophore concentration analysis when more than one chromophore is of interest. The first stage (the training step) involves creating a model of the system [29]. The parameters identified by the model are the regression coefficients later used to associate the input and output of the system. Stage two results in the prediction of dependent variables (in this case the chromophore concentrations) from the independent variables identified by the system [29]. For uses in spectroscopy, the data given to the model must be mean-normalized. However, no scaling of input samples is necessary [29], because the inputs to the model will be spectra acquired from a given system, and all in the same units. The mean-normalization allows the model to focus on spectral features rather than the absolute intensity of the spectra [32]. The ability to take complex spectra, or a series of complex spectra, and extract relevant information and associate it with the variables of interest is the strongest argument for the use of PLSR in chemistry and DRS. Mean normalization is performed as per Equation 2.15:

$$x' = \frac{x - \text{mean}(x)}{\max(x) - \min(x)} \quad \text{Equation 2.15}$$

Studies have compared the performance of PLSR to other regression techniques

as well as to MC simulations for DRS and chemical spectra. In general, regression techniques using the entire spectra have an advantage over simulation methods seeking to use only a few wavelengths in their analysis because regression can take advantage of the information provided by entire spectra [32]. PLSR, in addition to principle component analysis (PCA) and artificial neural network algorithms (ANNs), all seek to associate a data set containing many variables with the desired output variables [32]. These three regression models all contain an input layer (the dataset), a hidden later (the model), and an output layer (the variables of interest). These layers are associated with each other via a series of weights or regression coefficients. PLS and PCA have the theoretical ability to consistently outperform ANNs because the former two result in a global error minimum whereas ANNs generally are only capable of obtaining a local minimum in error [32].

When comparing PLSR to MC simulations, it is important to note that PLSR is a linear analysis technique that does not take into account specific knowledge of the tissue sample such as absorption and scattering, whereas MC simulations lead to additional knowledge about the optical properties of the tissue sample [1]. Despite this difference, MC simulations only performed a few percent better in tissue classification when compared to PLSR [1]. One key advantage of MC simulations is that they can be easily adapted to new iterations of probe design whereas completely new datasets must be acquired for training and testing PLSR models [1]. Therefore, while PLSR outperforms

other multivariate analytical techniques, more traditional methods such as MC simulations can lead to additional information and have a slightly higher accuracy. Despite the advantages of MC simulations, the computational time to perform a MC simulation is orders of magnitude greater than the time to perform PLSR. PLSR predictions can be completed in seconds compared to hours to perform a single MC simulation [34]. For accurate prediction, many MC simulations must be performed and compared to the experimental results. This is not necessary for PLSR, as PLSR trains on measured spectra.

A number of PLSR packages have been developed, enabling the technique to be easily applied to different situations [35]. Unfortunately, to accurately implement a PLSR model, datasets of 75-100 samples are required for clinical applications [36]. After the creation of a model, further dataset acquisition is necessary for testing. Data acquisition on this scale can impede the use of PLSR in clinical settings such as those that motivate this work. PLSR seeks to reduce the dimensionality of the data by associating specific features of the input with output variables [36]. Therefore, in evaluating which wavelengths are of the most interest or which detectors play the largest role in optical property quantification, PLSR can be used as an analysis technique to aid system optimization.

## ***2.7 Depth Analysis in Diffuse Reflectance Spectroscopy***

This thesis seeks to develop an understanding of the depth resolution of spatially resolved multilayer samples using a multipixel PD array. This is in contrast to previous studies that primarily focus on the classification of tissue and the quantification of optical coefficients in homogenous samples. In contrast, this thesis analyzes the capability of a sensor array to measure reflectance as a function of depth and to distinguish between layers of tissue in heterogenous samples. While many DRS measurements assume a homogeneous medium, this assumption is no longer valid when DRS systems are used for most *in vivo* sensing applications [37]. A photon traveling through skin tissue encounters changes in tissue optical properties as it moves through the dermis, epidermis, and as it encounters the small blood vessels that provide microcirculation within tissue [38]. When healthy and non-healthy tissues are present, the changes in optical properties can be even more pronounced than when the tissue is of one general type [4]. This section will describe the current state of depth resolved measurements in the field of DRS. An overview of current applications and their limitations will be discussed as well as a brief description of how the multipixel array described in this thesis can improve some of these drawbacks.

Previous studies have explored the use of DRS for the detection of veins [38], [39], boundaries between bone tissue [40], within skin tissue [37], brain measurements [41], and for cancer and pre-cancer detection [42]. These studies tend to make three assumptions: (1) large differences in the optical properties between the layers of

detection, (2) the ability to separate layers using different source-detector spacing, and (3) a homogenous distribution of absorbers. The first assumption is based on large optical property variation between types of tissue. For example, the skull has an absorption coefficient that is orders of magnitude larger than skin tissue. Many previous studies take advantage of these tissue differences when trying to detect distinct layers of tissue. For example, a study for detecting subcutaneous veins estimated the scattering coefficient of blood to be  $57.9 \text{ mm}^{-1}$  compared to a scattering coefficient of  $33.40 \text{ mm}^{-1}$  for the epidermis. When features such as blood vessels are targets of DRS, this assumption is valid, however, this assumption is not valid for evaluating other tissue structures, such as the difference between the dermis and epidermis or between white and grey brain matter. Sublayers of tissue can have similar optical properties, therefore, systems need to be able to distinguish between these layers in order to have spatial resolution. This thesis will explore the capability of a sensor array to distinguish between layers of tissues with as little difference between scattering and absorption coefficients as  $0.25 \text{ mm}^{-1}$ . We have found no previous reports that have shown this capability in a system. With regards to the second assumption, many studies attempting to distinguish different layers of tissue use either different wavelengths [40] or different detectors within a probe [37] to monitor the different layers. To do this, post-processing of the data is necessary to differentiate which portions of the signal come from which layers. For example, a study of bone boundary detection found that each of the tissue

types exhibited very similar spectroscopic curves, so advanced methods of multivariate analysis were necessary to differentiate between the tissues [37].

The third assumption, regarding homogenous absorbers within tissue, is generally valid, but there are some limitations. There are a number of major absorbers in tissue including hemoglobin, myoglobin, glucose and cytochrome c oxidase, most of which are modeled as a homogenous distribution [38]. Oxygen is delivered to tissue via small vessels in a process called microcirculation [38]. Rather than assuming a homogenous distribution of hemoglobin throughout the tissue, it should be confined to these vessels. A multilayer model that takes into account how blood is actually distributed throughout tissue would help increase chromophore extraction accuracy [38]. In a study by Fredriksson et. al., properties were measured within the blood vessels rather than estimating the optical properties [38]. While knowledge of these parameters is important for further analysis of tissue, further knowledge of chromophore concentrations or details of the surrounding tissues cannot be ascertained without extracting the optical properties. Other studies estimating profiles for the depth and thickness of veins have found that they can estimate the depth, but that the accuracy of vein thickness extraction is poor [39]. To complete the model by Fredriksson et. al., a good estimate for both depth and thickness are necessary.

This thesis demonstrates how a multipixel array can be used to detect buried layers of tissue both when the buried layer has distinctly different optical properties and

when the optical properties are similar, addressing the limitations of currently reported fiber systems. This thesis also examines optical property extraction accuracy as a function of the number of pixels used, and determines how many pixels can be used to target a given layer, again addressing the limitations of reported fiber systems.

## **2.8 Conclusions**

Diffuse reflectance spectroscopy is a non-invasive optical interrogation technique that can be applied to the classification of tissue and the quantification of tissue composition. Most DRS systems rely on optical fibers for detection, however, silicon PDs have advantages over fiber, as they have a larger numerical aperture and can be designed in patterns optimized for the targeted tissue. Monte Carlo simulations, look-up tables, and PLSR have all been applied to DRS systems for tissue classification in experimental systems that assume the homogeneity of the tissue sample. DRS systems can be designed to enable depth-resolved analysis. Realistic tissues, however, are inhomogeneous and layered, which are both a challenge for DRS systems.

This thesis analyzes the depth resolution of a multipixel Si PD probe using MC and PLSR analyses. For the first time PLSR data is directly applied to SRDRS spectra to extract optical properties rather than using PLSR to first extract latent variables and use them in a machine learning algorithm. By demonstrating that PLSR combined with a spatially resolved probe can be as accurate as other optical coefficient extraction mechanisms, this thesis adds a more computationally efficient option to the field of DRS

for tissue quantification. This thesis also represents the first direct comparison between PLSR and a LUT for a Si PD array. This thesis is the first time that MC simulations have been applied to experimental data from a multipixel Si PD system to show depth analysis in a tissue mimicking structure and the detection of buried layers.

### **3. Sensor Fabrication**

This chapter describes the design and fabrication of a custom array of Si PN junction photodiodes (PDs). Simulations to determine PD width and the characterization of fabrication processes are discussed. Finally, a complete process flow for the fabrication of the sensor array is provided and the characterization of a fabricated array is presented.

#### **3.1 Sensor Design**

The following section presents the design process for a Si PN junction PD array for depth-sensitive tissue measurements. A key advantage of Si PDs in contrast to optical fibers is that they have higher numerical apertures, can be designed for more optimal SNR for specific applications, and can be more densely packed for a higher fill factor. High packing densities can increase the spatial sensitivity of optical property extraction and tissue characterization. Therefore, the array described herein aims to optimize the number of pixels within a given space, with a target SNR. The high packing density must be balanced with the minimum pixel area required for the target SNR. To achieve the target SNR, each pixel must have sufficient surface area to detect enough incident photons to result in a photocurrent with a higher magnitude than the noise floor, which is the back illumination current. The back illumination current is measured with illumination but without a sample under test (i.e. no reflected signal), and includes the dark current. In designing the PD sensor, there is a tradeoff between PD packing

density and necessary PD width to achieve the target SNR. The resulting sensor has 32 concentric PDs of varying widths surrounding the aperture (round white area) through which the photons are incident upon the tissue, as shown in Figure 5. The PDs take the form of rings in four groups of eight with each group having a different PD width. The inner eight PDs are 50  $\mu\text{m}$  wide, the next set are 100  $\mu\text{m}$ , the PDS in the third set are 250  $\mu\text{m}$  wide, and the outer set of 8 PDs have a width of 500  $\mu\text{m}$ . Each PD is separated by 7  $\mu\text{m}$  of  $\text{SiO}_2$ .

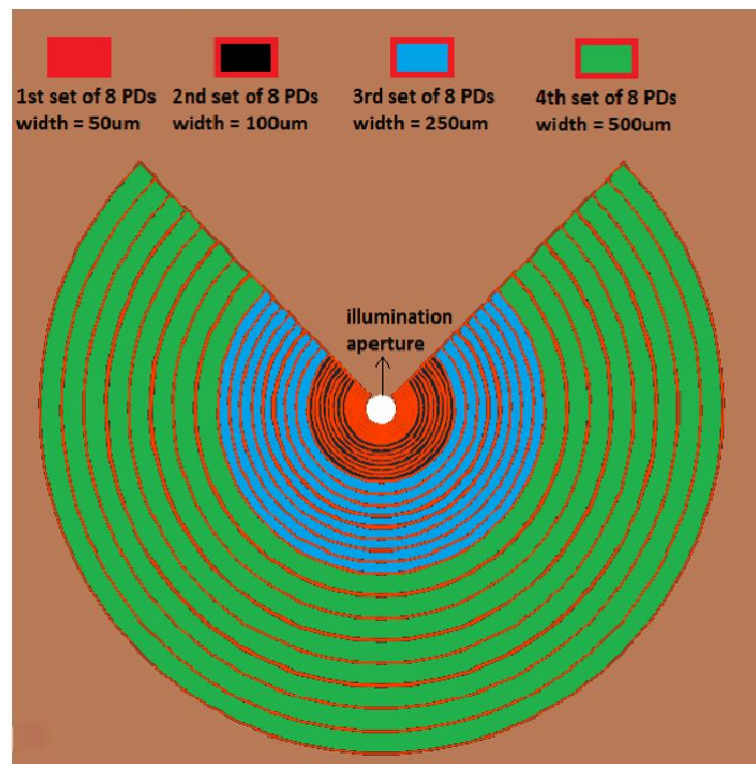


**Figure 5: Pixel Configuration of 32 Pixel Si PD Array Designed Herein**

The sensor array described herein is based on a 24 pixel sensor originally designed and fabricated by Dr. Ozlem Senlik for tissue characterization [12]. The design

process for the 24 pixel sensor is similar to the method presented here; however, Dr. Senlik based her design on the optical properties of skin tissue rather than both skin and muscle.

The general design process of a spatially resolved system is based upon light penetrating deeper into tissue samples, then re-emerging further from the point of entry than light remaining close to the surface. Fewer photons emerge at larger source-detector spacing, decreasing signal strength. Therefore, the outer PDs must be larger than the inner ones in order to maintain the same SNR. The design process presented in this section explores expanding the original design of the PD sensor to increase the depth-sensitivity of the system. Herein, the initial Senlik sensor is expanded to enable muscle and fatty tissue evaluation. The result is an additional set of 8 pixels of 500  $\mu\text{m}$  width for a total of 32 pixels (Figure 5).

Zemax©, a commercial ray tracing program, was used to perform a series of MC simulations to optimize a sensor for the measurement of skin, muscle, and fatty tissues. These simulations were used to decide the width and number of detectors necessary at different radial distances from the source. As optical properties are highly tissue specific, sensors can be designed for a variety of applications. The overall width of the sensor was such that the photons incident from the tissue at the outer PDs will be transmitted through skin and some muscle or fatty tissue, which the inner PDs will have a more shallow optical path through the tissue, likely transmitted through only skin. The optical tissue parameters used in the simulations are shown in Table 1 and are based on published skin

and muscle tissue optical coefficients [43]. As optical tissue properties can vary based on the specific tissue sample being interrogated, four sets of simulations were performed to determine theoretical results over the range of properties present in the literature.

**Table 1: Optical Tissue Parameters for Sensor Design**

Trial	$\mu_s$ (cm <sup>-1</sup> )	$\mu_a$ (cm <sup>-1</sup> )	$g$
1	6.5	0.1	0.9
2	11.0	0.1	0.9
3	6.5	0.2	0.9
4	11.0	0.2	0.9

To model ray propagation through tissue in Zemax©, a bulk scattering model, the angular distribution of scattering, the mean free path, and the albedo of the tissue are needed. The mean free path and the albedo were calculated using the  $\mu_a$  and  $\mu_s$  pairs in Table 1. The Henyey-Greenstein scattering model was used, where the angular distribution of scattering is given by Equation 3.1 [44]:

$$P(\theta) = \frac{1 - g^2}{4\pi(1 + g^2 - 2g \cos \theta)^{\frac{3}{2}}} \quad \text{Equation 3.1}$$

Studies have demonstrated that scattering in tissues without very high  $\mu_s$  generally follow the Henyey-Greenstein scattering model [44]. The anisotropy factor,  $g$ , was constant for all four trials. For skin and muscle tissues the average anisotropy factor is between 0.75 and 0.95 [43]. A previous study showed that the choice of the anisotropy

factor between 0.75 and 0.9 resulted in a less than a 1.5% change in the detected power for similar simulations [12].

The number of photons emerging from the tissue as a function of radial distance from the source can be extracted from the Zemax© MC simulations. The 525  $\mu\text{m}$  thick Si wafer was modeled in addition to the light source and the bulk tissue. The simulations assumed that the tissue appeared infinite to the source in all directions; therefore, no edge effects were considered. Figure 6 shows the ray tracing output from one of the Zemax simulations. One million rays were simulated in each run, however, for clarity, only 100 are shown in the figure.

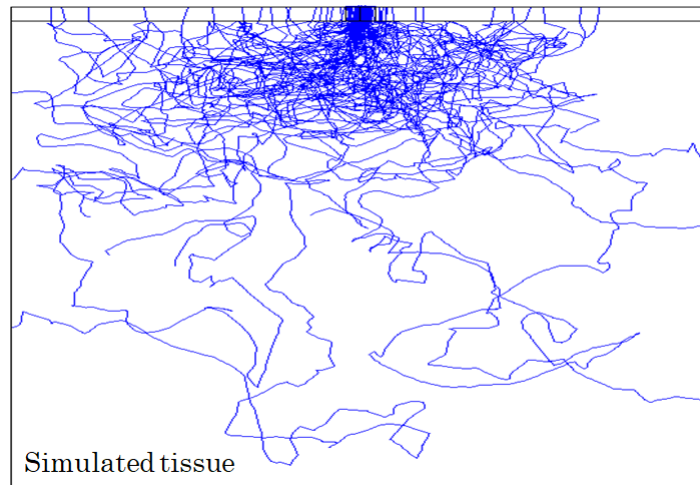


**Figure 6: 100 Rays Simulated in Zemax for the Design of the Multipixel Array Herein**

The inputs to the Zemax model were measured or taken from the literature, as in Table 1. Using a power meter, the power emitted from the optical fiber was measured to determine the source power used in the simulations. At a wavelength of 600 nm, the

source power was  $2.5 \mu\text{W}$ . The numerical aperture of the fiber used in the experimental setup and the Zemax© model was 0.39 as given by the specifications of the optical fiber. For detection as a function of radial distance from the source, the model included a series of  $10 \mu\text{m}$  wide concentric simulated detectors. Ten simulation runs were traced to obtain a mean and standard deviation of the optical power collected at each detector. Figure 7 shows the collected power as a function of distance from the optical input aperture for each set of simulations. As the radial distance increased, the amount of power collected by each detector significantly decreased. Therefore, to obtain the target SNR and associated minimum photocurrent, larger detectors were necessary as the distance from the source increased.

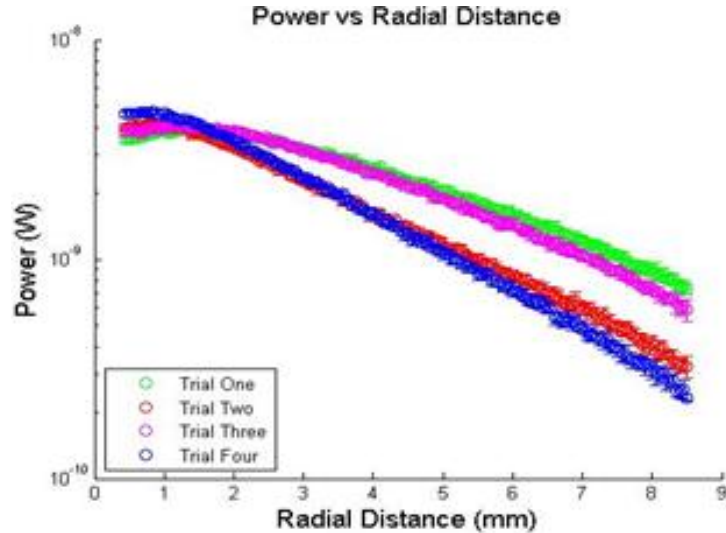


**Figure 7: Simulated Power vs Radial Distance for Four Optical Property Pairs**

The SNR of the PD array was used to optimize the width of the sensor PDs. The collected power at each  $10 \mu\text{m}$  slice of simulation detector was integrated across the

entire detector width for the inner 24 pixels (eight each of 50  $\mu\text{m}$ , 100  $\mu\text{m}$ , and 250  $\mu\text{m}$  pixels) to obtain the power collected by each pixel. Previously published PD responsivities using the same fabrication techniques from the Jokerst group [10] were used to convert power to photocurrent. The photocurrent was calculated for a wavelength of 600 nm, which is in the center of the intended measurement range (400 nm - 800 nm).

To design this structure it is important to have a targeted SNR to determine the area of the pixel. Previous studies have used a minimum SNR of 20 dB in the design of systems for the extraction of optical properties [12]. The noise floor is set by the back illumination current, which results from light detected by the sensor array before the light penetrates the tissue. When the structure studied herein was designed, the back illumination current of the structures was unknown, however, the dark current density of other multipixel PD devices of similar structure was known, and was used as the noise floor for the design calculations herein. Previously fabricated PD devices in the Jokerst Research group show that for wavelengths less than 750 nm, the dark current and the back illumination current were similar except at the inner 3 pixels [12], but this did not negatively impact the results, since the signal levels were higher than the noise floor for these 3 inner pixels, as described later herein. The previously fabricated similar PD devices had dark current densities ranging from 0.17 – 156 pA/mm<sup>2</sup> [12]. A maximum dark current density of 156 pA/mm<sup>2</sup> was used for SNR calculations in the

simulations herein. To obtain the desired SNR (minimum 20 dB), the target photocurrent minimum is 250 pA. The equation used to calculate SNR is given by Equation 3.2:

$$SNR = 20 \log \left( \frac{\text{mean}(I_{ph} - I_{bi})}{\text{std}(I_{ph} - I_{bi})} \right) \quad \text{Equation 3.2}$$

Where  $I_{ph}$  is the photocurrent, and  $I_{bi}$  the back illumination current. For this design, note again that the back illumination current is not used, but instead, the dark current is used as the noise floor.

In addition to the minimum SNR consideration, a second consideration was the target optical penetration depth of the photons sensed by the PD array. As described in Chapter 2, the photon penetration depth is approximately 1/3 of the source/detector spacing. The design target optical penetration depth was 2.5 mm, so as to sense muscle tissue through the skin, where human skin ranges depending on body location but can be as little as 2 mm thick [45]. Thus, the PD detector array would need to be approximately 7.5 mm in radius.

The structure was then designed with the minimum SNR and sensing depth criteria. For the outer eight pixels, pixel widths between 250  $\mu\text{m}$  - 600  $\mu\text{m}$  were modeled using MC simulations and the photocurrent and SNR of each pixel was calculated. To collect photons emerging at larger radii while maintaining the minimum target SNR of 20, 500  $\mu\text{m}$  wide pixels satisfied the SNR criterion, but resulted in a PD array with a radius of 7 mm (target 7.5 mm). However, due to the cost of phantom materials, the 7

mm radius PD array was chosen as acceptable. Using this width for the outer eight pixels of the PD sensor, the simulated photocurrents for the four different sets of optical properties in Table 1 were calculated (Figure 8). All simulated photocurrents are above the desired 250 pA level targeted in the design of the array, resulting in a simulated SNR above 20 dB.

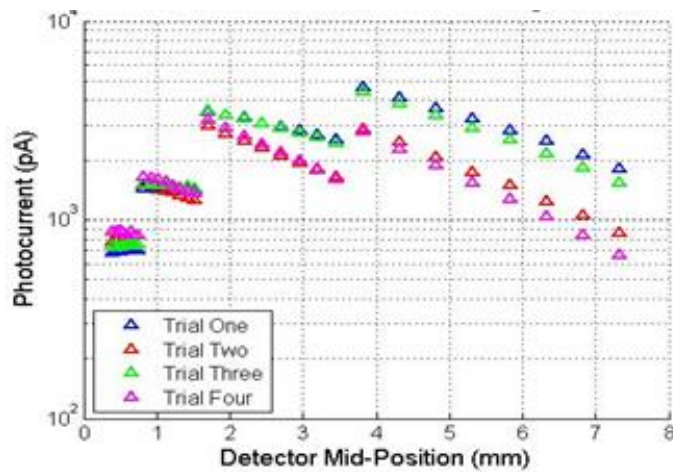


Figure 8: Simulated Photocurrent for 32 Pixel Si PD Array

### 3.2 Junction Depth Optimizations

A completed PD sensor includes the diffusion of p-type junctions into a n-type single crystal bulk Si wafer with an n<sup>+</sup> epilayer, with contacts added to the device for the collection of the generated photocurrent. The quality of the junctions and the contacts affects the performance of the sensor. The junction depth, doping levels of the junction, the doping at the back contact, and the resistance of the contacts all affect the performance of the PDs. High responsivity and low dark current are needed for high SNR. Given the set of materials available for use, the diffusion of materials into the front

side and back side of the Si wafer were optimized in addition to the contact deposition. The optimization process will be presented in this section.

To determine the optimum junction depth for the pn photodiodes, Silvaco Atlas© was used to simulate the pixels of the sensor. The four different diode widths (50, 100, 250, 500  $\mu\text{m}$ ) were all simulated. Figure 9 shows the responsivity as a function of wavelengths for seven junction depths for the 100  $\mu\text{m}$  PDs. The responsivity was

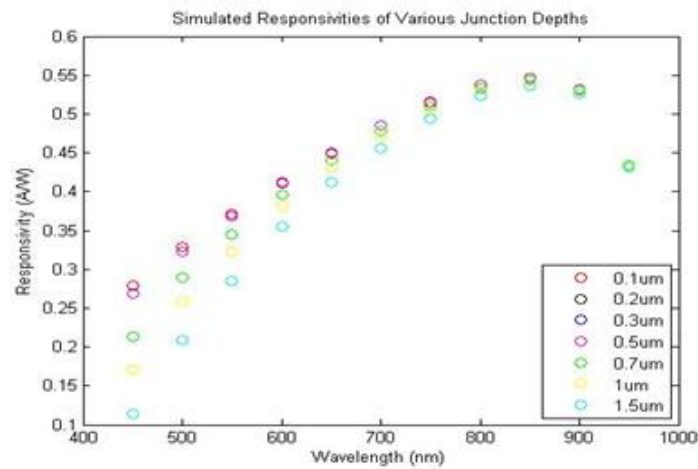


**Figure 9: Responsivity for Different Junction Depths as a Function of Wavelength Simulated in Silvaco**

calculated for wavelengths between 450 nm and 950 nm. As can be seen, a junction depth of 0.1  $\mu\text{m}$  had the highest responsivity at all wavelengths. Therefore, this junction depth was targeted during fabrication. Four diodes were fabricated with four different anneal times and temperatures to achieve four different junction depths. The sheet resistance of the Si after diffusion was measured to verify the junction depth. Four

contacts points were used to measure the sheet resistance using a four point probe system (Signatone S-302-4 Four Point Resistivity Probe Station). Using

**Table 2: Boron Junction Test Diodes**

	Measured Junction Depth ( $\mu\text{m}$ )	Measured Sheet Resistance ( $\text{ohm/sq}$ )
Diode 1	0.35	32.91
Diode 2	0.66	17.47
Diode 3	0.83	13.80
Diode 4	1.19	9.66

the sheet resistance and the background concentration of the epitaxial wafer ( $7.5 \times 10^{14} \text{ cm}^{-3}$ ) the junction depth was calculated. These measurements were used to calculate the surface concentration of the borosilica dopant which is  $6.5 \times 10^{20} \text{ cm}^{-3}$ . Based upon this calculated surface doping, an anneal time and temperature of 1000 degrees C for 12 minutes was then chosen to achieve the desired junction depth of  $0.1 \mu\text{m}$ . This was verified by the fabrication of a fifth diode using these parameters. The measured sheet resistance of the final diode corresponded to a junction depth of  $0.1 \mu\text{m}$ .

### **3.3 Sensor Fabrication Process Flow**

The process for the PD multipixel sensor fabrication consisted of three main sections: pn junction formation, metal contact deposition, and the aperture etch. These three processes will be explained in this section.

The process for the PD sensor fabrication used a Si epilayer structure, followed by doping. The PD structure was fabricated using a  $525 \mu\text{m}$  thick n/n<sup>+</sup> Si epitaxial wafer.

The n-type bulk Si was doped with Sb with a resistivity of approximately 0.01  $\Omega$ -cm ( $4 \times 10^{18} \text{ cm}^{-3}$ ) (University Wafer) as per the specifications. The 7  $\mu\text{m}$  thick epitaxial layer was phosphorus doped with a resistivity of 6  $\Omega$ -cm ( $7.5 \times 10^{14} \text{ cm}^{-3}$ ). To begin the processing, the wafer was RCA cleaned to remove organic contaminants and ionic impurities on the surface of the wafer. Immediately following the RCA clean, the wafer was placed in a Tempress furnace at 1000 degrees C for five hours to grow a thermal oxide targeted at a 146 nm thickness. The backside oxide was subsequently removed using buffered oxide etch (BOE), and a phosphorosilica spin-on-glass (SOG) with a surface concentration of  $1.2 \times 10^{20} \text{ cm}^{-3}$  was spun onto the backside of the wafer (the non-epitaxial side). The dopant was diffused into the sample by placing it in the Tempress furnace for 30 minutes at 1050 degrees C. The phosphorosilica glass was then removed using BOE, and a 2  $\mu\text{m}$  thick PECVD oxide was deposited to protect the backside of the wafer during further processing.

To form the pn junctions on the epitaxial side of the wafer, the thermal oxide was patterned and etched. The etch was performed using a two-step process combining a dry and a wet etch. Reactive ion etching (RIE) using  $\text{CHF}_3$  was used to thin the thermal oxide, but to avoid pitting on the surface of the Si that could increase the dark current in the device, the etch was completed using BOE. BOE cannot be used for the entire etch because it will undercut the thin 7  $\mu\text{m}$  oxide barrier between the PDs. After the thermal oxide was etched, borosilica SOG (Filmtronics B155) with a surface concentration of

$6.5 \times 10^{20} \text{ cm}^{-3}$  was spun onto the front side of the wafer. The wafer was placed in the furnace at 1000 degrees C for 12 minutes to complete the doping of the junctions. The resulting junction depth was 0.1  $\mu\text{m}$  as determined by the previous section. The borosilica SOG was then removed using the previously described two part dry and wet etch sequence.

After the junctions were formed, three metal depositions occurred: the top contacts, the leads, and the back contact. First, the Al (100 nm)/Ti (50 nm)/Ni (50 nm)/Au (200 nm) top contacts were deposited using e-beam evaporation. After patterning the top contacts, the leads were deposited and patterned: Ti (50 nm)/Ni (50 nm)/ Au (150 nm) using e-beam evaporation. Standard negative photolithography and liftoff in acetone removed the unwanted metal after both of these depositions. After the wafer was diced to the final dimensions, Ti (50 nm)/Ni (50 nm)/Au (150 nm) was broad area e-beam evaporated onto the backside of the wafer to form the backside contact. The back contact was deposited after dicing to avoid peeling of the back contact. The edges of the sample were protected to prevent metal curling around the device during metal deposition.

Optimization of the back contact was performed to decrease the resistance at the back contact and to maximize the device responsivity. When making contact between a semiconductor and a metal, an ohmic contact with a low contact resistance is critical for optimal signal capture and to reduce device heating [21]. High resistance at the contacts

leads to a large portion of the energy being converted to heat rather than being extracted as an optical signal. Low resistance contacts therefore increase the conversion of optical to electrical energy. Ohmic n-type contacts are obtained when a high level of n-type doping (in this case phosphorus (P)) exists at the Si/metal junction. The backside of the Si wafer was doped with phosphorosilica spin-on-glass (Filmtronics, P507) with a surface concentration of  $1.2 \times 10^{20} \text{ cm}^{-3}$ . Anneal times and temperatures for five test diodes that were fabricated and measured for this thesis are presented in Table 3. A Ti/Ni/Au

**Table 3: Phosphorus Test Diodes**

	Anneal Temperature (°C)	Anneal Time (min)
Diode 1	1100	30
Diode 2	1050	30
Diode 3	1100	45
Diode 4	1050	45
Diode 5	1000	14

contact was deposited onto the n-doped Si using e-beam evaporation and the dark currents of the diodes were measured. Figure 10 shows measurements of the dark current. Diode 2, with an anneal time and temperature of 30 minutes and 1050 degrees C had the lowest dark current. This diffusion time and temperature was used in further processing.

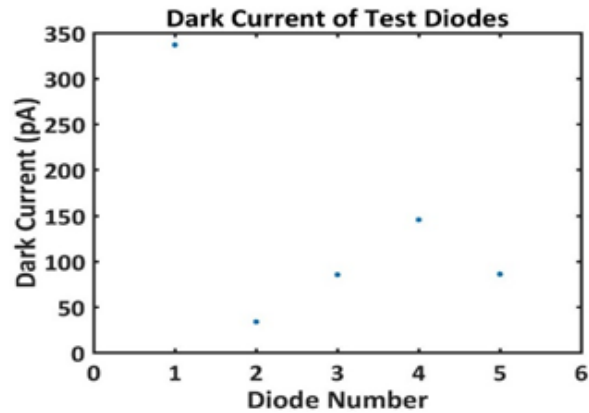


**Figure 10: Dark Current of Phosphorus Test Diodes**

The contacts for the PD array were carefully characterized. Al contacts have a number of desirable characteristics in VLSI processing, including low contact resistivity and ease of deposition [21]. Despite the many benefits of Al, spiking can cause a problem in devices using Al contacts directly on Si with a shallow junction, as is the case herein [21]. This spiking is more likely to occur at higher temperatures. Previous attempts at fabrication found that spiking contributed to large dark currents in the PD devices. Figures 11a and 11b show contacts before and after a high temperature anneal. After the anneal, pitting can be seen in the Al thin film where Al has diffused into the Si. The anneal is aimed at decreasing the resistance of the Al thin film and to increase adhesion of the Al to the Si. On the PD sensor, a portion of the Al contact is covered by, and connected to, the Ti/Ni/Au metal contact that forms the top leads of the device. Due to the potential for junction spiking and a high contact resistance, the dark current associated with a variety of anneal temperatures was tested. Four diodes were measured. These diodes were fabricated using the junction and back contact diffusions

previously discussed. The same mask was used to create all four diodes, giving them an equal surface area. An Al (150 nm) top contacts was deposited on the p-side of each diode using e-beam evaporation. The anneal time and temperatures for each diode are listed in Table 4. A Ti (50 nm)/Ni (50 nm)/Au (150 nm) back contact was deposited on

**Table 4: Al Test Diode Anneal Time and Temperatures**

	Anneal Temperature (°C)	Anneal Time (min)
Diode 1	400	3
Diode 2	420	3
Diode 3	440	3
Diode 4	460	3

the back of the diode using e-beam evaporation. The dark current was then measured by probing the diode under no illumination. The dark current per unit area of each diode can be seen in Figure 11. As can be seen, diode 3 with an anneal temperature of 440

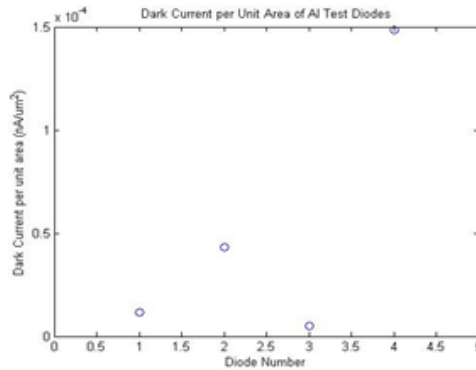


**Figure 11: Dark Current Per Unit Area of Al Test Diodes**

degrees C had the lowest dark current. Despite a low dark current, the repeatability of this anneal was low. For the same recipe in the RTA, roughly 50% of the diodes exhibited significant burning as detected visually. To avoid spiking and damaging the contacts, the metal stack was changed to an Al (100 nm)/Ti (50 nm)/Ni (50 nm)/Au (150 nm) stack. This metal combination did not require an anneal and has been used by the Jokerst Research group for low resistivity p-type contacts on thin film Si PDs. This multilayer metal structure was deposited using e-beam evaporation.

The central round aperture for light transmission from the fiber at the back of the PD array through the PD array and into the tissue was etched in two steps. After patterning the aperture, the oxide was etched using  $\text{CHF}_3$  in RIE. The sample was then placed in a deep RIE for the Si etch. The etch was performed using a Bosch process (DRIE, SPTS Pegasus). Once the aperture was formed, a PECVD nitride was applied as an anti-reflective coating and a surface passivation layer. A packaged sensor array is shown in Figure 12. The entire fabrication process for the sensor is depicted in Figure 13 below.

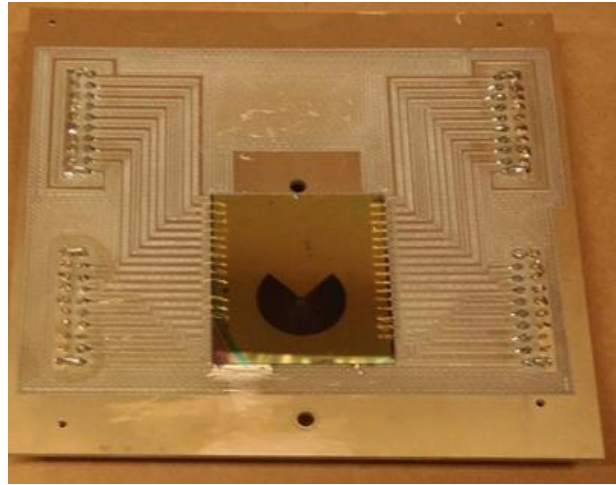


Figure 12: Packaged 32 Pixel Si PD Sensor Array

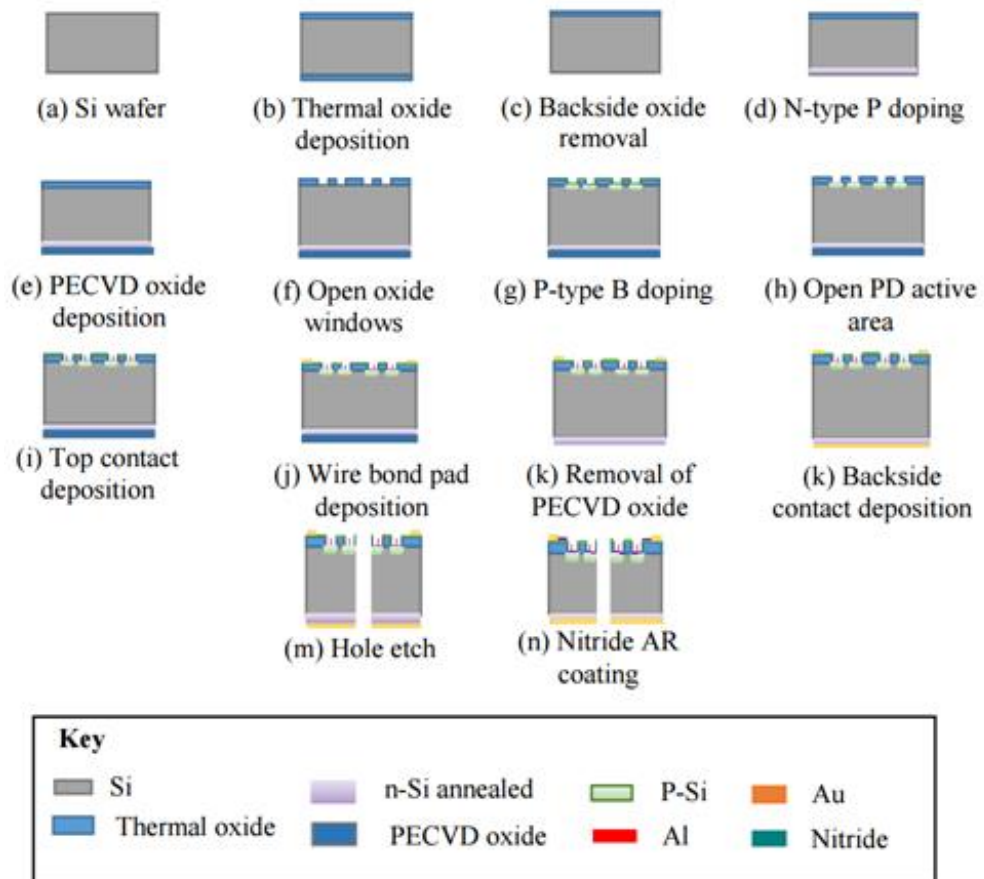


Figure 13: Si PD Sensor Array Process Flow

### **3.4 Sensor Array Characterization**

After fabricating a 32-pixel sensor array, the array was characterized.

Characterization included dark current measurements, back illumination measurements, responsivity and signal (to calculate SNR). Combined, these parameters reflect the applicability of the array for use in DRS measurements. If the dark current or back illumination current is too high, the noise floor will be high, and the lower DRS signals will not achieve the target SNR. A high SNR indicates the array can sense the small signals present in DRS, and that the noise floor is sufficiently low.

To characterize the array, the responsivity, dark current, and the signal-to-noise ratio (SNR) of each pixel was measured. The responsivity was measured by steady state illumination of the pixel at 7 different wavelengths in a dark room using a 300 W Xenon lamp connected to a Newport CS130 monochromator. A 1 mm diameter optical fiber with a numerical aperture of 0.39 delivered light from the monochromator to the sample. The illumination area was completely contained within the responsive area of each PD. The wavelengths used for responsivity testing were: 480 nm, 490 nm, 500 nm, 510 nm, 560 nm, 580 nm and 600 nm. The photocurrent due to illumination was measured using a Keithley SMU-4200 Source-Measurement Unit. The dark current of the device was measured when no light was present. To calculate the responsivity, the responsivity ( $R_{\text{hama}}$ ) and photocurrent ( $I_{\text{hama}}$ ) of a pre-calibrated Hamamatsu photodetector were used as given by Equation 3.3:

$$R_{pix} = \frac{(I_{ph} - I_d) * R_{hama}}{I_{hama}} \quad \text{Equation 3.3}$$

The Hamamatsu device has a known responsivity; therefore, the power with which the pixel is illuminated can be determined from the  $I_{hama}$  and the known responsivity. The responsivities of all functional pixels are shown in Figure 14. Out of 32

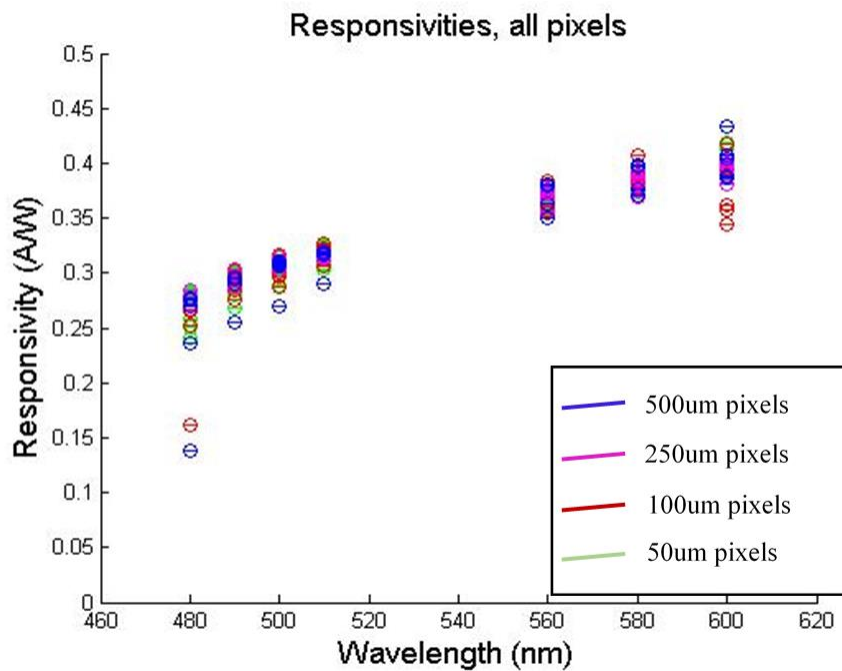


**Figure 14: Responsivity of Pixels in 32 Pixel Si PD Sensor Array**

pixels in the device, 25 pixels responded to illumination. The functional PDs included:

five 500 um, five 250 um, seven 100 um, and eight 50 um detectors. This resulted in a yield of 78.1%. Figure 15 shows the dark current and the dark current per unit area.

There are two pixels showing dark currents that are higher than the surrounding pixels.

Uneven etching during RIE can result in the slight pitting of some pixels, in turn possibly resulting in a higher dark current for those pixels.

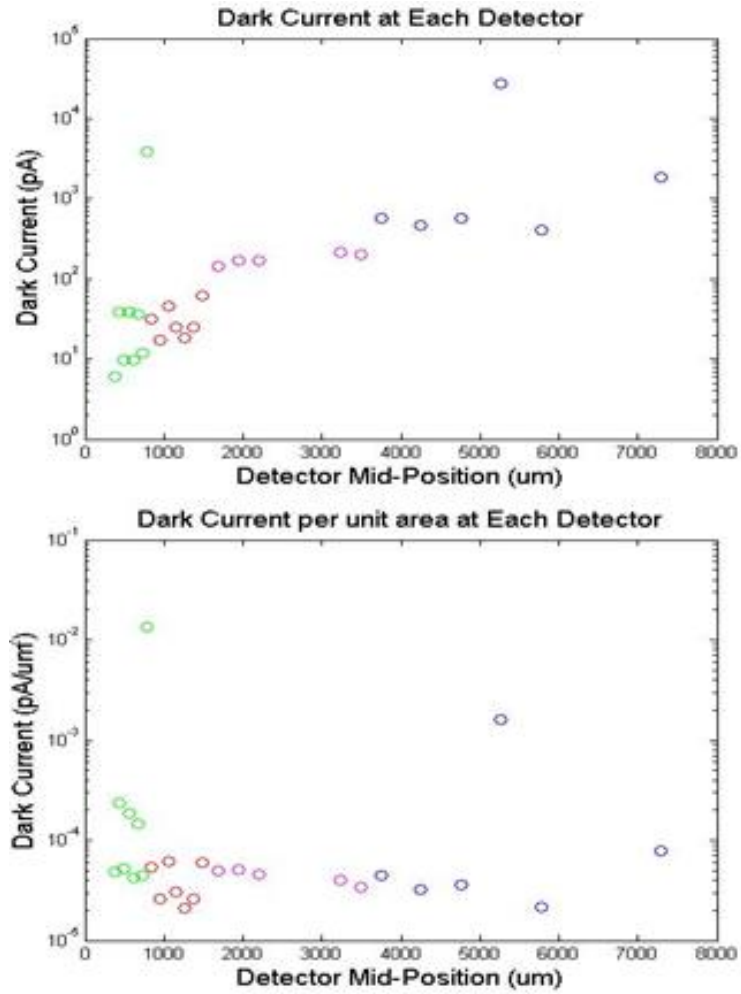


**Figure 15: Dark Current and Dark Current per Unit Area of 32 Pixel Si PD Sensor Array**

To calculate the SNR of each pixel, the array was illuminated from the backside using the 1 mm diameter fiber attached to the monochromator and the 350 W Xenon lamp. Instead of a sample, a 99% Spectralon reflectance standard was used to reflect

light onto the array. The fiber was aligned to the center of the illumination aperture, and this alignment was repeatable, as shown in Chapter 5.

The mean and standard deviation of the photocurrent were calculated using 10 consecutive photocurrent measurements. Measurements were for wavelengths ranging from 400 nm to 800 nm in 10 nm steps. SNR is calculated as in Equation 3.4:

$$SNR = 20 * \log\left(\frac{signal}{noise}\right) = 20 * \log\left(\frac{I_{ph}}{\sigma}\right) \quad \text{Equation 3.4}$$

A target SNR of 20 dB was used for the PDs in the sensor array. All pixels had an SNR greater than this value, as seen in Figure 16. Of the 25 functional pixels, 11 had an SNR greater than 40 dB. Of the remaining pixels, 22 had an SNR greater than 30 dB.

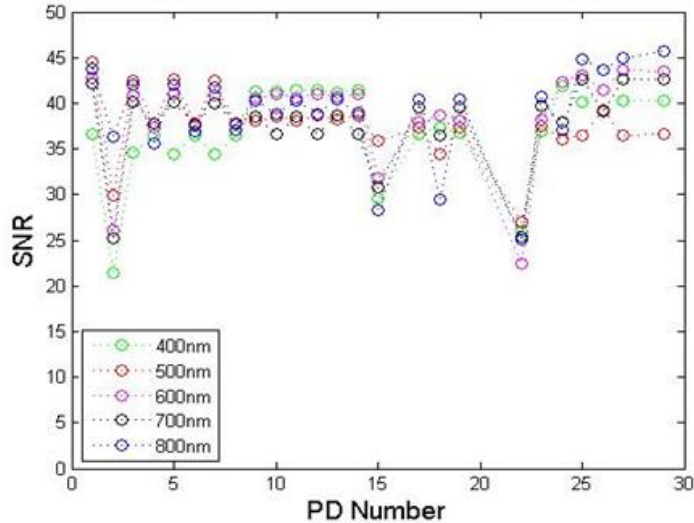


**Figure 16: SNR of Pixels in Si PD Sensor Array for Wavelengths between 400 nm - 800 nm**

The array fabricated herein demonstrates that the fabrication process described in Section 3.2 can produce an array with low dark current, high responsivity and high

SNR, although the array PD yield was only 78%. A 32-pixel device is optimal for sensing deeper within tissue compared to devices with lower source-detector spacing. However, due to testing constraints, a 24-pixel device was used for the measurements in subsequent chapters. The solid phantoms available for the experiments had a radius smaller than the outer radius of the 32-pixel array, thus motivating the use of the 24 pixel array. For optical measurements, phantoms should be semi-infinite to avoid scattering from the edges of the phantoms. To meet this requirement, it is necessary to use a smaller device, again motivating the use of the 24 pixel array. The device which was used for the phantom measurements was fabricated using a very similar process to the one described above. Of the 24 pixels of the device, 18 were functional at the time of testing.

### ***3.5 Conclusions***

This chapter presents the design, fabrication, and characterization of a 32 pixel sensor array. The array is composed of Si pn junction diodes optimized for sensing in skin and muscle tissue. The characterization of the 32 pixel sensor array demonstrated a process flow capable of producing photodiodes with high responsivity, low dark current, and high SNR. While this array will not be used in the testing presented in the rest of this thesis, a similar 24 pixel Si pn junction photodiode array was used, and the process flow presented herein is consistent with the fabrication process for the 24 pixel PD array.

## 4. Homogenous Phantom Optical Property Extraction

This thesis applies a multipixel Si PD array as described in Chapter 3 to perform depth resolved analyses of tissue. To accurately assess the spatial resolution of the PD sensor, the system must first be able to accurately extract optical properties from homogenous phantoms. Previous systems have shown the ability to use MC simulations or look-up tables as discussed in Chapter 2 to measure the optical properties of tissue and to classify homogenous liquid phantoms. Chapter 4 discusses the application of a new analytical technique to DRS data measured from homogenous phantoms for the extraction of optical properties: partial least squares regression (PLSR). Previous applications of PLSR to DRS data do not directly use PLSR to extract the optical properties of the sample. These studies instead use PLSR to identify latent variables that are then used in a machine learning algorithm to classify tissue [34]. This thesis represents the first time that PLSR will be directly applied to DRS data for the extraction of optical properties. The strength of the PLSR analysis herein arises due to the large variety of spatial data available from the multipixel Si PD array, and enables, for the first time, the PLSR to more accurately extract the scattering coefficient while greatly decreasing the computational time necessary for optical property extraction.

Partial least squares regression (PLSR) is a linear analysis technique often used in combination with chemical spectra to associate features in the spectra with desired variables. In this chapter PLSR will be applied to SRDRS data from homogenous liquid

phantoms acquired with a multipixel sensor array to predict optical properties. The prediction accuracy will be compared with results using the same spectra combined with a look-up table (LUT) to characterize the phantoms. The prediction accuracy of the PLSR will be analyzed as a function of SNR and the number of detectors used in the analysis. This chapter demonstrates that a technique rarely used for the quantification of optical properties can be more accurate than traditionally used methods in addition to decreasing computation time for the data examined herein. This thesis will demonstrate for the first time the robustness of a multipixel sensor array combined with PLSR to SNR requirements when compared with look-up tables.

#### ***4.1 Partial Least Squares Regression***

PLSR is a regression technique traditionally used in chemistry and recently applied to tissue measurements to quantify chromophore concentrations and other properties of interest [30], [31], [32]. PLSR associates desired output variables (in this case,  $\mu_a$  and  $\mu_s'$ ) with latent features in the optical spectra through a two-stage process. The model is trained in the first stage using acquired data [29]. This step identifies the regression coefficients used to associate the input (optical tissue spectra) and output ( $\mu_a$  and  $\mu_s'$ ) of the system. After the model is trained, the prediction of the variables of interest can occur in stage two [29]. The use of PLSR in combination with DRS data is motivated by the capability of PLSR to quantify parameters of interest using data from complex spectra. As seen in previous chapters, characterization of tissue is generally

based on the knowledge of many components of the system including path length, tissue structure, and the quantity and type of chromophores present. PLSR assumes no prior tissue knowledge. The optical absorption coefficient,  $\mu_a$ , for example, is the sum of all the individual absorbers (chromophores) within the tissue. Many systems seeking to directly calculate  $\mu_a$  must make assumptions about which chromophores will dominate the spectra and therefore do not include all absorbers present. This can lead to overestimations of chromophore quantities. Such assumptions are not necessary in PLSR. A final factor motivating the use of PLSR for tissue measurements is the computational intensity of PLSR when compared with more traditional data analysis methods such as LUTs. Numerical models and LUTs are computationally intensive and do not enable rapid property extraction [34]. In contrast, linear regression methods such as PLSR are less computational intensive and well suited for fast property extraction [46].

This thesis for the first time combines measurements from a multipixel Si PD sensor array with PLSR to analyze optical spectra from SRDRS measurements. In highly absorbing tissues, such as those sometimes encountered in DRS, most photons do not propagate to the surface for collection, and the collected power is low. Detectors placed at large source/detector spacing also suffer from low collected power even when the tissue is not highly absorbing. Low SNR can decrease system performance. The multipixel sensor developed by Senlik et. al. seeks to enhance the SNR of the system by

using Si PDs with a higher NA than optical fibers and by densely packing the array to minimize unused surface detection area [13]. Despite these gains, the SNR can still impact the accuracy of the extraction of tissue optical properties. As shown later in this chapter, the use of PLSR can mitigate the effect of system noise on the ability to extract optical properties.

## 4.2 Experimental Setup

Sixteen liquid phantoms were measured by a custom Si multipixel sensor array for SRDRS composed of 24 semi-annular PDs. The Si PD array was fabricated by Dr. Senlik. Sixteen of the 24 pixels were functional during testing. The array fabrication was described in Chapter 3. The 16 phantoms were prepared in deionized (DI) water using Nigrosin powder (N4754, Sigma Co.) and polystyrene spheres (PolySciences) 1  $\mu\text{m}$  in diameter) for the absorbers and scatterers, respectively. The prepared liquid phantoms were titrated from a single mixed stock solution. The phantoms were illuminated using a 300 W Xenon lamp connected to a monochromator and a light guide (Figure 17). A

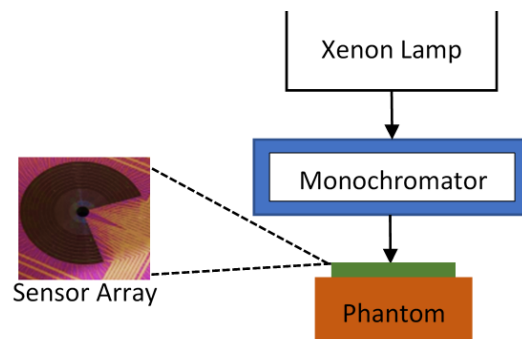


**Figure 17: Experimental Setup for Homogenous Liquid Phantom Measurements**

wavelength range of 400 nm - 800 nm in 10 nm steps was used for all measurements.

The range of optical properties for the prepared phantoms was:  $\mu'_s$  (0.619-2.814  $\text{mm}^{-1}$ ) and  $\mu_a$  (0.242-2.424  $\text{mm}^{-1}$ ). These properties represent a range associated with skin tissue and melanoma [43]. These sixteen phantoms can be grouped into four sets of phantoms containing 4 subgroups of phantoms in each set as noted in Table 5. Within a given set (e.g. 1, 2, 3, or 4),  $\mu'_s$  is constant while  $\mu_a$  varies.

**Table 5: Optical Properties of Homogenous Liquid Phantoms**

Phantom Set	Average $\mu'_s$ (mm <sup>-1</sup> )	$\mu'_s$ range (mm <sup>-1</sup> )	Average $\mu_a$ (mm <sup>-1</sup> )	$\mu_a$ range (mm <sup>-1</sup> )
<b>1a</b>	0.752	0.619 – 0.949	0.484	0.242 - 0.689
<b>1b</b>	0.752	0.619 – 0.949	0.926	0.463 - 1.319
<b>1c</b>	0.752	0.619 – 0.949	1.327	0.664 – 1.891
<b>1d</b>	0.752	0.619 – 0.949	1.701	0.851 – 2.424
<b>2a</b>	1.133	0.933 – 1.430	0.484	0.242 - 0.689
<b>2b</b>	1.133	0.933 – 1.430	0.926	0.463 - 1.319
<b>2c</b>	1.133	0.933 – 1.430	1.327	0.664 – 1.891
<b>2d</b>	1.133	0.933 – 1.430	1.701	0.851 – 2.424
<b>3a</b>	1.810	1.489 – 2.284	0.484	0.242 - 0.689
<b>3b</b>	1.810	1.489 – 2.284	0.926	0.463 - 1.319
<b>3c</b>	1.810	1.489 – 2.284	1.327	0.664 – 1.891
<b>3d</b>	1.810	1.489 – 2.284	1.701	0.851 – 2.424
<b>4a</b>	2.230	1.835 – 2.814	0.484	0.242 - 0.689
<b>4b</b>	2.230	1.835 – 2.814	0.926	0.463 - 1.319
<b>4c</b>	2.230	1.835 – 2.814	1.327	0.664 – 1.891
<b>4d</b>	2.230	1.835 – 2.814	1.701	0.851 – 2.424

The liquid phantom  $\mu_a$  and  $\mu'_s$  were known because they were mixed for the experiments. The  $\mu_a$  and  $\mu'_s$  were predicted using PLSR through the leave-one-out method to calculate prediction errors. The leave-one-out validation iteratively uses 15 of the 16 phantoms to predict the 16th. The two-step process of PLSR first requires a subset of the measured phantoms (15 in this case) to be used to create a model of the system.

This step identifies those components in the spectra which best describe the optical tissue properties by finding the most covariance between the spectra and individual optical tissue properties. After the model is created, it is used to predict the properties of the remaining one phantom that was not included in the learning set. The results will be presented in the subsequent sections.

### ***4.3 Prediction Accuracy as a Function of SNR***

The experimental DRS data from these homogenous, liquid phantoms was used in combination with two prediction techniques: a LUT developed by Dr. Senlik [12] and PLSR discussed herein. When the data from fifteen phantoms was used to predict the optical tissue properties of the sixteenth phantom using PLSR, the mean prediction errors for  $\mu_a$  and  $\mu'_s$  were 9.03% and 4.15% respectively. These prediction errors are significantly lower than those resulting from a prediction using a LUT (19.8% and 16.5% for  $\mu_a$  and  $\mu'_s$ ) when no SNR minimum is applied [12]. Figure 18 plots the PLSR predicted verses known mean optical properties of a given phantom. Optical tissue properties are a function of wavelength. The mean optical tissue properties are the mean for  $\mu_a$  and  $\mu'_s$  when averaged across the wavelength range (400 nm – 800 nm). The results herein demonstrate the PLSR may be useful in measurements where there is less signal power in the system.

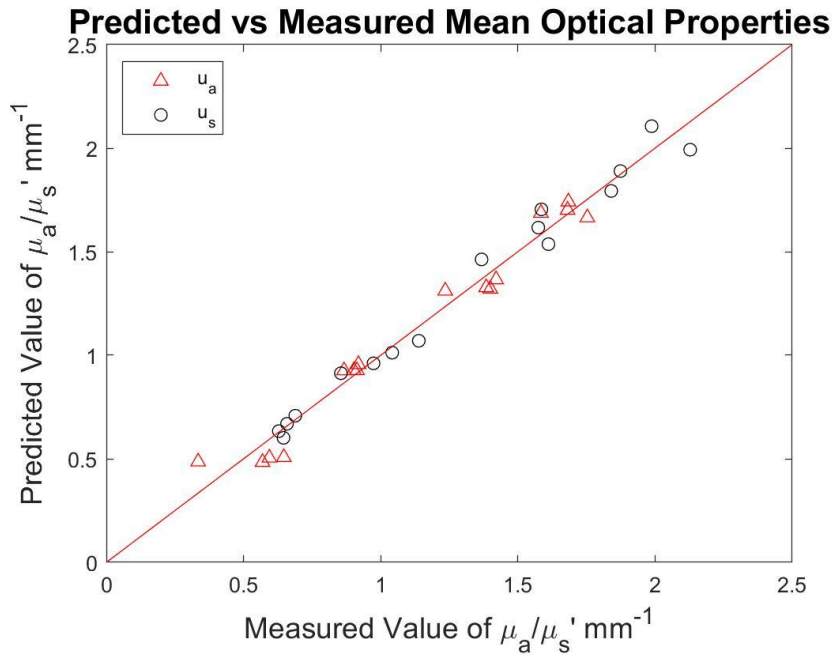


**Figure 18: Prediction Results for Leave-One-Out Prediction Using PLSR**

To assess the impact of SNR on the extraction of the optical coefficients, a test applying a minimum SNR to the data analysis was used to determine the robustness of the PLSR and LUT approaches for low SNR. The results for both PLSR and LUTs can be seen in Figure 19. When a minimum SNR is applied to the LUT analysis, a sharp increase in prediction accuracy is noted as the minimum SNR increases. In contrast, PLSR demonstrates similar prediction accuracies across all SNRs, indicating that it is more tolerant to low SNR data. Both the LUT and PLSR approaches show a slight decrease in prediction accuracy for a minimum SNR of 30 dB. The decrease in prediction

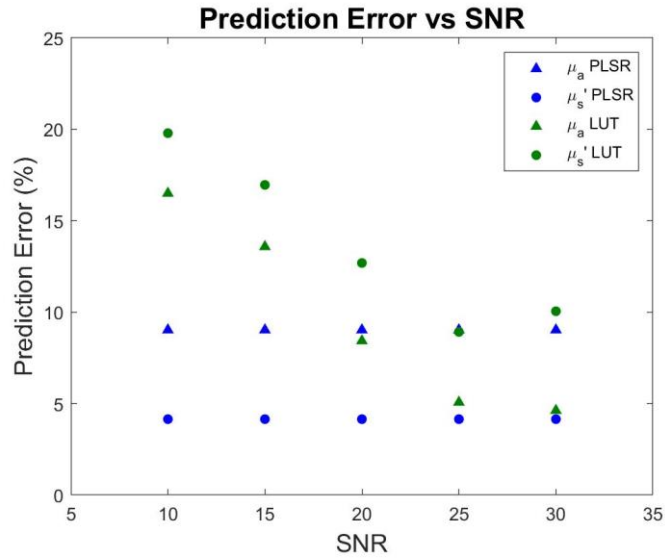


**Figure 19: Prediction Error as Function of SNR for LUTs and PLSR Analyses**

accuracy is likely due to a decrease in the amount of data being used to train the system for the particular case analyzed herein, as seen in Table 6. Table 6 shows a significant decrease in the amount of data being used between a minimum SNR of 25 dB and a minimum SNR of 30 dB. If more data were available at an SNR above 25 dB, the decrease in prediction accuracy between a minimum SNR of 25 dB and 30 dB (as noted in Figure 19) might not occur.

**Table 6: Percent of Data Used in SNR Analysis for Given Minimum SNRs**

Min Allowed SNR	Percent Data Allowed by Min SNR
10	99.0%
15	97.8%
20	95.3%
25	90.2%
30	82.0%

#### 4.4 Prediction Accuracy as a Function of Number of Detectors

The effect that the number of pixels has upon the PLSR analysis is explored herein. Most DRS systems use a small number of fibers (around 6) for the collection of data [37], [38], [40]. With a densely packed multipixel array, we can collect data from more source/detector spacings than previous studies. For the following analysis herein, a minimum SNR of 15 dB was used. Using this SNR limit the number of detectors used to predict the phantom optical properties was decreased. The number of detectors and the detector numbers that were used for the analysis are shown in Table 7 and the results

**Table 7: Detectors used for Prediction Accuracy as a Function of Number of Detectors Analysis**

Number of Detectors	Detector Numbers
3	6, 13, 21
6	5,8; 11, 15; 18,21
9	5, 6, 8; 9, 11, 15; 18, 21, 23
12	5, 6, 7, 8; 9, 11, 13, 15; 18, 20, 21, 23
16	5, 6, 7, 8; 9, 10, 11, 13, 14, 15; 18, 19, 20, 21, 23

are depicted in Figure 20. As with the SNR analysis, the results demonstrate that PLSR is better at the prediction of  $\mu_s'$  than  $\mu_a$ . Since PLSR is a linear regression technique, it performs best when there are few nonlinearities in the system. As a function of

wavelength, both  $\mu_s'$  than  $\mu_a$  exhibit nonlinearities, however, there is greater nonlinearity in  $\mu_a$  with respect to wavelength compared to  $\mu_s'$ , decreasing the prediction

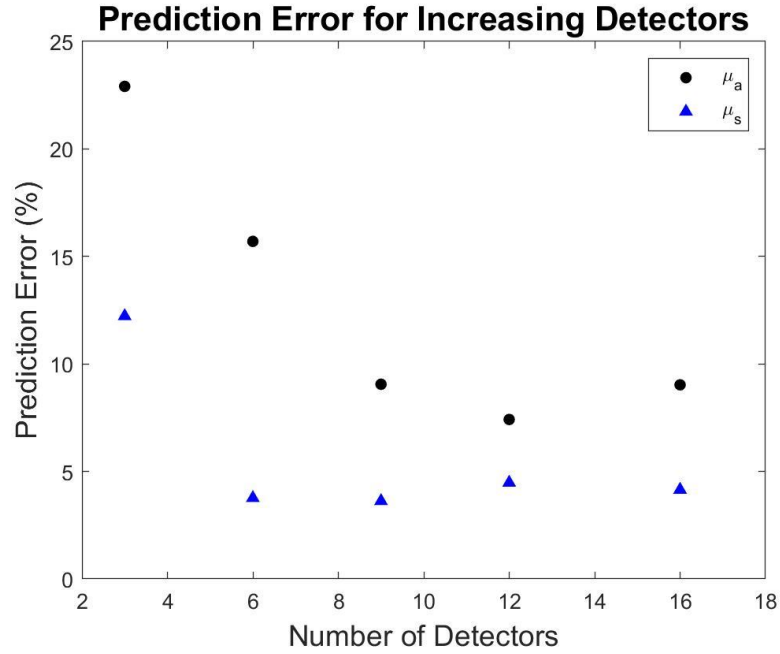


**Figure 20: Prediction Error as a Function of Detector Number Using PLSR**

accuracy [43]. Using more detectors for prediction mitigates the effect of nonlinear  $\mu_a$  on prediction accuracy as seen in Figure 20 up to a 12 detectors. The prediction error increases for 16 detectors because the SNR of the additional detectors is lower than the SNR of the average SNR of the PDs used in the analysis. Figure 20 shows the prediction error decreasing with an increasing number of detectors for  $\mu_a$ . Similar to the case of increasing the minimum SNR discussed above, an increase in the number of detectors used had a greater effect on the prediction of  $\mu_a$  than on  $\mu_s'$  due to nonlinearities in  $\mu_a$  as a function of wavelength. No large increase in prediction accuracy is seen after the use of 9 detectors.

To determine if the source/detector spacing and pixel width influence the prediction accuracy, four detectors from each detector width group were used in the PLSR analysis. A width group is defined as a grouping of detectors with the same pixel width (e.g. 50  $\mu\text{m}$ ). Table 8 indicates which detectors were used for each analysis. Figure 21 shows the prediction accuracy for each of the detector width groups from Table 8.

**Table 8: Detector Numbers from Each Group used in Prediction Error as a Function of Detector Group Analysis**

Detector Set	Detector Numbers
1	5, 6, 7, 8
2	11, 13, 14, 15
3	19, 20, 21, 23

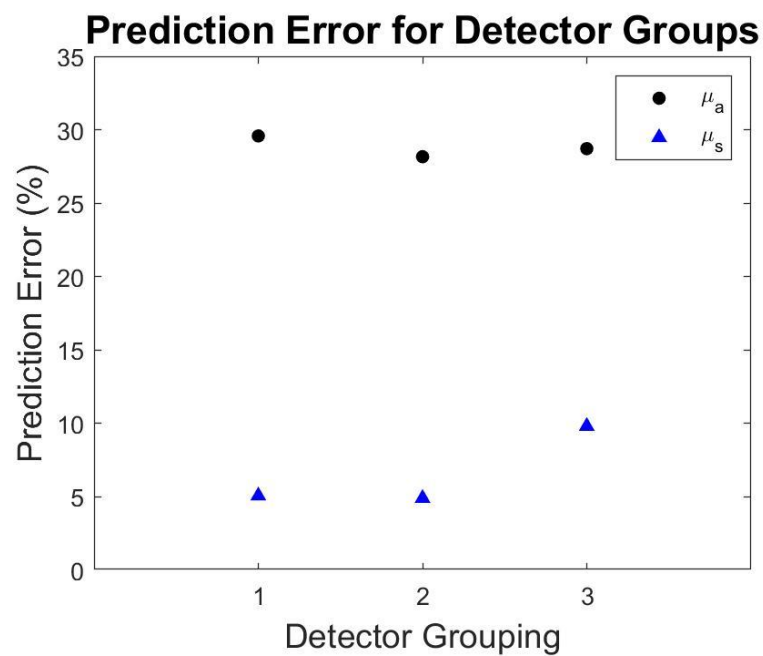


**Figure 21: Prediction Error for Detector Groups using PLSR**

The prediction accuracy does not change as a function of mean source/detector spacing. The outer detectors have a lower SNR than the inner detectors. This leads to a decrease in prediction accuracy for detector group 3 compared to detector groups 1 and 2.

## **4.5 Conclusions**

Chapter 4 presented the first direct use of PLSR on SRDRS data from a multipixel Si PD array for the accurate extraction of optical properties. A multipixel PD sensor array was used to measure liquid phantoms of varying optical properties. These measurements were analyzed using two different data analysis techniques (LUT and PLSR). The robustness of the optical property extraction algorithms as a function of SNR was compared. For low SNR requirements (10 dB) PLSR outperformed LUTs in the both prediction of  $\mu_a$  (9.03% versus 19.8% prediction error) and  $\mu_s'$  (4.15% versus 16.5% prediction error) for this data set. As the minimum SNR increased, the performance of the LUT improved significantly, but PLSR continued to outperform LUTs for the prediction of  $\mu_s'$  (4.15% versus 5.07% prediction error).

The multipixel sensor array was designed to look at tissue properties as a function of tissue depth. The densely packed nature of the array was also designed to mitigate the effects of low system noise on tissue characterization. Comparisons between a fiber system and the multipixel sensor showed that a densely packed array can increase prediction accuracy. However, when measuring homogenous, liquid phantoms it was found that not all the pixels were necessary. When homogeneity is assumed, this

makes sense. The optical tissue properties are not changing as a function of tissue depth therefore we do not expect to need all pixels to accurately extract the tissue properties. When the tissue properties change as a function of depth, then the multipixel array is critical to optical coefficient extraction, as discussed in the next chapter, which will look at the depth sensitivity of the array.

## **5. 2-layer Solid Phantom Experiments and Simulations**

While many DRS studies assume homogenous phantoms, as discussed in Chapter 4, it is critical to move the field forward by exploring measurement and analysis techniques that acknowledge the heterogeneity present within tissues. Chapter 5 explores the depth resolution of the SRDRS Si PD sensor system described in this thesis as a first step towards understanding how the multipixel Si PD array could be used in inhomogeneous media. This chapter will begin with a brief motivation for depth analysis in SRDRS systems. A series of experiments using the multipixel Si PD array to measure two layer, stacked solid phantoms will be presented. These results will be used to develop a theoretical model of the system which will then be utilized in a series of simulations to explore the depth sensitivity of the sensor array. Finally, an analysis of the SRDRS signal as a function of depth for a series of optical properties will be presented.

### **5.1 Motivation**

As mentioned in Chapter 2, depth resolved analysis of tissue has many benefits, including tumor margin assessment [1] and monitoring the velocity of red blood cells within veins [39]. Many current DRS systems focus on homogenous tissue measurements, however, the field has recently been moving towards depth analysis [2-4]. Reported depth resolved SRDRS systems typically use only 6 optical fibers for the measurement of tissue [9], [39], [42]. Chapter 3 discussed a densely packed

photodetector array designed for spatially resolved DRS photon capture from tissue.

This chapter will use a similar 24 pixel array to analyze the depth resolution of a multilayer solid phantom. This thesis is the first time a SRDRS Si PD array has been used for depth resolution within multilayered samples.

There was a distinct increase in optical property extraction accuracy (lower prediction error) when 12 or more detectors were used in the multipixel Si PD array experiments on homogeneous phantoms in Chapter 4. In reported optical fiber devices, the six fibers (which lead to detectors) are used for general DRS measurements, but that number is then reduced when they allocate certain fibers for certain layers in a multilayer phantom [37], [40]. A densely packed sensor array as described in Chapter 3 enables more (all of the) detectors to be used for the measurement of all layers in a multilayer phantom, thus potentially increasing extraction accuracy, as was observed in Chapter 4.

This chapter will also focus on multilayer phantoms with optical properties that do not have large differences between the layers, to observe the sensitivity of the Si PD array sensor to small changes in tissue optical coefficients (or tissue type) that can account for slight inhomogeneities in chromophore distribution within the tissue. This thesis chapter will begin by assessing the depth sensitivity of the multipixel array by measuring multilayer phantoms with thin top layers of variable thickness and optical properties on a thicker, highly absorbing, optically semi-infinite bulk layer. The

experiments on these phantoms will be used to generate an analysis of the SRDRS signal as a function of depth.

## 5.2 Experimental Results

Two layer solid phantoms were constructed and the DRS signals were measured using the 24-pixel photodiode sensor probe previously described herein (Figure 22) [17].

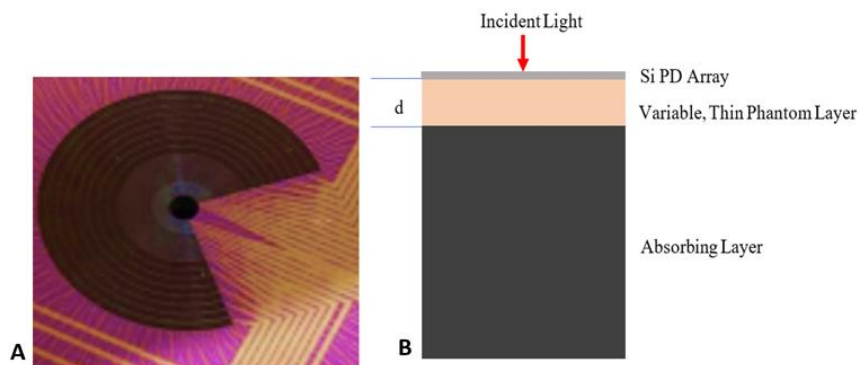


**Figure 22: Experimental Setup for Solid Phantom Experiments (a) Multipixel Si PD Sensor Array (b) Testing Setup with Solid Phantoms**

Solid phantoms were fabricated by collaborators Greening et. al. [47], as follows: a thin PDMS-based solid phantom was prepared using nigrosine powder and titanium dioxide powder. The author created multilayer phantoms by stacking one of these thin phantom onto a thick, semi-infinite, highly absorbing PDMS phantom (fabricated by the Jokerst Research group). The optical properties are detailed in Table 9. This two-layer stack was then measured using the multipixel Si PD sensor array using a 300 W Xenon Lamp connected to a monochromator to transmit 660 nm wavelength light that was delivered through a 1 mm diameter optical fiber. All 2-layer solid phantom measurements were performed on the same day. The optical power incident on the phantoms through

**Table 9: Optical Properties of Sets of Solid Phantoms**

	$\mu_a$ (mm <sup>-1</sup> ) at 600 nm	$\mu'_s$ (mm <sup>-1</sup> ) at 600 nm	Thickness Range (um)
Set 1	0.05	2.0	370-15000
Set 2	0.2	3.0	364-935

the Si PD array aperture was constant, as the lamp, fiber, and PD array alignment was not changed throughout the full series of phantom experiments. The Si PD array had a 750 um illumination aperture (hole), and 18 out of 24 pixels were functional at the time of measurement. For clarity, the semi-infinite phantom will be referred to as the bulk phantom. The thin phantom on the top of the bulk phantom will be referred to as the top layer phantom.

Two different sets of phantoms were used as top layers (Table 9). The bulk layer was the same for all measurements, and all measurements were conducted at a wavelength of 660 nm. The as-fabricated optical properties of the “Set 1” top layer phantoms were:  $\mu_a = 0.05 \text{ mm}^{-1}$  and  $\mu'_s = 2.0 \text{ mm}^{-1}$ . The as fabricated optical properties of “Set 2” phantoms were:  $\mu_a = 0.2 \text{ mm}^{-1}$  and  $\mu'_s = 3.0 \text{ mm}^{-1}$ . Set 1 contained six phantoms ranging in thickness from 370 um to 15 mm. Set 2 contained 5 phantoms ranging in thickness from 364 um to 935 um. The different thicknesses of the two sets of phantom top layers are listed in the legends of Figures 23 and 24. The thin phantoms were fabricated and characterized by collaborators Greening et. al.

The experimental results for the 2-layer solid phantom measurements are shown in Figures 23 (Set 1) and 24 (Set 2). Both the photocurrent and the photocurrent per unit area can be seen in the figures. As described in Chapter 3, as the source/detector spacing increases, it is necessary to increase the pixel width to maintain a minimum required SNR. The sensor array contains three sets of eight pixels. Each set of eight pixels has a different width, with the furthest pixels having a width of 250  $\mu\text{m}$  and inner pixels that are 50  $\mu\text{m}$  wide. This structure causes a discontinuity in the measured photocurrent present at the beginning of each set of 8 pixels when looking at the photocurrent as a function of radial distance. By normalizing the photocurrent to the area of the pixels to obtain the reflectance, the discontinuity is no longer present.

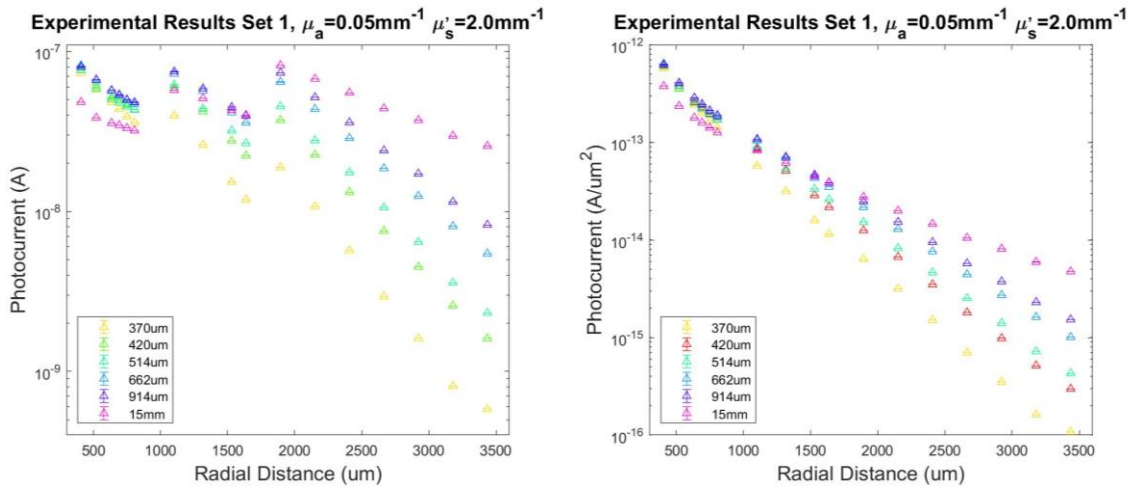


**Figure 23: Experimental Results for 2-Layer Solid Phantoms Measurements Using Set 1 Phantoms**

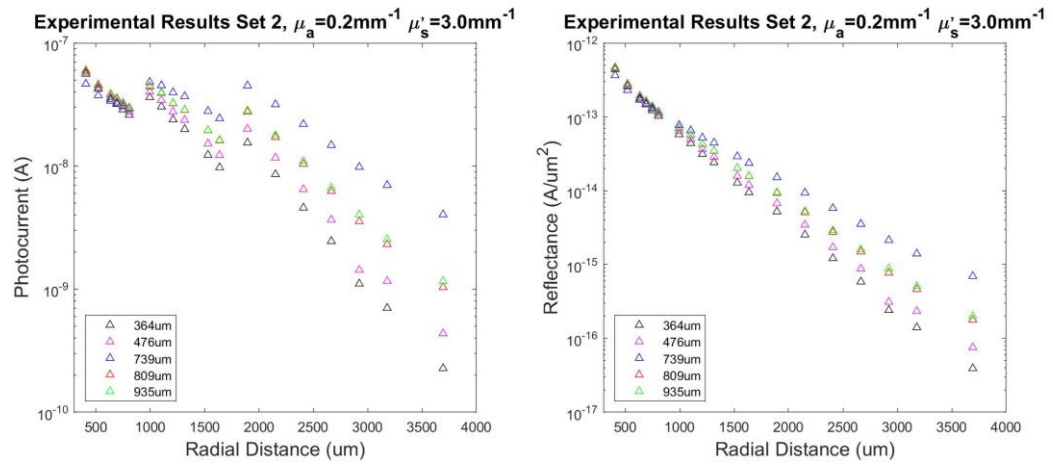


**Figure 24: Experimental Results for 2-Layer Solid Phantom Measurements Using Set 2 Phantoms**

In both Figures 23 and 24, the measured reflectance decreases as the phantom thickness decreases. For very thin phantoms (~100 um - 600um), most photons will arrive at the highly absorbing bulk phantom and be absorbed there. They will not propagate back to the surface of the thin phantom to be collected by the detectors in the sensor array. The presence of the highly absorbing bulk phantom enables the depth sensitivity analysis since most photons interacting with the bulk phantom stop propagating and thus, do not escape the bulk phantom. Therefore, we can assume that the measured reflectance is the reflectance that comes from the top phantom. As the top phantom increases in thickness, more photons hit their maximum depth before hitting the bulk phantom. Photons that reach their maximum depth before interacting with the bulk phantom can propagate back to the surface, increasing the DRS signal. As previously stated, the purpose of this chapter is to analyze the depth sensitivity of the

DRS sensor array. These solid phantom experiments will form the basis for this analysis in subsequent sections.

### **5.3 Simulations vs Experimental Results**

Monte Carlo Zemax© software was used to simulate the experiments performed in Section 5.2. The Si PD array physical characteristics were input to the MC simulation, as were the incident optical signal and the phantom properties and phantom thicknesses. The Henyey-Greenstien phase function was used for the probability distribution of scattering angle and the anisotropy factor was 0.8, which was the anisotropy factor used for the solid phantoms [12]. Three simulations of five million photons each were generated, and the output of these simulations was the optical power at each detector. The average optical power of these simulations was converted to photocurrent so as to compare the simulations to the measured PD array photocurrents. A scaling factor was used to convert the optical power to photocurrent that took into account the responsivity of the pixels and the differences between the simulated power and experimental power. The same scaling factor was used for all pixels and phantoms in the experiments. The scaling factor is mean of the ratios of the experimental photocurrent and the simulated power across the 16 functional PDs (hence the division by 16) given by Equation 5.1:

$$SC = \frac{\sum_{i=1}^{i=24} I_{phantom,experimental}}{\sum_{i=1}^{i=24} P_{phantom,simulated}} \cdot 16 \quad \text{Equation 5.1}$$

Where  $I_{phantom, experimental}$  is the photocurrent measured at a phantom for a given detector  $i$ , and  $P_{phantom, simulated}$  is the simulated power at detector  $i$  for the phantom.

The results for theory versus experiment agree very well, and can be seen in Figures 25 and 26, where both the photocurrents and the reflectances are compared. When the reflectance is calculated by dividing the photocurrent by the areas of the pixels in the 3 groups of pixels, the discontinuities in the photocurrent data are smoothed. The average percent error between the experimental and the simulated data is defined herein by the mean of the errors across all pixels, wavelengths, and thicknesses. The average percent error was calculated using Equation 5.2:

$$Percent\ Error = 100 * \frac{R_{theory} - R_{experiment}}{R_{theory}} \quad \text{Equation 5.2}$$

Where  $R_{theory}$  is the reflectance from the simulation and  $R_{experiment}$  is the measured reflectance. The average percent error between the known phantom  $\mu_a$  and  $\mu_s'$  and the measured values across all pixels and phantoms for Set 1 was 4.63%. The average percent error across all pixels and phantoms for Set 2 was 5.96%.

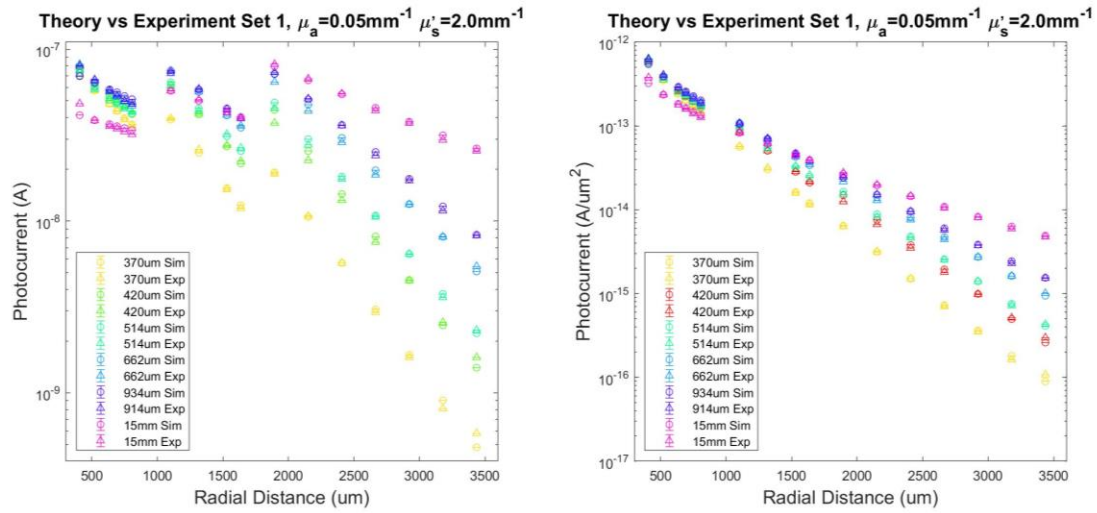


**Figure 25: Theory vs Experiment for 2-Layer Solid Phantom Measurements Using Set 1 Solid Phantoms**

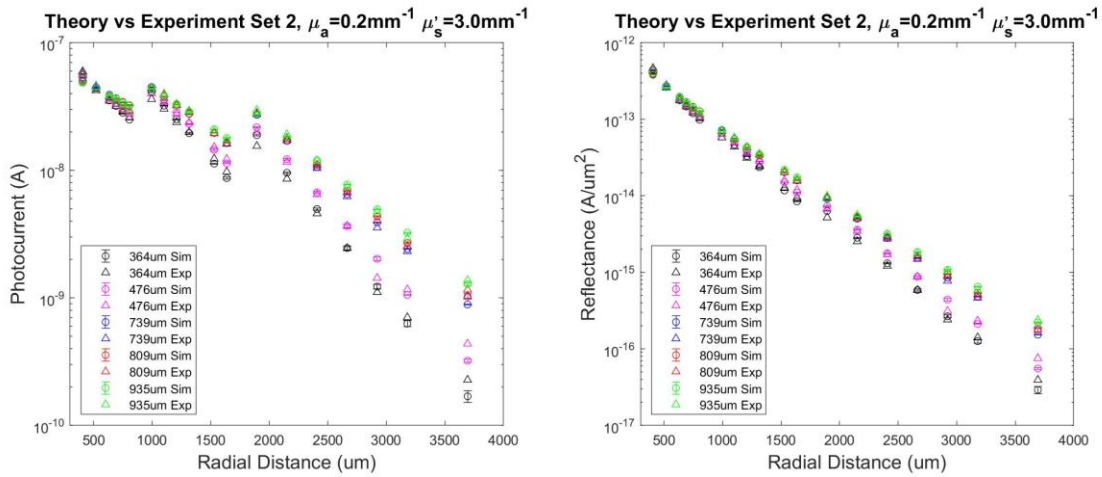


**Figure 26: Theory vs Experiment for 2-Layer Solid Phantom Measurements Using Set 2 Solid Phantoms**

To assess the impact of reflections at the phantom interfaces (top layer to bulk), it is useful to compare the two-layer phantoms to an essentially homogenous phantom that is nonetheless still a two-layer stacked phantom. The 15 mm thick phantom (from Set 1) is an optically semi-infinite phantom, and can be considered a homogenous

phantom. The percent error between simulation and experiment for the 15 mm phantom in comparison to the other two-layer phantoms may yield some insight into the impact of the interfacial reflections of the two-layer phantoms. The 15 mm percent error should not exhibit interfacial reflection in the percent error. Because the percent error was 3.65% for the 15 mm phantom, and the percent errors for the other two-layer phantoms were less than 6%, this indicates that the effect of the interfacial reflection on the percent error is likely not more than a few percent.

## **5.4 Simulations**

The model developed using this experimental data and these simulations was interpolated to simulate two different theoretical simulations spaces, as shown in Figure 27. This was undertaken due to the lack of available physical phantoms for measurements. For the simulations, the top layer thickness ranged from 0.3 mm to 1.4 mm, in 100  $\mu\text{m}$  steps. The bulk phantom was a 15 mm thick highly absorbing phantom for all simulations. The simulations used a Si PD sensor array with a 750  $\mu\text{m}$  aperture, as described in Chapter 3. The simulated photocurrents for Theoretical Space 1 are shown in Figure 28. Note that the simulated phantoms follow the same trends as the experimental phantoms, as discussed above. Unless otherwise stated the analysis in the rest of the chapter uses the simulated phantoms, not the experimental data.

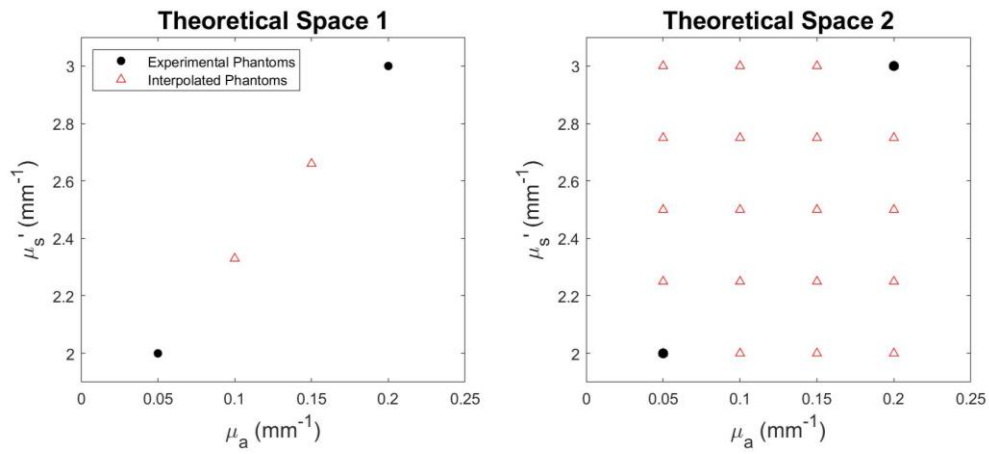


Figure 27: Theoretical Spaces Simulated in Chapter 5

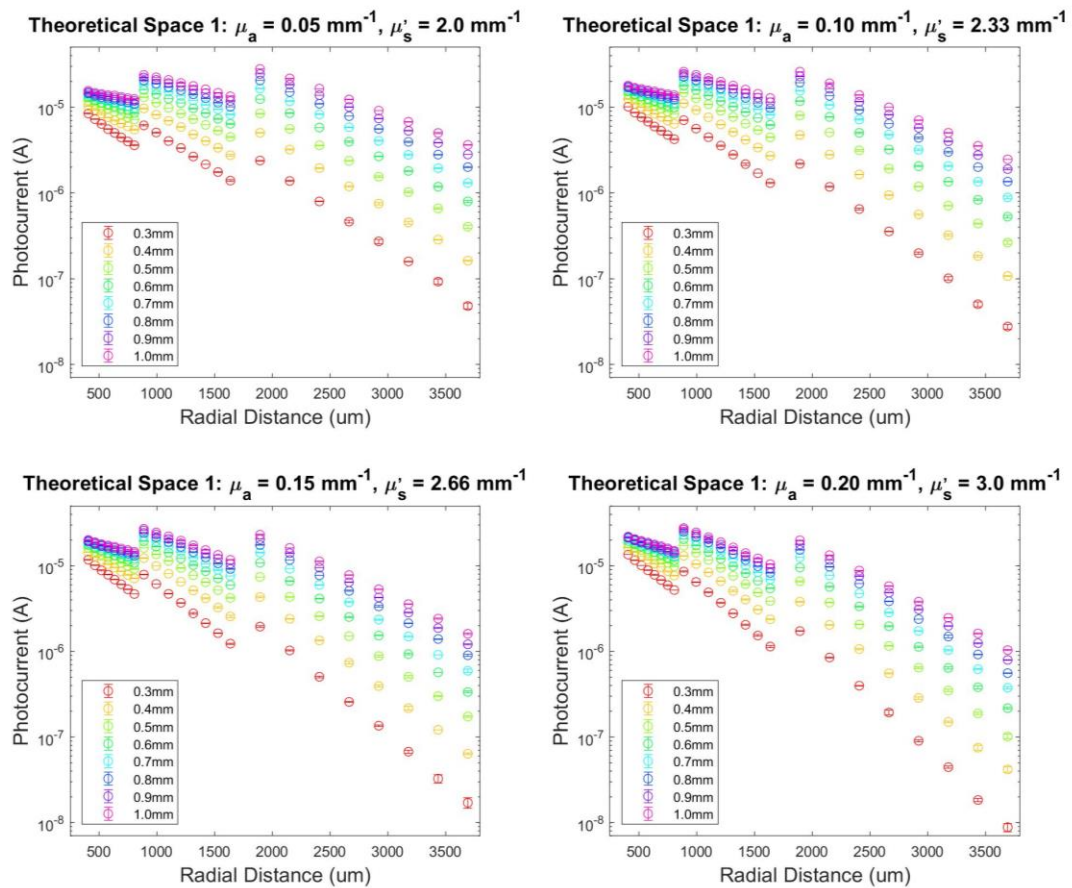
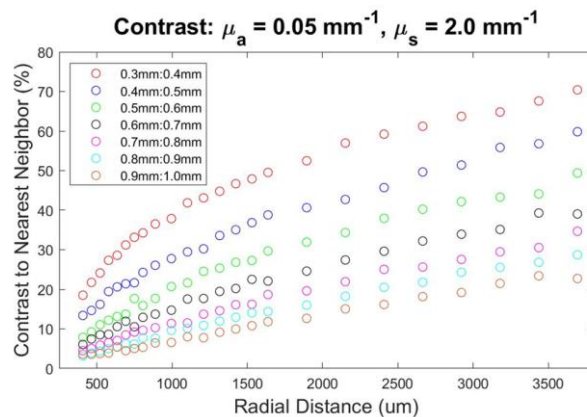


Figure 28: Simulated Photocurrents for 2-Layer Phantoms Using Theoretical Space 1

As the top phantom thickness increases, it is approaching optical semi-infiniteness. When that thickness is reached, we do not expect an increase in DRS signal for further increases in top phantom thickness. This is shown by a decrease in the difference in the diffuse reflectance between phantoms of similar thickness (i.e. 0.3 mm compared to 0.4 mm or 0.7mm compared to 0.8mm). We can see that the difference between the 0.3 mm phantom and the 0.4 mm phantom simulated photocurrent is much greater than the difference between the simulated phantoms of 0.8 mm and 0.9 mm thickness. This trend is reflected in the experimental data as from Section 5.2 as well. In the experimental data, note that very thin phantoms with a 50  $\mu\text{m}$  difference in thickness (e.g. the 370  $\mu\text{m}$  thick phantom and the 420  $\mu\text{m}$  thick phantom from Set 1) show a greater difference in measured photocurrent than the 662  $\mu\text{m}$  thick phantom compared to the 914  $\mu\text{m}$  thick phantom. By calculating the contrast between two phantoms of similar thickness (nearest neighbors), we can see this quantitatively. The contrast for one set of phantom simulations is shown in Figure 29.



**Figure 29: Contrast for a Simulated Set of Solid Phantoms**

Using the knowledge that increasing phantom thickness results in decreasing contrast between phantoms, we can determine the thickness at which the top layer becomes semi-infinite optically. By increasing the thickness of the simulated top phantoms in small increments, we can find the point at which the DRS signal no longer increases (zero contrast at all pixels). This is the point where the phantom has become semi-infinite. This is also the maximum sensing depth of the photodiode array. As previously noted, the DRS signal is dependent on the optical properties of the tissue being interrogated. Therefore, the maximum sensing depth is also dependent on the tissue type and properties. Subsequent sections will use these simulations to analyze the DRS signal as a function of depth.

### ***5.5 Reflectance as a Function of Depth***

Knowledge of photon depth measurement capability for each pixel will eventually permit the evaluation of tissue samples as a function of depth by examining results from individual detectors instead of the array as a whole, as in Chapter 4. If we know the range of locations in a tissue where a photon is most likely arriving from, we can isolate pixels on the array to look at specific layers of tissue. Thus, to evaluate the depth sensitivity of the Si PD sensor system, we can look at the diffuse reflectance signal as a function of depth for each pixel in the array. The DRS signal as a function of depth can also be viewed as the probability that a photon arriving at a detector reached a given

depth. The analysis in this section will be performed using the simulation-generated data described in Section 5.3.

The photocurrent as a function of radial distance curves from Figure 28 can be converted to reflectance as a function of depth for each pixel in the array using the following method. Figure 30 shows the simulation of three different phantoms with the same optical properties in each layer of thicknesses  $T_1$ ,  $T_2$ , and  $T_3$ . We would like to know

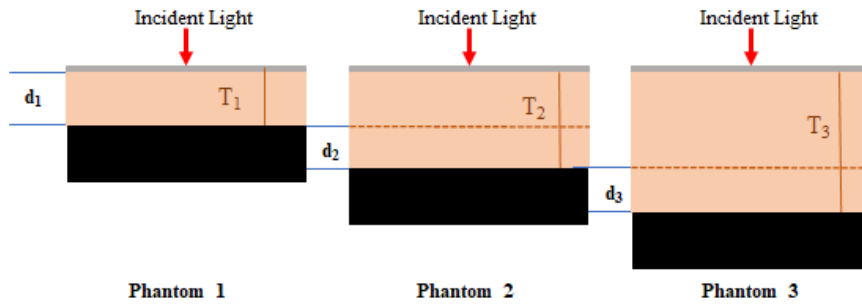


**Figure 30: Simulated Phantom Setup for Creation of Depth vs DRS Signal Curves**

the reflectance through depths  $d_1$ ,  $d_2$ , and  $d_3$ . For Phantom 1, all photons in thickness  $T_1$  are also in depth  $d_1$ . Phantom 2 is of thickness  $T_2 = T_1 + d_2$ , where,  $d_1 = d_2 = d_3$ . The reflectance through thickness  $d_2$ ,  $R_{d2}$ , is thus the reflectance from  $T_1$  subtracted from the reflectance through the entire thickness,  $T_2$  as in Equation 5.3:

$$R_{d2} = R_{T2} - R_{T1} \quad \text{Equation 5.3}$$

This process of isolating photons traveling to different depths can be performed iteratively as in Equations 5.4 and 5.5:

$$R_{d3} = R_{T3} - R \quad \text{Equation 5.4}$$

And,

$$R = R_{Ti} - R_{T(i-1)} \quad \text{Equation 5.5}$$

The diffuse reflectance at each depth,  $d_i$ , for each pixel is then normalized to the maximum diffuse reflectance for that pixel. For a depth,  $i$ , and pixel,  $j$ , the normalized diffuse reflectance is given by Equation 5.6:

$$R_{i,j_{norm}} = \frac{R_{i,j}}{R_{j_{max}}} \quad \text{Equation 5.6}$$

Figure 31 depicts reflectance versus depths curves for a subset of pixels for the 2-layer phantoms from Theoretical Space 1. Only six pixels are shown on the graph for clarity; however, these curves have also been generated for all 24 simulated pixels, and

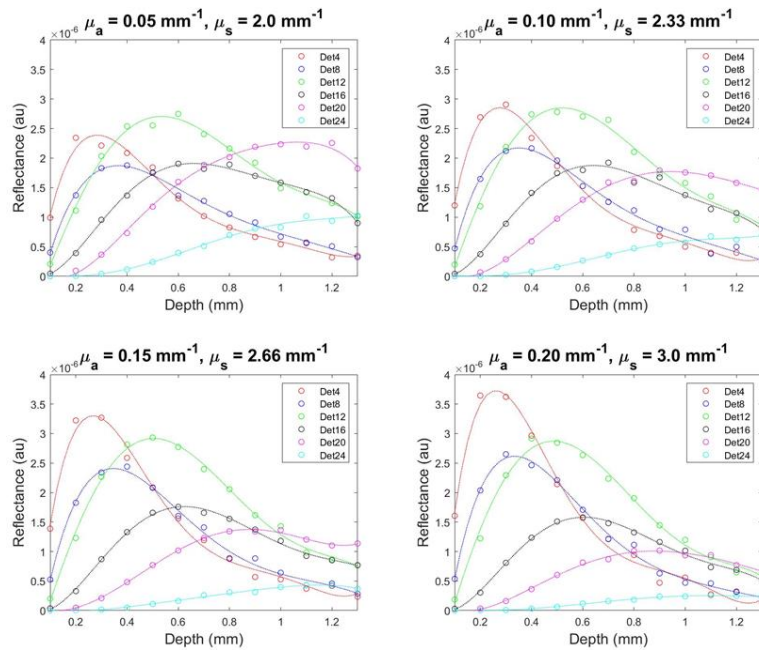


**Figure 31: Simulated Reflectance vs Depth for 6 Detectors in the Multipixel Si PD Sensor Array**

exhibit the same trends as the six pixel graphs. Note that increasing pixel number (e.g. Det4, Det12, Det20) is associated with increasing source/detector spacing. In Figure 31 we can see that an increasing source/detector spacing results in an increasing depth of maximum reflectance, indicating that the photons incident upon that PD have traveled deeper into the sample under test. Also notable is a flattening of the curve with increasing source/detector spacing. In theory, PDs detecting photons that reach greater depths will tend, statistically, to be re-emitted from the surface at further source/detector spacings. The outer detectors thus are also interrogating a larger optical path lengths, i.e., a greater thickness of sample/tissue. This results in the flattening of the curves because these detectors have a greater number of depths from which photons can arrive, and are larger in size, so collect a broader range of photons emitted from the surface.

Figure 32 shows the normalized diffuse reflectance, which enables a clearer visual comparison of the shape of the diffuse reflectance curve as a function of depth. The peak of the curve for each detector moves to the right (greater depth), with increasing source/detector spacing, indicating that as the detector number increases (e.g. Det4, Det12, Det20), the depth of interrogation of the photons in the sample also increases. This is shown visually in the progression of graphs in Figure 32. On the top left (Figure 32a), we see two detectors from the inner 50 um wide pixels. Figure 32b shows two detectors from the middle 100 um wide pixels are added to the graph. The depth of maximum reflectance from these two additional pixels is larger than the depth

of maximum reflectance from the inner pixels, as observed by a shift of the peak of the curve to the right (increasing depth). In Figure 32c, two detectors from the outer grouping of pixels (250  $\mu\text{m}$  width) have been added to Figure 32b. These two detectors show a further increase in depth of maximum reflectance. The final graph on the bottom right plots all 24 pixels. This graph demonstrates that each pixel has a distinct depth vs reflectance curve.

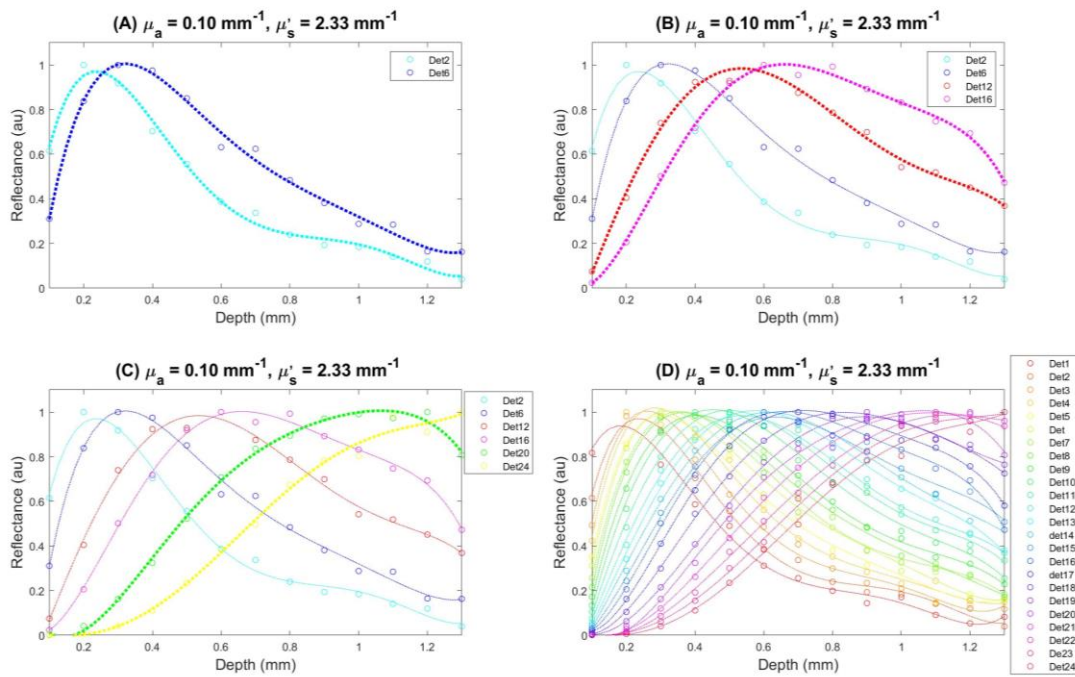


**Figure 32: Normalized Reflectance as a Function of Depth for one Set of Optical Properties**

These results may allow medical professionals to know the maximum tissue depth that the photons are interrogating and enable data to be accessed for individual tissue layers. For example, from Figure 32, the depth of maximum diffuse reflectance from detector four is around 0.35 mm. The inner pixels give less information about

deeper layers of the sample/tissue being interrogated, and the outer pixels offer information about deeper layers of sample/tissue. As discussed in Section 5.3, by observing the phantom thickness at which the DRS signal stops changing, researchers can assess the tissue thickness being interrogated by the device.

## ***5.6 System Resolution as a Function of Optical Properties***

As previously discussed, the optical properties of the sample/tissue can greatly affect the DRS signal. An increase in absorption, for example, generally results in a lower signal at the detectors. Figure 33 shows reflectance versus depth curves for four detectors and four different optical property pairs. These pairs are the four pairs within Theoretical Space 1 and are representative of the range of optical coefficients reported for skin tissue [43]. From Figure 33, it can be observed that even for optical properties within a given type of tissue (e.g. skin), a change in optical properties results in a change in the DRS curves. This is most evident at larger depths and larger source/detector spacing (i.e. higher detector number).

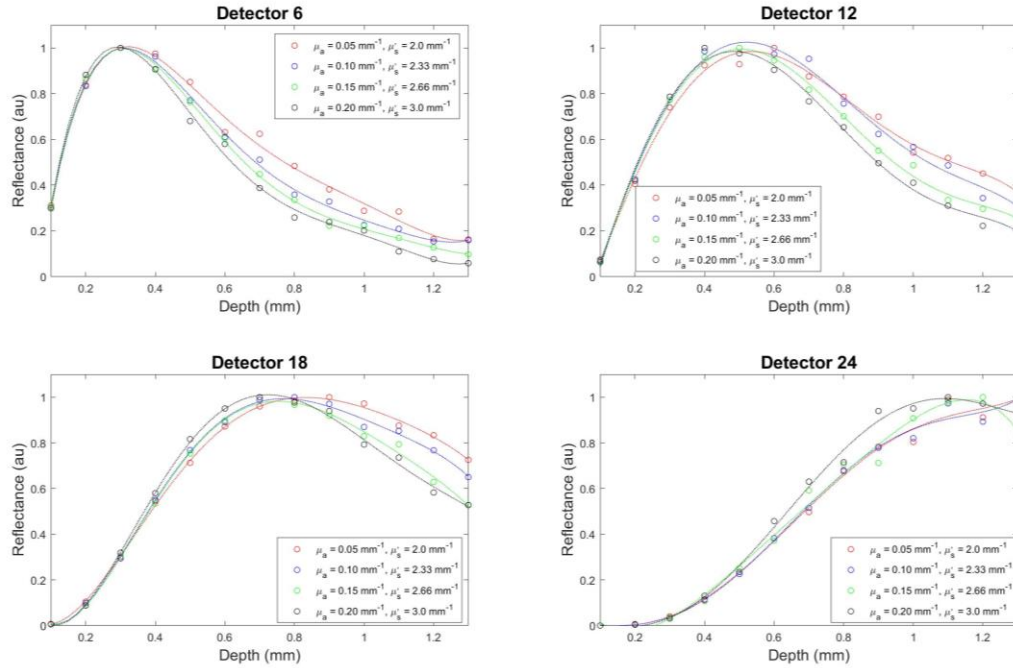


**Figure 33: Reflectance vs Depth for Different Optical Properties at Select Detectors**

By noting small changes for a particular detector compared to surrounding pixels, it may be possible to potentially isolate thin layers of tissue. If only a few detectors are exhibiting a change in DRS signal as a function of depth, a range of depths over which there may be an anomaly in the sample/tissue might be isolated. This concept will be further explored in Chapter 6 when measurements of multilayer phantoms are discussed.

Theoretical Space 2 was used to look at the effect of small changes in only absorption or scattering on the DRS signal. Theoretical Space 2 is in the range for skin tissue, in the same manner as Theoretical Space 1. A subset of theoretical DRS results are shown in Figure 34 (high  $\mu_s$ , changing  $\mu_a$ ). Figure 34 illustrates how small changes in the

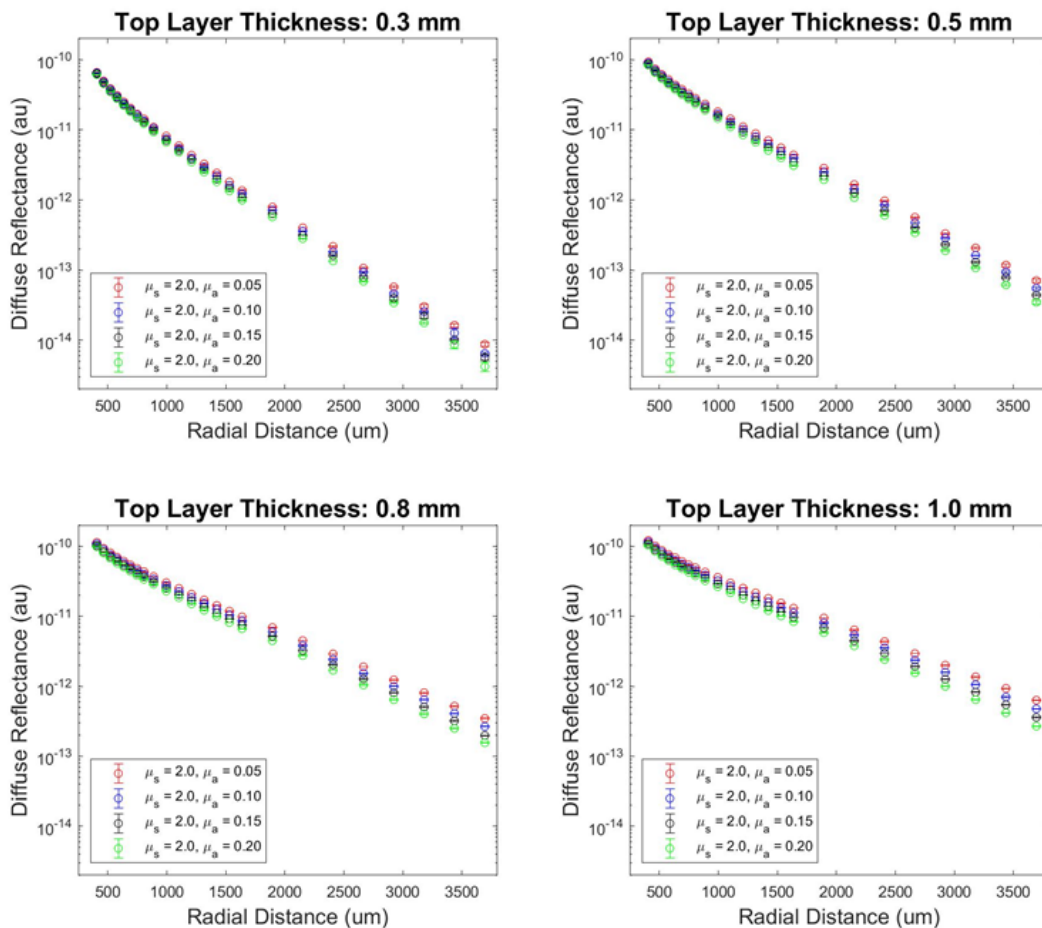


**Figure 34: Effect of Changing Absorption Levels on Simulated DRS Signal for 4 Phantom Thicknesses**

absorption coefficient for a constant scattering coefficient affects the DRS signal. The largest changes are in the outer detectors, as fewer diffusely reflected photons are emitted from the surface with increasing distance from the optical source. When focusing on further source/detector spacings we can see that a smaller value for  $\mu_a$  results in a higher DRS signal as previously discussed. Small changes in absorption on the order of magnitude of  $0.05 \text{ mm}^{-1}$  are not distinguishable visually on the graph except at larger phantom thicknesses. For larger phantom thicknesses, the overall magnitude of

the DRS signal increases because photons are less likely to interact with the highly absorbing bulk phantom, as previously discussed, increasing the signal at the detectors. The increased signal is accompanied by an increased ability to distinguish small changes in absorption values.

When these results are taken in combination, they have an impact on the ability of the DRS sensor array to distinguish a buried layer within otherwise homogenous samples/tissues. These results indicate that the sensor array will be more sensitive when the difference in absorption coefficients between the buried layer and the surrounding tissue is high. It also suggests that the thickness of the top layer can play a role in buried layer detection. Both of these observations will be investigated further in Chapter 6.

## **5.7 Conclusions**

This chapter presented experimental results for the measurement of two-layer solid phantoms. The stacked phantoms were composed of a thin phantom layer on top of a highly absorbing bulk phantom. Different thin top phantom layers with different optical coefficients were measured. The experimental results were used to develop a model in Zemax© that was validated on the measurements, and the model was then used to interpolate from the measured data a series of theoretical multilayer phantoms. Observations regarding the change in DRS signal as a function of phantom thickness were made using both the experimental and theoretical results. The theoretical multilayer phantom data was to create depth verses reflectance curves for each pixel in

the photodiode sensor array. Next, a discussion of the effects of tissue optical properties on the depth verses reflectance curves was presented.

This chapter is the first steps towards depth resolved measurements of tissue using the multipixel Si PD sensor array presented in Chapter 3. As discussed in Chapter 3, one of the main benefits of an array containing a high number of pixels is the ability to look at individual tissue layers. To accomplish this goal, it is important to first understand the relationship between the individual pixels, the DRS signal, and the depth of the layer of tissue being interrogated. This chapter explored this relationship and showed that highly accurate models can be developed using ray tracing software (Zemax©), and can be validated with experimental measurements. The next chapter will address how the Si PD array can be used when the sample/tissue under test is inhomogeneous.

## 6. Experiment and Simulation for Three Layer Phantoms

This chapter explores the sensing capabilities of the multipixel Si PD array when measuring multilayer solid phantoms containing a distinct layer between two phantoms of the same properties. The experimental measurement results on these 3 layer phantoms is presented, a theoretical model validated by the measurements is developed, and then a series of simulations interpolating the experimental results are presented. An analysis of the ability of the sensor to distinguish between multilayered and single layered (homogenous) phantoms will be performed with respect to the buried layer and top layer thicknesses. Finally, conclusions regarding the limitations of the current multipixel Si PD device will be discussed.

### 6.1 Motivation

As discussed at the beginning of Chapter 5, common assumptions regarding DRS measurements in homogeneous media are no longer valid when DRS systems are used for *in vivo* tissue sensing. Both healthy and diseased tissues consist of layers with differing optical properties [43]. For healthy tissue, within a given tissue type, sub-layers of tissue (i.e. epidermis verses dermis) may exhibit relatively similar properties compared to tissue of different types (i.e. muscle verses skin) [43]. Of particular interest to medical professionals is diseased tissue encapsulated or buried within healthy tissues. When determining the margins while excising internal cancer, detecting cancerous cells beneath healthy skin tissue, or evaluating the growth of a tumor within the colon, there

is a target diseased tissue surrounded by tissues that are normal. A device capable of non-invasively sensing and measuring the diseased tissue may be useful to guide further exploration of the buried suspect tissue. The identification of a distinctive buried layer of tissue within a surrounding tissue mass of comparatively similar optical properties is a step towards the realization of this medical goal.

This chapter is the culmination of the previous work described in this thesis. Chapter 3 described the design and fabrication processes for a Si PD SRDRS sensor with the potential for depth resolved measurements. Chapter 4 investigated optical coefficient extraction approaches for homogenous liquid phantoms. Evaluating the optical properties of a homogenous sample/tissue yields information regarding the overall tissue being interrogated and, as discussed in this chapter, aids in determining whether or not there is a layer of tissue with properties that are not the same as the surrounding tissue. Chapter 5 discussed the depth sensitivity of the SRDRS sensing system. For a given set of optical properties, we can determine the DRS signal as function of depth for each pixel in the system. This information is combined in this chapter with the information from Chapter 5 to explore a Receiver Operator Characteristic (ROC) curve analysis to assess the sample/tissue sample being interrogated. This information is aimed to better enable medical professionals to make yes-or-no decisions regarding further investigation of tissue samples, namely, by providing more information than when under the assumption that the tissue is homogenous.

## 6.2 Experimental Results

The diffuse reflectance of multilayered (3 layer) solid phantoms was measured using a multipixel Si PD sensor similar to the one previously described herein, but with a 400  $\mu\text{m}$  Si PD aperture [17]. At the time of the measurements, there were more functional pixels on a 400  $\mu\text{m}$  device than on the 750  $\mu\text{m}$  sensor array. This motivated the use of the 400  $\mu\text{m}$  sensor array for the measurements. Three layers of solid phantoms were stacked to create an inhomogeneous medium, as illustrated in Figure 35, for illumination with 660 nm wavelength light using a 300 W Xenon Lamp connected to a monochromator as described in previous chapters. The 3 layer phantoms were fabricated and the optical properties were measured by Dr. Greening, as described in Chapter 5.

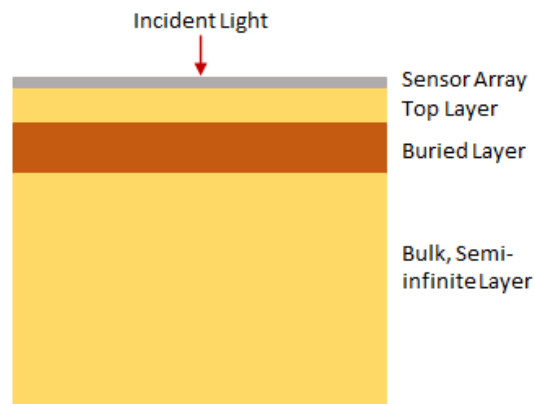


**Figure 35: Experimental Setup for 3-layer Solid Phantoms Measured Using a 400  $\mu\text{m}$  Aperture Si PD Sensor Array**

A two-layer phantom stack was created by placing a top layer on a more absorbing layer. The two-layer stack was then placed on top of a semi-infinite 15 mm

thick phantom whose properties were the same as those of the top layer. This stack was then measured using a multipixel Si PD probe with a 400  $\mu\text{m}$  aperture fabricated by Dr. Ozlem Senlik. Measurements were performed in collaboration with Dr. Senlik. In the PD array, 21 out of 24 pixels were functional at the time of measurement. For the purpose of this chapter, the semi-infinite phantom will be referred to as the bulk phantom. The middle layer whose properties differ from the surrounding layers will be called the buried layer. The thin phantom on the top of the stack will be referred to as the top layer phantom. The as-fabricated optical properties of the thin PDMS top layer phantoms and the 15 mm bulk phantom measured at 660 nm were:  $\mu_a = 0.05 \text{ mm}^{-1}$  and  $\mu_s' = 2.0 \text{ mm}^{-1}$ . The optical properties of the buried layer phantoms measured at 660 nm were:  $\mu_a = 0.2 \text{ mm}^{-1}$  and  $\mu_s' = 3.0 \text{ mm}^{-1}$ . Further details of phantom preparation can be found in [47]. A total of 15 different 3 layer phantoms were measured by combining a series of top layers of different thickness with a series of buried layers of different thicknesses. The five top layers ranged in thickness from 101  $\mu\text{m}$  to 934  $\mu\text{m}$ . The three buried layers ranged in thickness from 150  $\mu\text{m}$  to 476  $\mu\text{m}$ . For all 3 layer phantoms, the same 15 mm bulk phantom was used.

The experimental results for the 3 layer solid phantom measurements are shown in Figures 36 with the measurements from a homogenous, optically semi-infinite phantom. The left column of Figure 36 shows the measured raw data photocurrent, and the right column displays the reflectance signal (photocurrent per unit area of the

pixels). The purpose of this chapter is to determine the sensor's capability to distinguish between a homogenous tissue sample and a sample containing a buried layer whose optical properties differ from the surrounding tissue. Figures 36 shows that these experiments demonstrate that the DRS signal varies with buried layer and top layer thickness.

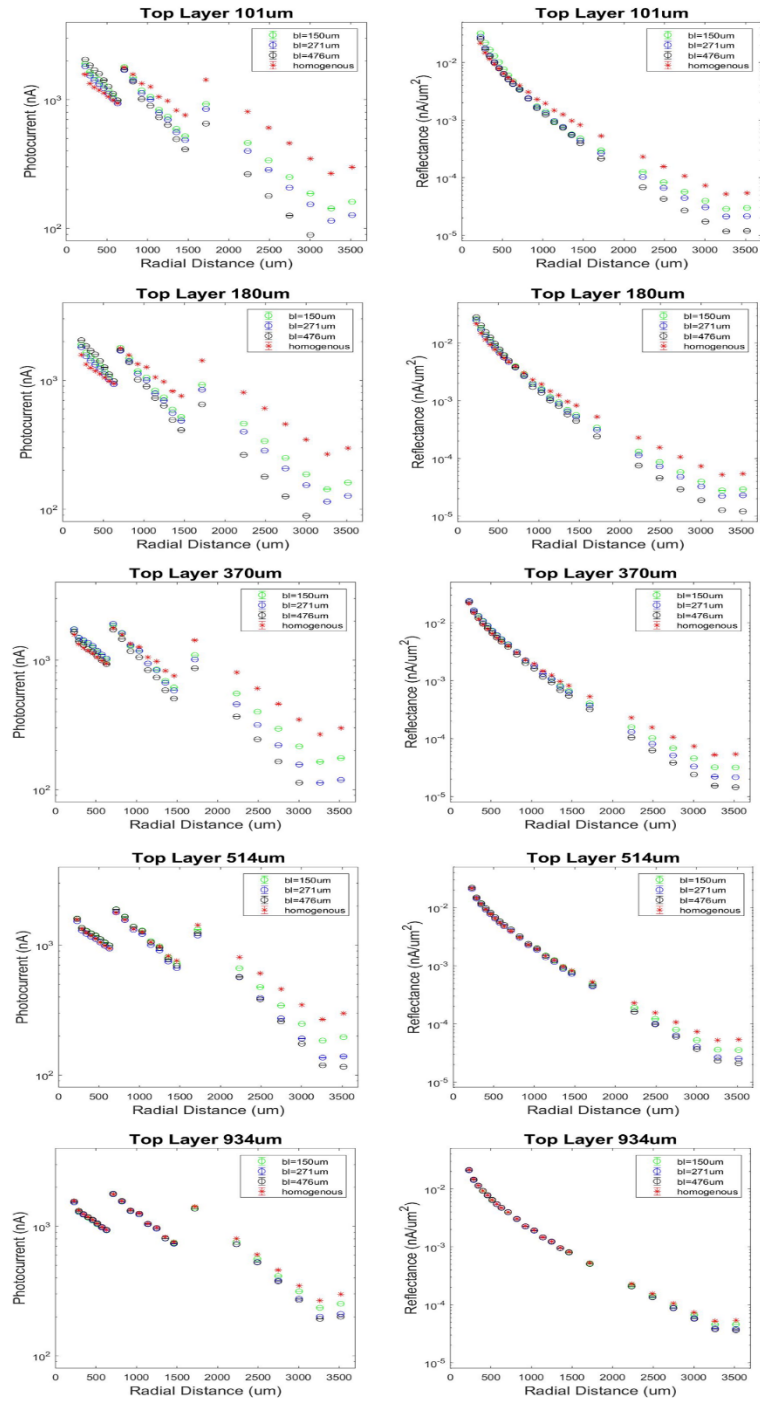


Figure 36: 3 Layer Solid Phantom Measurements using 400 um Si PD Sensor Array

The experimental results show that the DRS signal decreases with the presence of a buried layer compared to the DRS signal from a homogenous phantom, as is expected, when a more highly absorbing and more highly scattering layer is inserted into a lower absorption and lower scattering phantom. The signal decrease is most evident at the outer detectors and for thinner top layers. As the top layer thickness increases, the top layer of the multilayer phantom is approaching a semi-infinite optical extent. Chapter 5 showed that as a thin phantom layer approaches an optical semi-infinite thickness, the difference in DRS signal as a function of increasing phantom thickness decreases. This leads to the 3 layer phantoms with a thicker top layer being less distinct from each other and from the homogenous phantom, even when a buried layer is present.

The experimental results also indicate that the buried layer thickness affects the DRS signal. We can see that thinner buried layers have less effect on the DRS signal for a given top layer thickness compared to the thicker buried layers. In other words, thinner buried layers result in DRS signals closer to that of the DRS signal from a homogenous phantom. As the thickness of the buried layer decreases, the photons are interrogating more of the homogenous tissue compared to buried layers of greater thicknesses. Since the buried layer has a higher absorption than the surrounding layers, a photon propagating through a thicker buried layer is more likely to be absorbed, decreasing the DRS signal for increasing buried layer thickness.

### **6.3 Simulation of Phantoms Containing a Buried Layer**

Zemax© was used to simulate the experimental results from Section 6.2. The Si PD array physical characteristics were input to the simulation, as were the incident optical signal and the phantom properties and thicknesses. The Henyey-Greenstien phase function was used for the probability distribution of scattering angle and the anisotropy factor was 0.8, which was the anisotropy factor used previously for solid phantom experiments [12]. Three simulations of five million photons each were generated, and the output of these simulations was the optical power at each detector. The average optical power of these simulations was converted to photocurrent so as to compare the simulations to the measured PD array photocurrents, using the same scaling factor approach as described in Chapter 5. Figure 37 shows the simulated results compared to the experimental results (shown in Figure 36). The agreement is very good, with an average percent error between the measured results and the Zemax© simulation across all pixels and phantoms was 5.3%.

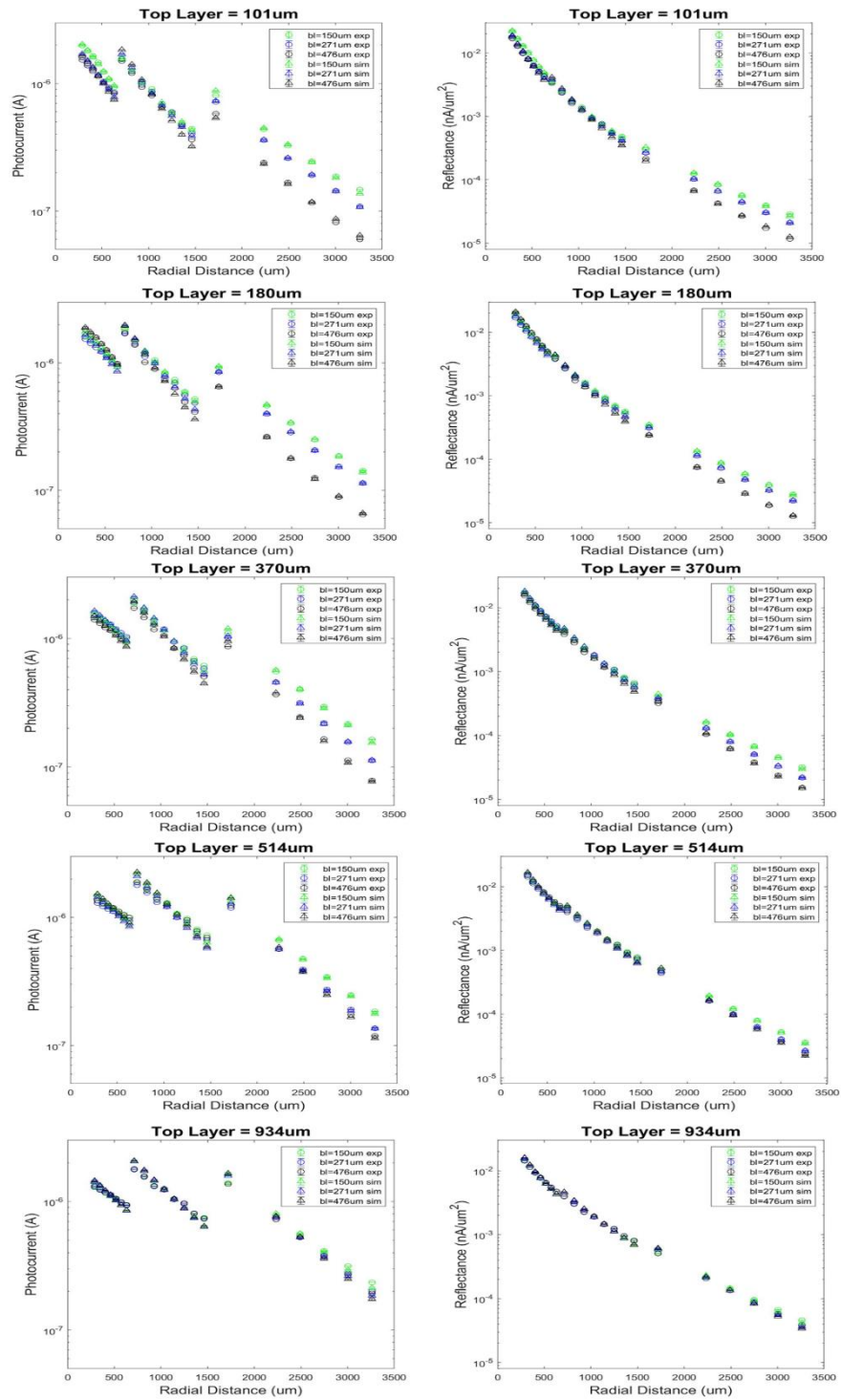


Figure 37: Theory vs Experiment for 3-Layer Solid Phantoms Measured using a 400 um Si PD Sensor Array

It would be useful to relate the models for these 750  $\mu\text{m}$  and 400  $\mu\text{m}$  structures, so as to inform the results of the 3-layer phantoms by the 2-layer phantoms. The simulations of the 2-layer phantoms were validated by the experiments in Chapter 5 using a 750  $\mu\text{m}$  aperture PD, and likewise, the simulations of the 3-layer phantoms using the 400  $\mu\text{m}$  aperture PD were validated by experiment in Section 6.2. Both of these MC simulations were performed using the same model, changing only the aperture size, pixel radii (but using the same pixel width), and the phantoms. To relate the models for the 2-layer and 3-layer structures, the validated model for the 400  $\mu\text{m}$  structure was modified to include a 750  $\mu\text{m}$  aperture and the PDs were modified to radii corresponding to the 750  $\mu\text{m}$  PD array. This model was then used to simulate an expanded data set for the 3-layer phantoms.

This model was used to interpolate between the measured data (using the same optical properties used in the 400  $\mu\text{m}$  3-layer experiments, as in Section 6.2) to simulate a series of 25 phantoms consisting of 3 layers each using the geometry of the 750  $\mu\text{m}$  aperture array. The top layer thicknesses in the interpolated model ranged from 100  $\mu\text{m}$  to 900  $\mu\text{m}$  in 100  $\mu\text{m}$  steps. Buried layer thicknesses also ranged from 100  $\mu\text{m}$  to 900  $\mu\text{m}$  in 100  $\mu\text{m}$  steps. A 15 mm optically semi-infinite phantom was used as the bulk layer. The simulation results from these theoretical phantoms are shown in Figure 38. Unless otherwise stated the analysis in the rest of the chapter uses these simulated phantoms.

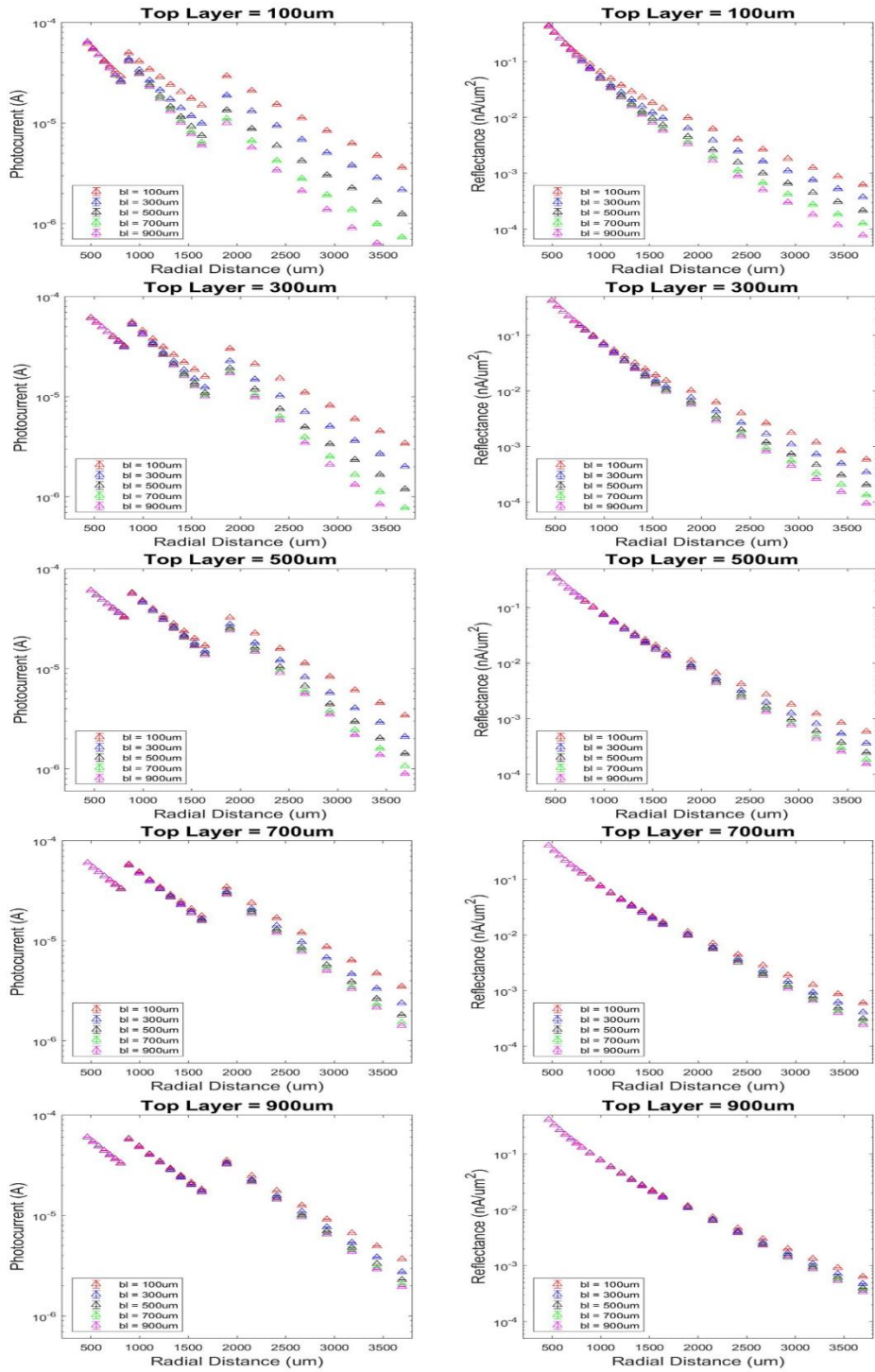


Figure 38: Simulated 3-Layer Phantoms using a 750 um Aperture Si PD Sensor Array

## 6.4 ROC Curves in Decision Making

For some applications, the analysis of DRS signals does not have to quantify every aspect of the tissue being interrogated. Rather, as mentioned in Section 6.1, there are situations in which medical professionals are seeking to answer yes-or-no questions. For example, is there a layer of cancerous tissue that lies beneath normal tissue? Because typical human skin and other tissue is complex and multilayered, this is a very difficult question. However, the field needs to take steps to begin to address the detection of buried layers of tissue that have different optical coefficients from the surrounding tissue. Herein, to make progress toward the detection of a buried phantom layer surrounded by homogeneous phantom layers, a yes-or-no analysis of whether or not a buried layer is present is explored.

Receiver operating characteristic curves (ROC curves) can be used to evaluate the decision-making capabilities of a system, particularly when a yes-or-no answer is desired. ROC curves evaluate the false positive rate (1 - specificity) versus the true positive rate (Sensitivity) [48]. Where specificity and sensitivity are given by Equations 6.1 and 6.2:

$$Specificity = \frac{N_{True\ Negatives}}{N_{True\ Negatives} + N_{False\ Positives}} \quad \text{Equation 6.1}$$

And,

$$Sensitivity = \frac{N_{True\ Positives}}{N_{True\ Positives} + N_{False\ Negatives}} \quad \text{Equation 6.2}$$

ROC curves can be used to compare different models, and will be used later in this chapter. The area under the curve,  $A_{ROC}$ , is a general marker for the performance of the model [48]. As  $A_{ROC}$  approaches 1, the model approaches a perfect model. As  $A_{ROC}$  moves from 1 towards 0.5, the ability of the model to distinguish between the two cases decreases. If  $A_{ROC}$  moves below 0.5, the model has switched the prediction cases. For diagnostic testing, an  $A_{ROC}$  of 0.8-0.9 is labeled as ‘excellent’ while an  $A_{ROC}$  of 0.9 or above is considered outstanding [49]. This chapter will present results that fall in these ranges.

When considering medical cases, classification models seek to decrease the number of false positives and false negatives. A false negative can be more harmful than a false positive since a false negative could result in a patient foregoing necessary treatment. For example, if a buried layer of cancer is not detected under healthy skin tissue it would not be excised and could grow and eventually metastasize to other areas of the body. In contrast, if a buried layer is falsely detected (there is no real buried layer) then the patient might undergo unnecessary procedures. A medical classification system thus needs to maintain a high sensitivity while reducing the number of false positives.

It is very important to note that the performance of decision-making algorithms (and thus the ROC curve) are greatly influenced by the choice of algorithm. There are a number of processing algorithms that can be chosen, ranging from linear prediction

algorithms to support vector machines. For the work herein, a support vector machine was chosen for the classification of 3-layered phantoms. The algorithm used was the `fitcsvm()` algorithm available in MATLAB. No changes were made to this algorithm. ROC curves are showing the change in sensitivity and (1-specificity) for a given threshold value between two hypothesis  $H_0$  and  $H_1$ . Herein,  $H_0$  is represented by the presence of a homogenous phantom. There is only one case where a homogenous phantom is present for the simulations.  $H_1$  is when a 3-layered phantom is present. The 25 simulated 3-layer phantoms all fall under the  $H_1$  hypothesis. The following ROC curves are testing the ability of the processing algorithm to predict the presence of a 3-layer phantom.

## ***6.5 ROC Analysis of the DRS Sensing System***

The following section analyses ROC curves for the simulations described above in four situations: overall (both from simulations and experiment), as a function of detector group, as a function of top layer thickness, and as a function of buried layer thickness.

Figure 39 shows the ROC curves for the system as a function of which detector groups are involved in the analysis. When visually inspecting the measured and simulated data from the previous sections, we can see that there is greater contrast between the DRS signals with

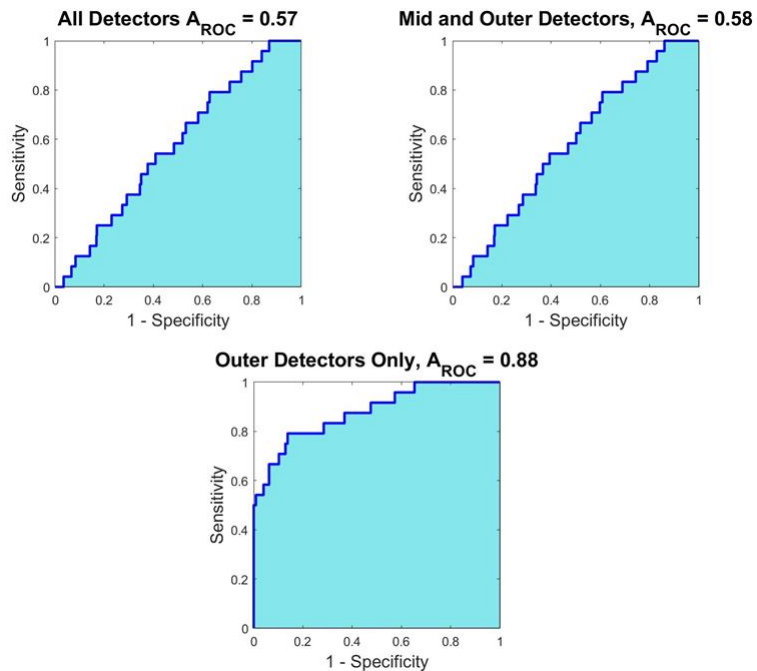


**Figure 39: ROC Curves for Simulated 3-layer Phantoms as a Function of Detector Group**

increasing source-detector spacing for 3-layer phantom structures with a highly absorbing buried layer. The outer detectors show a greater difference between measurements for all 25 phantoms. This is reflected in the performance of the models in Figure 39. When all of the detectors are used, the system exhibits worse classification capabilities ( $A_{ROC} = 0.57$  for all detectors and  $A_{ROC} = 0.58$  for the middle and outer detectors combined). The area under the ROC curve is close to 0.5, signifying that the model cannot distinguish between the two states. When the inner detectors are no longer used in the model, the performance improves but is still less than ideal. When only the outer 8 PDs are used, the model performs significantly better ( $A_{ROC} = 0.88$ , excellent). Figure 40 is the same model using the 15 experimental 3 layer phantoms

rather than the 25 simulated 3-layer phantoms. The performance of the experimental system is similar to that of the simulated system, and thus, the experimental data in this situation can be used in a classification model of the system. Based on these results, further analyses using only the outer detectors was conducted.

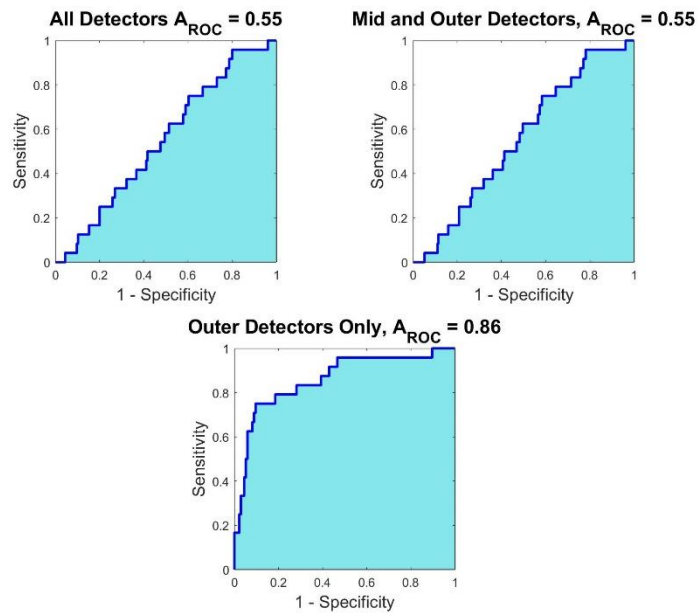


**Figure 40: ROC Curves for Experimentally Measured Data as a Function of Detector Group**

The results in Sections 6.2 and 6.3 show that as the top layer thickness increases, the difference between the layered phantoms and the homogenous phantoms decreases. When the top layer thickness is 900  $\mu\text{m}$ , there is little difference between the data except at the extreme outer detectors, since the top layer is nearly optically infinite in extent. When the top layer thickness is reduced to 100  $\mu\text{m}$ , there is a clear difference in the middle and outer sets of detectors. This is reflected in Figure 41, and thus, the classification model performs better for thinner top layers (outstanding instead of

excellent). The results presented in Figure 41 use only the outer 8 detectors in the decision-making algorithm.

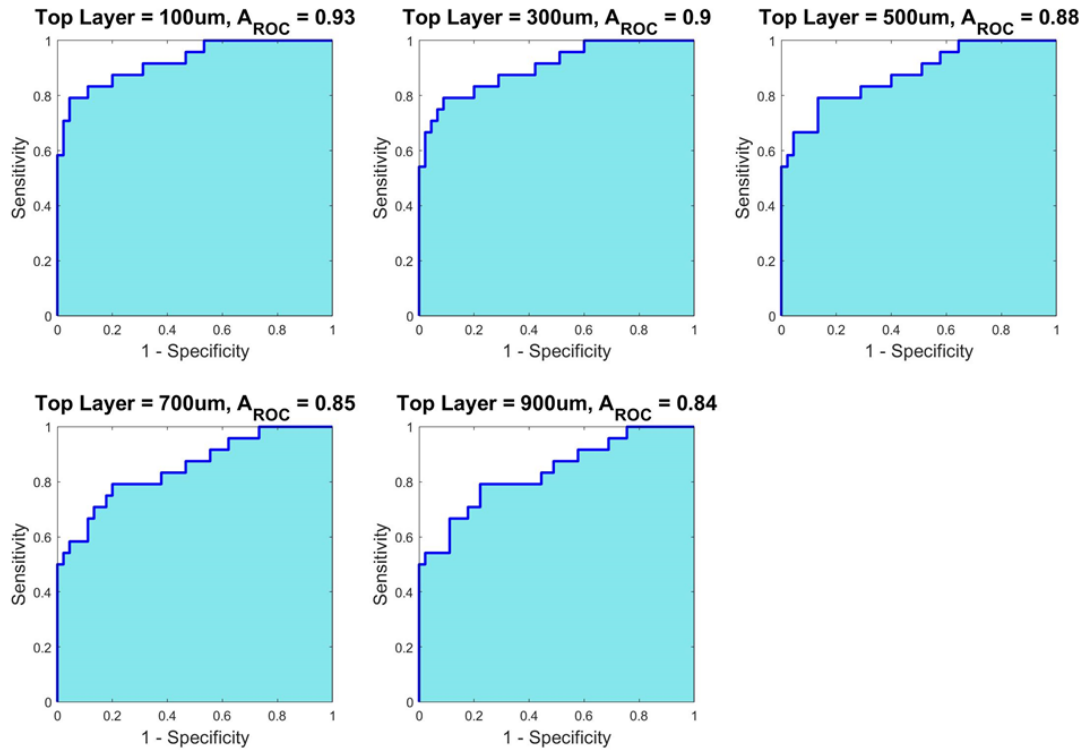


**Figure 41: ROC Curves as a Function of Top Layer Thickness for Simulated Phantoms**

When the classification analysis is performed as a function of buried layer thickness, the model performs better for thicker buried layers. The buried layer has higher absorption than the surrounding phantoms, and, as the buried layer thickness increases, the photons are more likely to be absorbed within this layer instead of propagating back to the sensor array at the surface of the tissue. The difference between the multilayer phantoms and the homogenous phantoms is thus greater. These results

are shown in Figure 42, where only the outer 8 detectors are used as a part of the analysis.

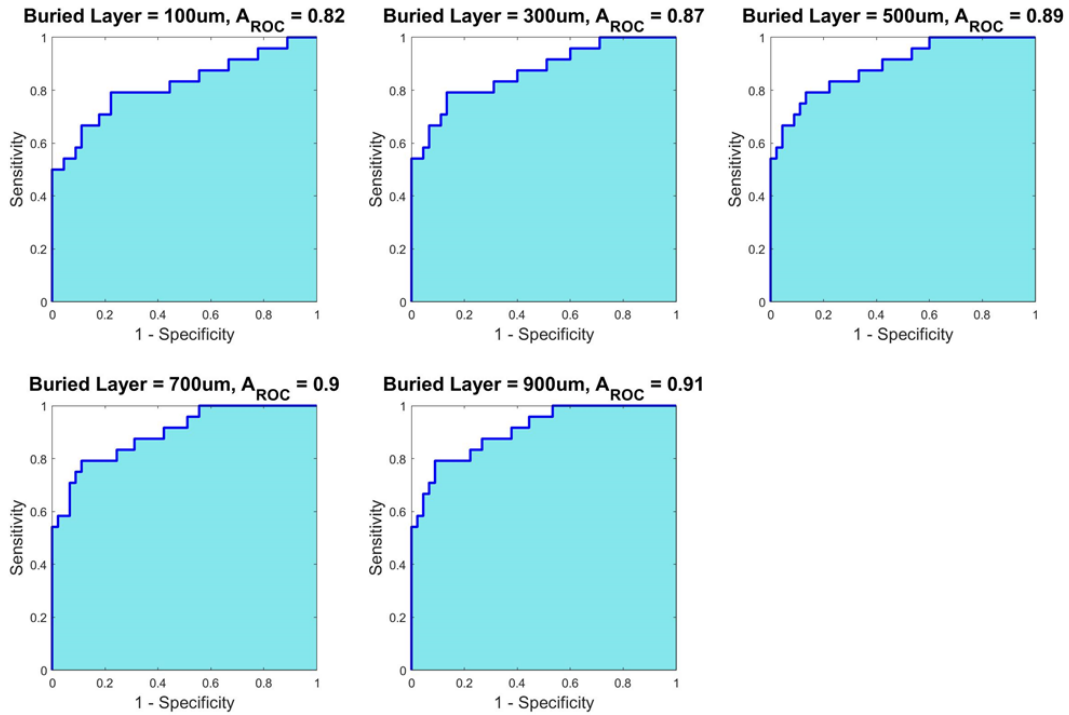


**Figure 42: ROC Curves as a Function of Buried Layer Thickness for Simulated Phantoms**

Finally, a series of 25 multilayer (3 layer) phantoms was simulated where the optical properties of the top layer and bulk layer were the same as the previously simulated phantoms. The buried layer was altered to increase the absorption and scattering coefficients compared to the previous examples:  $\mu_a = 5.0 \text{ mm}^{-1}$  and  $\mu_s' = 3.0 \text{ mm}^{-1}$ . The high absorption coefficient of the buried layer is consistent with melanoma [43]. These phantoms were then used in the classification model. The results are shown in Figure 43. When the buried layer is more highly absorbing, the model performs

better, even when all detector sets are used, and the outer PDs still outperform the entire PD array.

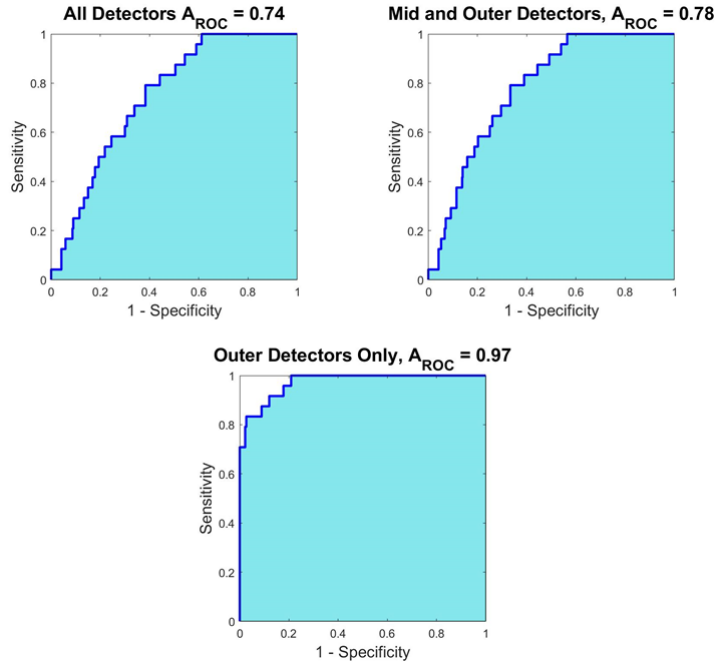


**Figure 43: ROC Curves for a Highly Absorbing Buried Layer as a Function of Detector Group**

## **6.6 Classification of 3-Layer Structures**

This section will discuss how the multipixel Si PD array can be used for the classification of 3-layer samples using different sensors in the array to target different layers of tissue. For example, previous DRS studies using multiple source/detector spacings have used a single emitter and different detectors in a detector array to measure samples at different depths. This published research partitioned the detectors into two groups: one to measure the overall optical properties of a sample and one to target depth measurements [37], [42], [50]. These studies took advantage of general

knowledge of photon propagation through tissue (e.g. photons exiting at further source/detector spacings had propagated deeper into the tissue). These studies used a few inner detectors to measure the upper layer of the sample, and outer detectors to perform measurements of deeper layers. Herein, a similar technique will be used, but will take advantage of the densely packed Si PD array to perform the measurement of the upper layer using eight pixels (in contrast to only a few in the published paper [39], [40], [42]). The process presented herein quantifies the optical coefficients of the upper layer, but not those of the buried tissue.

Based on the results presented in Section 6.5, a sample with a possible buried layer could be evaluated using the following by partitioning the detectors into two groupings: the inner 8 pixels and the outer 16. First, the inner eight pixels would be used to extract the upper sample optical properties. It was shown that the inner eight pixels do not measure significantly different properties when there is a buried layer present. This is true for all simulated top layer thicknesses and buried layer thicknesses herein. Chapter 4 examined the sensor optical property extraction error as a function of detector set. For homogenous liquid phantoms, the error was independent of which grouping of detectors was used for optical property extraction. There was a decrease in extraction accuracy with the use of fewer detectors, but the extraction accuracy remained at 9.03% for  $\mu_a$  and 3.62% for  $\mu_s'$  for nine detectors when using PLSR as the extraction mechanism. Assuming that this also holds true for solid phantoms, the inner detectors

can thus be isolated and used to extract the optical properties for the homogenous tissue above the potential buried layer. The properties extracted from the inner 8 pixels are used to create a MC model of a homogeneous phantom.

The photocurrents from the outer 16 pixels would be compared to the photocurrents that would result from the theoretical homogeneous phantom created from the inner 8 pixel data. If the outer 16 pixel data is consistent with the homogeneous phantom model, then no buried layer is present. If the outer 16 pixel data is not predicted by the homogenous phantom model, then a buried layer may be present. The ROC model is a good way to visualize this comparison and to classify the question of a buried layer in a yes-or-no manner. Note, however, that this analysis gives no information regarding the location of the buried layer or the optical properties of the buried layer.

## **6.7 Conclusions**

This chapter focuses on the measurement of 3-layer solid phantoms. The measured phantoms consisted of a buried layer sandwiched between two layers, where the two layers have the same optical properties. The buried layer had a higher absorption than the surrounding phantoms. The system was MC simulated using Zemax© to compare theory to experiment, and the average percent error between theory and experiment across all pixels and phantoms was 5.3%. The model developed in Zemax© was then used to interpolate between the measured results to simulate 25

phantoms that had 3 layers. The simulated phantoms were used to evaluate the capability of the sensor to distinguish between homogenous samples and samples containing a buried layer through the use of ROC curves. The results herein are the first evaluation of a DRS system using ROC curves to determine the sensitivity of a multipixel sensing system to the presence of buried layers within a sample.

Future work in this area could improve the algorithm used for processing the data. As previously mentioned, the processing algorithm can significantly affect the classification results. Classification is based on the raw data (as shown in this chapter) combined with the processing of that data. This chapter demonstrated that the outer detectors are better suited for the prediction of buried layers. However, other algorithms could be chosen to mitigate the effect of the inner detectors. That is outside of the scope of this work, but would be key to further results in this field.

## 7. Conclusions

This chapter presents conclusions and thoughts on future work for this thesis. Optical property extraction from homogenous liquid phantoms, depth analysis of solid phantoms and multilayer phantoms will be discussed. Finally, opportunities for future work will be presented.

### 7.1 Conclusions

Diffuse reflectance spectroscopy is a non-invasive, optical interrogation technique that has been used for the measurement of tissues/samples both *in-vivo* [40] and *ex-vivo* [7]. Previous work in the field includes the quantification of optical tissue properties from homogenous liquid phantoms [51], measurement of cancerous breast tissue [1], determination of the stages of colon cancer [24], and the quantification of chromophores [41]. While some techniques such as the measurement of phantoms can be highly controlled to contain only one homogenous layer of tissue, *in vivo* measurements often sample complex tissues containing multiple layers. Optical properties change with tissue type; therefore, the complexity of tissue needs to be accounted for during DRS measurements and in the analysis of DRS data.

This thesis presents research aimed at increasing optical property extraction accuracy for homogenous phantoms and to enable the detection and analysis of layered phantoms. Chapter 2 contains an overview of the field of DRS, focusing on optical property extraction approaches and how they are used to obtain information about

tissues/samples. Chapter 3 discussed the design, fabrication, and initial testing of a 32-pixel Si pn junction photodetector array. Chapter 4 used a similar, 24-pixel sensor array to measure homogenous liquid phantoms. Chapter 4 also focuses on the extraction of optical properties through modeling of the phantom measurements. Look-up tables (LUTs), a technique often used in DRS optical property extraction, were compared to partial least squares regression (PLSR). PLSR is a linear regression technique that is often applied to complex chemical spectra and has been previously applied to tissue analysis but has not been used for optical property extraction in conjunction with a multipixel sensor array. By combining the complex multipixel sensor with PLSR, this work demonstrated increased accuracy in the quantification of the optical scattering coefficient compared to an approach using look-up tables for the experiments performed. The photodetector array in combination with PLSR was also more robust to a low sensor SNR compared to the same sensor array combined with a look-up table. Thus, the array can be used with multiple extraction techniques with a high accuracy, indicating that the sensor array data is adaptable to multiple DRS applications that might have a preferred coefficient extraction approach.

After determining that optical property extraction using the multipixel probe was possible when combined with multiple extraction techniques, Chapters 5 and 6 focused on the potential of the array for depth resolved measurements. In Chapter 5, the 24-pixel sensor array was used to conduct depth resolved measurements in homogenous

solid phantoms of varying thicknesses. For each pixel in the array, the DRS signal as a function of sample depth was calculated. This enables users to roughly correlate probe pixels to measurement depth, so as to identify specific pixels to use when measuring specific layers of samples at a certain depth. Chapter 6 showed that the probe is capable of distinguishing between homogenous samples and samples with buried layers using multilayer solid phantoms. The work herein represents the first steps towards using a multipixel sensor array for the depth resolved measurement of samples. The next two sections will explore how the capabilities of the sensor array can be expanded and further investigated.

## ***7.2 Future Work: Depth Analysis with Arrays Composed of More Pixels***

This thesis focused on the testing of a 24 pixel Si PD sensor array. A 24 pixel array was chosen based on experimental constraints (cost and size of materials). However, a 32 pixel array was designed and characterized in Chapter 3. The 32 pixel array targeted sample layers at a depth of 2.5 mm based on its overall radius (approximately 7 mm). This is roughly twice the sensing depth of the 24 pixel array in skin mimicking samples as characterized in Chapter 5. Measurements targeting larger veins and arteries as well as muscle tissue need to sense much deeper than the 1.3 mm discussed in Chapter 5. The 32 pixel array as designed has the potential to perform this sensing. It has not yet been used to measure samples, however, meaning the signal levels at the outer detectors may be too small for accurate optical property prediction.

A comparison between the 32-pixel array discussed in Chapter 3 and the 24-pixel array used in the experiments in Chapters 4-6 would be useful in furthering knowledge about the depth sensitivity of the multipixel arrays. This would be accomplished through the measurement of similar homogenous liquid phantoms and multilayer phantom stacks combined with MC simulations. If a 32-pixel array did not significantly expand the interrogation depth or did not help classification accuracy between a multilayer and homogenous phantom then the extra pixels may not be worth the increase in materials used for experiments or the increased measurement time that comes with a 32-pixel device. The tradeoffs between measurement time, material use, and increased classification accuracy need to be evaluated for multipixel arrays. This analysis will also lend itself to an understanding of how the array can perform when measurements are targeting specific optical properties. DRS measurements with a multipixel probe for the quantification of cytochrome c oxidase will be discussed in the next section.

### ***7.3 Future Work: The Sensing of Cytochrome C Oxidase***

Current methods for monitoring patient health often include a measurement of the oxygen content within the blood stream. Concentrations of oxygen within the vascular system are not directly related to the amount of oxygen available in tissue, however, and thus are not a good measure of the health of critical organs such as the brain and kidneys [52]. Cytochrome C Oxidase (CCO) is the terminal enzyme in the

electron transport chain and thus linked to tissue health and the amount of oxygen available to the tissue [53]. Measurements of CCO would improve upon doctors' current ability to monitor patients under anesthesia and those who have an elevated risk of stroke or heart attack by giving medical professionals a direct way to monitor the condition of critical organs.

The 32 pixel sensor array presented in this thesis was designed for measurement in skin and muscle tissue. As the terminal enzyme in the electron transport chain, CCO is present in all cells with mitochondria and therefore sensing can be targeted in multiple areas of the body. Recently a great deal of research has been conducted on the measurement of cytochrome c oxidase within brain tissue [6], [41], [54]. However, the highly absorptive nature of the skull makes optical measurements difficult. DRS signal levels for the skull are much smaller than for the other areas of the body. Multiple groups have previously attempted to monitor CCO level ([8], [55]); however, they have encountered a number of drawbacks to accurate quantification of this chromophore. Signal changes due to a variety of causes including blood flow fluctuation, probe pressure changes and oxygen level changes can obstruct direct sensing of CCO [56]. The large level of background noise in these systems results in a low signal to noise ratio (SNR). When the noise of the system is large, small signal variations due to changes in CCO and other chromophore concentrations are harder to distinguish. Finally, there have been multiple attempts at designing an algorithm for accurate absolute CCO

quantification. These algorithms are often complex in nature and rely on different extraction methods. Combined with the fact that there is no gold standard for CCO measurement, direct comparisons of system performance are often not possible. The multipixel Si PD sensor array presented herein demonstrated high prediction accuracies in low SNR settings when paired with PLSR for sample property extraction. Additionally, it demonstrated the ability to perform depth resolved measurements. The densely packed array therefore has the potential to aid in the sensing of this key enzyme because it could overcome two of the main drawbacks of current systems: poor prediction in low SNR settings and poor depth resolution.

To examine the ability of the multipixel Si PD array to perform *in vivo* sensing in scenarios similar to those for CCO testing, two participants were used in the blood pressure cuff trials. They had different percentages of body fat. This was established based on a visual assessment of the volunteers. The CCO sensor must be able to extract data over a large range of body types for it to be useful in a clinical setting. Additionally, one of the participants was male and the other was female. Both were professors involved in this research who asked to be measured.

The trials proceeded as follows: (1) the blood pressure cuff was attached to the participant; (2) Teflon tape was adhered to the participant's lower forearm in the sensing location to protect the multipixel Si PD sensor from skin surface contaminants such as oils; (3) the multipixel Si PD sensor was lowered onto the forearm; (4) a measurement

under no cuff inflation was taken; (5) the cuff was inflated to 60 mmHg and remained there for 60 s for stabilization of blood flow; (6) a measurement under pressure was taken; (7) the cuff was deflated and remained there for 60 s for stabilization; (8) a measurement under no pressure was taken; (9) the cuff was inflated to 200 mmHg and was stabilized for 60 s before measurement; (10) a measurement was taken at pressure. The photocurrent was measured under illuminations between 400 nm - 900 nm in 50 nm steps. Pressures of 60 mmHg and 200 mmHg were chosen because they represent venous and arterial occlusion respectively. This enabled measurement of two different levels of oxygen flow.

Figures 44 and 45 show measurements on participant 1 at 600 nm. 11 measurements were averaged for each point plotted in the figures. Figure 44 is an assessment of the repeatability of the measurements before and after cuff inflation when

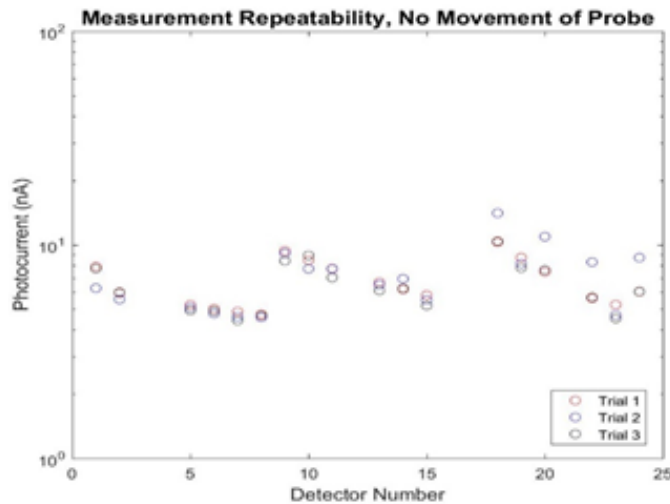


**Figure 44: Repeatability of Blood Pressure Cuff Measurements using Multipixel Si PD Sensor Array**

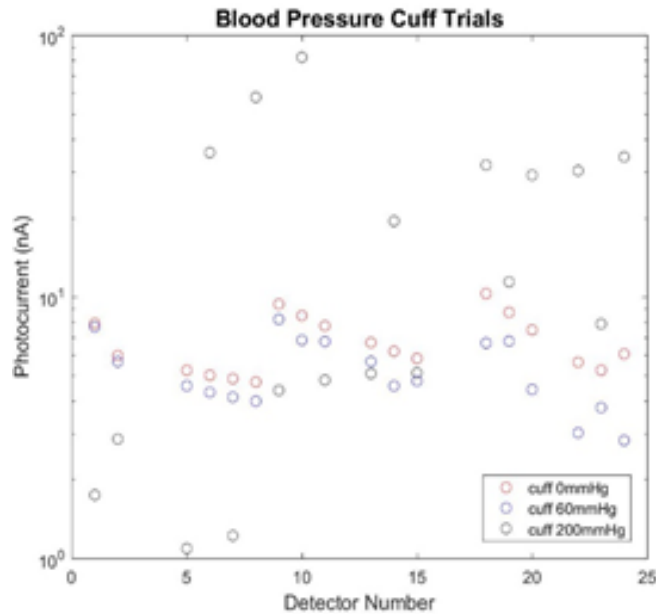


**Figure 45: Blood Pressure Cuff Measurements for No Inflation, Inflation to 60 mmHg and Inflation to 200 mmHg**

the sensor array is not moved. Trial 1 occurred before any inflation of the blood pressure cuff, while trials 2 and 3 occurred after the 60 mmHg and 200 mmHg inflation, respectively. Measurements spaced far enough apart for stabilization are expected to show close agreement to each other. The average percent difference between consecutive trials was below 15% averaged over all detectors, and 66% of the functional detectors had a maximum percent difference below 20%. As can be seen in Figure 45, comparing measurements under inflation and without inflation, the difference between trials under no pressure is similar to the difference between an uninflated pressure cuff and a pressure cuff inflated to 60 mmHg. If the stabilization time was not long enough between trials, then this could result in the large percent difference at some pixels. In

future trials, a longer stabilization time will be used to decrease the percent difference between un-inflated trials.

Figure 45 compares the measured photocurrent before cuff inflation, inflation to 60 mmHg, and inflation to 200 mmHg at 600 nm. This shows that inflation to 60 mmHg consistently resulted in a lower photocurrent for all detectors. Inflation to 200 mmHg did not result in a consistent trend, however. This was one relatively uncontrolled test, and the blood pressure cuff measurements presented herein are exploratory, however, they do demonstrate that a probe design such as the CCO sensor is capable of distinguishing different types of blood flow to the lower arm. Additionally, consistent measurements are possible for a similar pressure for one participant.

Further testing in collaboration with Dr. Richard Moon would seek to better understand the functionality of the multipixel Si PD sensor array during *in vivo* testing. Both a 24 pixel sensor and a 32 pixel sensor will be compared to determine the effect of additional pixels on *in vivo* property extraction. Using longer stabilization times, an increased number of participants, and a more repeatable setup, the repeatability of measurements would be remeasured and the DRS signals from each participant would be compared. Combined with phantom measurements containing varying levels of CCO mixed with other chromophores, these *in vivo* tests could lead to further information about the ability of the sensor array to measure CCO.

## References

- [1] C. Zhu, G. M. Palmer, T. M. Breslin, J. Harter, and N. Ramanujam, "Diagnosis of breast cancer using diffuse reflectance spectroscopy: Comparison of a Monte Carlo versus partial least squares analysis based feature extraction technique," *Lasers Surg. Med.*, vol. 38, no. 7, pp. 714–724, 2006.
- [2] N. Rajaram, R. Js, N. Th, and T. Jw, "Pilot clinical study for quantitative spectral diagnosis of non- melanoma skin cancer .," *Lasers Surg. Med.*, vol. 42, no. 10, pp. 716–727, 2010.
- [3] A. I. Mundo, G. J. Greening, M. J. Fahr, L. N. Hale, and T. J. Bullard, Elizabeth A Rajaram, Narasimhan Muldoon, "Specialized source-detector separations in near-infrared reflectance spectroscopy platform enable effective separation of diffusion and absorption for glucose sensing," *J. Biomed. Opt. Opt.*, vol. 10, no. 9, pp. 4839–4858, 2019.
- [4] A. I. Mundo *et al.*, "Diffuse reflectance spectroscopy to monitor murine colorectal tumor progression and therapeutic response," *J. Biomed. Opt.*, vol. 25, no. May, 2020.
- [5] S. P. Nighswander-Rempel, V. V Kupriyanov, and R. A. Shaw, "Assessment of optical path length in tissue using neodymium and water absorptions for application to near-infrared spectroscopy.," *J. Biomed. Opt.*, vol. 10, no. 2, p. 024023, 2005.
- [6] M. Melendez-Ferro, M. W. Rice, R. C. Roberts, and E. Perez-Costas, "An accurate method for the quantification of cytochrome C oxidase in tissue sections," *J. Neurosci. Methods*, vol. 214, no. 2, pp. 156–162, 2013.
- [7] O. Senlik and N. M. Jokerst, "Spatially resolved diffuse reflectance Si probes for tissue characterization over a wide scattering range," *2015 IEEE Photonics Conf. IPC 2015*, vol. 2, pp. 625–626, 2015.
- [8] I. Tachtsidis, L. Gao, T. S. Leung, M. Kohl-Bareis, C. E. Cooper, and C. E. Elwell, "A Hybrid Multi-Distance Phase and Broadband Spatially Resolved Spectrometer and Algorithm for Resolving Absolute Concentrations of Chromophores in the Near-Infrared Light Spectrum," *Adv. Exp. Med. Biol.*, vol. 662, pp. 169–175, 2010.
- [9] A. Jakobsson and G. E. Nilsson, "Prediction of sampling depth and photon pathlength in laser Doppler flowmetry," *Med. Biol. Eng. Comput.*, vol. 31, no. 3, pp.

301–307, 1993.

- [10] S. Dhar *et al.*, “A diffuse reflectance spectral imaging system for tumor margin assessment using custom annular photodiode arrays.,” *Biomed. Opt. Express*, vol. 3, no. 12, pp. 3211–22, 2012.
- [11] B. C. Wilson and S. L. Jacques, “Optical reflectance and transmittance of tissues: principles and applications,” *Quantum Electron. IEEE J.*, vol. 26, no. 12, pp. 2186–2199, 1990.
- [12] O. Senlik, “Custom Photodiode Arrays for Diffuse Spectroscopic Imaging of Tissues,” Duke University, 2016.
- [13] O. Senlik and N. M. Jokerst, “Concentric multipixel silicon photodiode array probes for spatially resolved diffuse reflectance spectroscopy,” *IEEE J. Sel. Top. Quantum Electron.*, vol. 22, no. 3, 2016.
- [14] N. M. J. Ozlem Senlik, Callie Woods, “High pixel density concentric si spatially resolved diffuse reflectance probe: Wide absorption range phantom study,” *2016 IEEE Sensors*, pp. 1–3, 2016.
- [15] B. S. Nichols, N. Rajaram, and J. W. Tunnell, “Performance of a lookup table-based approach for measuring tissue optical properties with diffuse optical spectroscopy,” *J. Biomed. Opt.*, vol. 17, no. 5, p. 057001, 2012.
- [16] S. A. P. Steven L. Jacques, “Mie Theory Model for Tissue Optical Properties,” 1998. .
- [17] O. Senlik and N. M. Jokerst, “Concentric Multi-pixel Photodiode Array Probes For Optical Tissue Characterization,” *Adv. Photonics 2015, OSA Tech. Dig. (Optical Soc. Am. 2015)*, 2015.
- [18] H. Nilsson, M. Larsson, G. E. Nilsson, and T. Strömberg, “Photon pathlength determination based on spatially resolved diffuse reflectance.,” *J. Biomed. Opt.*, vol. 7, no. 3, pp. 478–485, 2002.
- [19] S. Matcher, M. Cope, and D. T. Delpy, “Use of the water absorption spectrum to quantify tissue chromophore concentration changes in near-infrared spectroscopy.,” *Phys. Med. Biol.*, vol. 39, no. 1, pp. 177–96, 1994.
- [20] “Photodetectors- Introduction.” [Online]. Available: [http://www.ee.sc.edu/personal/faculty/simin/ELCT566/15 Photodetectors -%0A](http://www.ee.sc.edu/personal/faculty/simin/ELCT566/15%20Photodetectors%20-%0A)

Introduction, Photoconductors.pdf.

- [21] Stanley Wolf and Richard N. Tauber, *Silicon Processing for the VLSI Era vol. 1: Process technology*. 1986.
- [22] P. Bhattacharya, *Semiconductor Optoelectronic Devices*. Upper Saddle River, NJ: Prentice Hall, 1997.
- [23] O. Senlik, G. Greening, T. J. Muldoon, and N. M. Jokerst, "Spatially resolved diffuse reflectance spectroscopy of two-layer turbid media by densely packed multi-pixel photodiode reflectance probe," *Proc. SPIE*, vol. 9700, no. March 2016, 2016.
- [24] B. Lariviere, K. S. Garman, N. L. Ferguson, D. A. Fisher, and N. M. Jokerst, "Spatially Resolved Diffuse Reflectance Spectroscopy of Tumor and Normal Excised Human Colon with Thin Film Si Sensors," *Opt. Sensors Sens. Congr.*, vol. 2019, no. C, pp. 4–5, 2019.
- [25] C. Matcher, S.J. Cooper, "Absolute quantification of deoxyhaemoglobin concentration in tissue near infrared spectroscopy," *Phys. Med. Biol.*, vol. 39, pp. 1295–1312, 1994.
- [26] O. O. Soyemi, M. R. Landry, Y. E. Yang, P. O. Idwasi, and B. R. Soller, "Skin color correction for tissue spectroscopy: Demonstration of a novel approach with tissue-mimicking phantoms," *Appl. Spectrosc.*, vol. 59, no. 2, pp. 237–244, 2005.
- [27] S. C. Feng, F. Zeng, and B. Chance, "Monte Carlo simulations of photon migration path distributions in multiple scattering media," *Phot. Migr. Imaging Random Media Tissues*, vol. 1888, pp. 78–89, 1993.
- [28] T. M. Bydlon, R. Nachab, N. Ramanujam, H. J. C. M. Sterenborg, and B. H. W. Hendriks, "Chromophore based analyses of steady-state diffuse reflectance spectroscopy: Current status and perspectives for clinical adoption," *J. Biophotonics*, vol. 8, no. 1–2, pp. 9–24, 2015.
- [29] P. Geladi and B. R. Kowalski, "Partial least-squares regression: a tutorial," *Anal. Chim. Acta*, vol. 185, no. C, pp. 1–17, 1986.
- [30] K. Maruo, M. Tsurugi, M. Tamura, and Y. Ozaki, "In Vivo Noninvasive Measurement of Blood Glucose by Near-Infrared Diffuse-Reflectance Spectroscopy," *Appl. Spectrosc.*, vol. 57, no. 10, pp. 1236–1244, 2003.

- [31] S. F. Malin, T. L. Ruchti, T. B. Blank, S. N. Thennadil, and S. L. Monfre, "Noninvasive prediction of glucose by near-infrared diffuse reflectance spectroscopy," *Clin. Chem.*, vol. 45, no. 9, pp. 1651–1658, 1999.
- [32] C. C. Shou, T. C. R. Hsiao, J. K. Lin, C. Y. Wang, and K. C. Huihua, "Comparison of the performance of linear multivariate analysis methods for normal and dysplasia tissues differentiation using autofluorescence spectroscopy," *IEEE Trans. Biomed. Eng.*, vol. 53, no. 11, pp. 2265–2273, 2006.
- [33] I. Dreissig, S. Machill, R. Salzer, and C. Krafft, "Quantification of brain lipids by FTIR spectroscopy and partial least squares regression," *Spectrochim. Acta - Part A Mol. Biomol. Spectrosc.*, vol. 71, no. 5, pp. 2069–2075, 2009.
- [34] I. Barman, N. C. Dingari, N. Rajaram, J. W. Tunnell, R. R. Dasari, and M. S. Feld, "Rapid and accurate determination of tissue optical properties using least-squares support vector machines," *Biomed. Opt. Express*, vol. 2, no. 3, p. 592, 2011.
- [35] B.-H. Mevik and R. Wehrens, "The pls Package: Principle Component and Partial Least Squares Regression in R," *J. Stat. Softw.*, vol. 18, no. 2, pp. 1–24, 2007.
- [36] H. J. Byrne, P. Knief, M. E. Keating, and F. Bonnier, "Spectral pre and post processing for infrared and Raman spectroscopy of biological tissues and cells," *Chem. Soc. Rev.*, vol. 45, pp. 1865–1878, 2016.
- [37] A. Koenig, B. Roig, J. Le, G. Josse, and J. Dinten, "Accessing deep optical properties of skin using Diffuse Reflectance Spectroscopy," *Proc. SPIE*, vol. 9537, no. 0, pp. 1–8, 2015.
- [38] I. Fredriksson *et al.*, "Inverse Monte Carlo in a multilayered tissue model : merging diffuse reflectance spectroscopy and laser Doppler flowmetry Inverse Monte Carlo in a multilayered tissue model : merging diffuse reflectance spectroscopy and laser Doppler flowmetry," *J. Biomed. Opt.*, vol. 18, no. 12, 2013.
- [39] C. M. G. Oh, R. S. Ubramaniam, N. M. S. Aad, S. A. A. Li, and M. Eriaudeau, "Subcutaneous veins depth measurement using diffuse reflectance images," *Opt. Express*, vol. 25, no. 21, pp. 95–102, 2017.
- [40] K. Komolibus, C. Fisher, K. Grygoriev, R. Burke, and B. C. Wilson, "In-vivo diffuse reflectance for bone boundary detection in orthopedic surgery," *Biophotonics Congr. Opt. Life Sci.*, vol. 2019, pp. 2–3, 2019.
- [41] I. Tachtsidis, M. M. Tisdall, and C. Pritchard, "Analysis of the Changes in the

Oxidation of Brain Tissue Cytochrome-c-Oxidase in Traumatic Brain Injury Patients during Hypercapnoea," *Adv. Exp. Med. Biol.*, vol. 701, pp. 9–14, 2011.

- [42] Q. Liu and N. Ramanujam, "Sequential estimation of optical properties of a two-layered epithelial tissue model from depth-resolved ultraviolet – visible diffuse reflectance spectra," *Appl. Opt.*, 2006.
- [43] A. N. BASHKATOV, E. A. GENINA, and V. V. TUCHIN, "Optical Properties of Skin, Subcutaneous, and Muscle Tissues: a Review," *J. Innov. Opt. Health Sci.*, vol. 04, no. 01, pp. 9–38, 2011.
- [44] T. Binzoni, T. S. Leung, a H. Gandjbakhche, D. Rüfenacht, and D. T. Delpy, "The use of the Henyey-Greenstein phase function in Monte Carlo simulations in biomedical optics.," *Phys. Med. Biol.*, vol. 51, no. 17, pp. N313-22, 2006.
- [45] P. Oltulu, B. Ince, N. Kokbudak, S. Findik, and F. Kilinc, "Measurement of Epidermis , Dermis , and Total Skin Thicknesses from Six Different Body Regions with a new Ethical Histometric Technique," *Turkish J. Plast. Surg.*, pp. 56–61, 2018.
- [46] J. H. Cheng and D. W. Sun, "Partial Least Squares Regression (PLSR) Applied to NIR and HSI Spectral Data Modeling to Predict Chemical Properties of Fish Muscle," *Food Eng. Rev.*, vol. 9, no. 1, pp. 36–49, 2017.
- [47] G. J. Greening, L. M. Higgins, D. Roblyer, M. C. Pierce, and T. J. Muldoon, "Characterization of thin poly (dimethylsiloxane)-based tissue-simulating phantoms with tunable reduced scattering and absorption coefficients at visible and near- infrared wavelengths," *J. Biomed. Opt.*, vol. 19, no. 11, 2014.
- [48] T. Fawcett, "An introduction to ROC analysis," *Pattern Recognit. Lett.*, vol. 27, pp. 861–874, 2006.
- [49] J. N. Mandrekar, "Receiver Operating Characteristic Curve in Diagnostic Test Assessment," *J. Thorac. Oncol.*, vol. 5, no. 9, pp. 1315–1316, 2010.
- [50] J. Giraldo, A. Giordano, M. Almadi, and W. Lin, "Assessment of complete hemodynamic characteristics of in vivo tissues using a non-contact laser Doppler and total diffuse reflectance spectroscopy system," *Biophotonics Congr. Biomed. Opt. Congr.*, pp. 6–7, 2018.
- [51] O. Senlik and N. M. Jokerst, "Concentric Si Annular Photodiode Arrays for Spatially Resolved Diffuse Reflectance Spectroscopy," *Lasers Electro-Optics (CLEO), 2015 Conf.*, pp. 4–5, 2015.

- [52] C. Kolyva *et al.*, "Cytochrome c oxidase response to changes in cerebral oxygen delivery in the adult brain shows higher brain-specificity than haemoglobin," *Neuroimage*, vol. 85, pp. 234–244, 2014.
- [53] E. L. Bell, "Mitochondrial regulation of oxygen sensing," *Mitochondrion*, vol. 5, no. 5, pp. 322–332, 2005.
- [54] G. Bale, S. Mitra, J. Meek, N. Robertson, and I. Tachtsidis, "A new broadband near-infrared spectroscopy system for in-vivo measurements of cerebral cytochrome-c-oxidase changes in neonatal brain injury.," *Biomed. Opt. Express*, vol. 5, no. 10, pp. 3450–66, 2014.
- [55] S. Suzuki, S. Takasaki, T. Ozaki, and Y. Kobayashi, "A Tissue Oxygenation Monitor using NIR Spatially Resolved Spectroscopy," *SPIE Proc.*, vol. 3597, no. January 1999, pp. 582–592, 1999.
- [56] F. M. Scandurra and E. Gnaiger, "Modelling of Mitochondrial Oxygen Consumption and NIRS Detection of Cytochrome Oxidase Redox State," *Adv. Exp. Med. Biol.*, vol. 662, pp. 7–25, 2010.

## Biography

Callie Woods attended Princeton University and in 2014 she received her Bachelor of Science in Electrical Engineering. While at Princeton, she received the Newport Undergraduate Award in Photonics and the Optical Engineering Award of Excellence. She received both an M.S. and Ph.D. from Duke University in 2020. While at Duke she received the following awards: James B Duke Fellowship, John Chambers Fellowship, Chambers Scholarship, Kristina M Johnson Fellowship, and NSF GRFP Honorable Mention. A list of publications from her time at Duke is below:

O. Senlik, C. Woods and N. M. Jokerst, "High pixel density concentric si spatially resolved diffuse reflectance probe: Wide absorption range phantom study," *2016 IEEE SENSORS*, Orlando, FL, 2016, pp. 1-3, doi: 10.1109/ICSENS.2016.7808487.

C. M. Woods, O. Senlik, and N. M. Jokerst, "A Custom Multi-Pixel Photodetector Probe and Partial Least Squares Regression for the Efficient Identification of Optical Tissue Properties," in *Frontiers in Optics / Laser Science*, OSA Technical Digest (Optical Society of America, 2018), paper JW4A.113.

C. M. Woods, O. Senlik, G. Greening, T. J. Muldoon, and N. M. Jokerst, "Depth-Sensitive Tissue Measurements Using a Multi-Pixel Photodetector Probe," in *Biophotonics Congress: Biomedical Optics 2020 (Translational, Microscopy, OCT, OTS, BRAIN)*, OSA Technical Digest (Optical Society of America, 2020), paper JTU3A.14.